Transformation-Mismatch Plasticity in Zirconia Ceramic Composites

by

Michael J. Whitney

B.S. Materials Science and Engineering
University of Michigan, 1995

Submitted to the Department of
Materials Science and Engineering in
Partial Fulfillment of the Requirements for the Degree of

MASTER OF SCIENCE IN MATERIALS SCIENCE AND ENGINEERING

at the

MASSACHUSETTS INSTITUTE OF TECHNOLOGY

June 1997

Signature of Author ....
Department of Materials Science and Engineering
May 9, 1997

Certified by ....
David C. Dunand
AMAX Associate Professor of Materials Engineering
Thesis Supervisor

Accepted by ....
Linn W. Hobbs
John F. Elliott Professor of Materials
Chairman, Departmental Committee of Graduate Students

TRANSFORMATION-MISMATCH PLASTICITY IN ZIRCONIA CERAMIC COMPOSITES

by

MICHAEL J. WHITNEY

Submitted to the Department of Materials Science and Engineering
on May 9, 1997 in partial fulfillment of the requirements
for the degree of Master of Science in Materials Science and Engineering

ABSTRACT

Ceramic matrix composites consisting of partially stabilized zirconia with 5% and 10% by volume unstabilized zirconia particles (PSZ-ZrO_2) were tested for steady-state deformation behavior in tension and compression. While tensile experiments were inconclusive due to matrix cracking, compressive samples thermally cycled under stress about the allotropic temperature of the particulate phase (950°C to 1250°C) deformed at faster strain rates than control samples. Up to 8% strain has been created without macroscopic damage at strain rates of $0.85 \cdot 10^{-7}$ to $5.3 \cdot 10^{-7}$ s^{-1}.

The enhanced deformation rate is attributed to transformation-mismatch plasticity, caused by the biasing of cyclical internal stresses created by the 6% volume change during the zirconia allotropic transformation. Dilatometry of a PSZ-5% ZrO_2 composite shows a ± 37 MPa change in the internal mean level of stress, compared with the nominal value of ± 108 MPa calculated by the Eshelby technique. Microstructural observations of particle cracking can account for this discrepancy. These results are compared with three existing models for internal-stress plasticity and a numerical technique is developed to consider the relaxation of internal stresses by creep.

Thesis Supervisor: David C. Dunand

Title: AMAX Associate Professor of Materials Engineering

TABLE OF CONTENTS

Abstract 2
Table of Contents 3
List of Illustrations and Figures 5
List of Tables 7
Acknowledgments 8
1. Introduction 9
2. Background 11
    2.1 Creep regimes 11
        2.1.1 Power-law creep 11
        2.1.2 Diffusional creep 12
        2.1.3 Superplasticity 12
    2.2 Internal-stress plasticity 13
        2.2.1 Review of Experimental Internal-Stress Plasticity 14
        2.2.2 Models of Internal-Stress Superplasticity 15
    2.3 Materials 19
        2.3.1 Properties 19
        2.3.2 High temperature mechanical behavior 20
3. Experimental 23
    3.1 Testing apparatus 23
        3.1.1 Mechanical testing system 23
        3.1.2 Furnace 24
        3.1.3 Temperature measurement and control 24
        3.1.4 Data acquisition 25
    3.2 High temperature experiments 25
        3.2.1 Procedure 25
        3.2.2 Experiments performed 26
    3.3 Materials 28
        3.3.1 Powder preparation 28
        3.3.2 Processing 29
    3.4 Characterization 30
        3.4.1 Thermal 30
        3.4.2 Microstructural 31
        3.4.3 Physical 31
    3.5 Figures and Illustrations 33
4. Results 34
    4.1 Experimental materials 34
    4.2 Creep/TSP experiment overview 36
    4.3 Tensile experiments 38
        4.3.1 Results from tensile tests on pure PSZ (0%) composite samples 38
        4.3.2 Results from tensile tests on PSZ-5% ZrO_2 composite samples 39
        4.3.3 Results from tensile tests on PSZ-10% ZrO_2 composite samples 40
    4.4 Compression Experiments 40
        4.4.1 Results from compression tests on pure PSZ (0%) samples 40
        4.4.2 Results from compression tests on PSZ-5% ZrO_2 composite samples 41
        4.4.3 Results from compression tests on sintered PSZ-5% ZrO_2 composite samples 42
    4.5 Microstructural evolution 43
    4.6 Figures and Illustrations 45

5. Discussion 58
- 5.1 Results of creep experimentation 58
- 5.2 Models of internal stresses 59
- 5.3 Internal-Stress plasticity 63
  - 5.3.1 Modeling based on Greenwood and Johnson 63
  - 5.3.2 Modeling based on Sato & Kuribayashi 64
  - 5.3.3 Modeling based on Wu et al. 65
- 5.4 Further modeling 66
- 5.5 Figures and Illustrations 69

6. Conclusions 76
7. Suggestions for Future Work 77
Appendix 1. Engineering drawing of tension pullrods 79
Appendix 2. Isothermal effective temperature calculation 80
Appendix 3. Tension experiment summary 81
Appendix 4. Compression experiment summary 82
Appendix 5. Engineering drawing of the tensile sample. 83
Appendix 6. Eshelby technique calculations 84
Appendix 7. Calculations for Sato and Kuribayashi model 87
Bibliography 89

LIST OF ILLUSTRATIONS AND FIGURES

Figure 3.1.1. Schematic of the experimental cyclical temperature profile. 33

Figure 4.1.1. SEM micrograph of the coarsened ZrO2 powders used in the composite samples. 45

Figure 4.1.2. SEM micrograph (high magnification) of the ZrO2 particles used in the composite. 45

Figure 4.1.3. Optical micrograph of an as-received 10% composite sample. 46

Figure 4.1.4. SEM micrograph of polished matrix PSZ in a 10% composite sample at high magnification. 46

Figure 4.1.5. SEM micrograph of a sectioned particle in a polished 10% composite. 47

Figure 4.1.6. SEM micrograph of an unpolished, sectioned 10% composite surface. 47

Figure 4.1.7. Differential scanning calorimetry results of ZrO2 powders from coarsening pre-treatments. 48

Figure 4.1.8. Complete dilatometry results for hot-pressed 10% composite, compared with a simplified expected curve. 49

Figure 4.3.1. Corrected strain versus time for thermal cycling experiment on pure PSZ (0%) material at 5 MPa tensile stress, second run. 50

Figure 4.3.2. Displacement versus time for two successive 10 MPa thermal cycling tensile experiments on a sample of pure PSZ (0%). 50

Figure 4.3.3. Primary, isothermal creep displacement of pure PSZ (0%) samples at 5 MPa, showing creep at 1250°C and 1178°C. 51

Figure 4.3.4. Transformation-mismatch plasticity during thermal cycling of 5% material at 5 MPa tensile stress through three successive runs until failure. 51

Figure 4.3.5. Deformation of a PSZ-5% ZrO2 sample during thermal cycling after isothermal creep under 5 MPa tensile stress. 52

Figure 4.3.6. Transformation-mismatch plasticity during thermal cycling of a PSZ-10% ZrO2 composite at 5 MPa tensile stress, second run. 52

Figure 4.4.1. Isothermal (1178°C) creep of a sample of pure PSZ (0%) under 10 MPa compressive stress. 53

Figure 4.4.2. Comparison of 20 MPa compression experiments during isothermal (1178°C) and thermal cycling conditions on pure PSZ (0%). 53

Figure 4.4.3. Primary creep behavior of pure PSZ (0%) and PSZ-5% ZrO2 composites during isothermal (1178°C) compression creep at 10 MPa. 54

Figure 4.4.4. Comparison of 5 MPa compression experiments during thermal cycling and isothermal creep on a PSZ-5% ZrO2 composite. 54

Figure 4.4.5. Comparison of 10 MPa compression experiments during thermal cycling and isothermal creep on a PSZ-5% ZrO2 composite. 55

Figure 4.4.6. Comparison of 20 MPa compression experiments during thermal cycling and isothermal creep on a PSZ-5% ZrO2 composite. 55

Figure 4.4.7. Deformation behavior of PSZ-5% ZrO2 composites under various isothermal compressive stress experiments at 1178°C. 56

Figure 4.5.1. SEM micrograph at high magnification illustrating void (cavity) formation in a material pulled to 4.4% strain in tension during thermal cycling at 5 MPa. 56

Figure 4.5.2. Optical micrograph of a polished PSZ-10% ZrO2 composite after tensile strain to 4.4% during thermal cycling. 57

Figure 4.5.3. SEM micrograph of a fracture surface from a PSZ-10% ZrO2 composite sample broken at high temperature and under 5 MPa tensile stress. 57

Figure 5.1.1. Steady-state strain rates of thermal cycling and isothermal (1178°C) compression creep experiments on high density PSZ-5% ZrO2 composites. 69

Figure 5.2.1. Eshelby's conceptual cutting and welding exercise to understand the states of stress and strain imposed by a transformation mismatch in a composite. 69

Figure 5.2.2. Schematic of the stresses created in the matrix adjacent to the particle due to allotropic transformation in the particle during cooling. 70

Figure 5.2.3. Simple conceptual models for estimating the sign and magnitude of matrix internal stresses during the particle transformation. 70

Figure 5.2.4. Highlights of dilatometry results with measurements of mean internal matrix strain changes, <εM>, and measured coefficient of thermal expansion. 71

Figure 5.3.1. Linear results of compression experiments on PSZ-5% ZrO2 composites at 5 MPa fitted with a model based on Greenwood and Johnson. 72

Figure 5.3.2. Logarithmic results of compression experiments on PSZ-5% ZrO2 composites at 5 MPa fitted with a model based on Greenwood and Johnson. 72

Figure 5.3.3. Linear results of compression experiments on PSZ-5% ZrO2 composites at 5 MPa fitted with a model based on Sato and Kuribayashi. 73

Figure 5.3.4. Logarithmic results of compression experiments on PSZ-5% ZrO2 composites at 5 MPa fitted with a model based on Sato and Kuribayashi. 73

Figure 5.3.5. Linear results of compression experiments on PSZ-5% ZrO2 composites at 5 MPa fitted with a model based on Wu, Wadsworth, and Sherby. 74

Figure 5.3.6. Logarithmic results of compression experiments on PSZ-5% ZrO2 composites at 5 MPa fitted with a model based on Wu, Wadsworth, and Sherby. 74

Figure 5.4.1. Plot of expected internal stress relaxation over several transformation thermal cycles. 75

Figure 5.4.2. Results of compression experiments compared with Wu model incorporating relaxation of internal stresses from Figure 5.4.1. 75

LIST OF TABLES

Table 2.3.1. Table of relevant engineering properties for partially stabilized zirconia (PSZ) and pure zirconia. 22

Table 5.2.1. Results of Eshelby internal stress calculations for PSZ-5% ZrO2 and PSZ-10% ZrO2. 60

ACKNOWLEDGMENTS

I would like to extend a sincere thank you to all of the people who have helped, guided, and assisted me through completion of this work. I would especially like to thank:

Prof. David C. Dunand, for his constant guidance and wisdom. His praise and understanding, as well as the immense faith and trust he had in my work, were essential in making this thesis and my endeavor at MIT a truly pleasurable experience.

This work was supported by the Army Research Office under grant # DAAH04-95-1-0629, monitored by Dr. W. C. Simmons. I would like to thank Dr. Simmons and the ARO for that support. This work also made use of MRSEC Shared Facilities supported by the National Science Foundation under Award Number DMR-9400334.

The 8-328 research group at MIT: it has been a great time. Whether the topic was the languages, my search for employment, business economics, computers, or (more soberly) internal stresses, mechanics, thesis writing, and lab techniques, I appreciate that you all were always there, ready to help. Raj Vaidyanathan, T.A. Venkatesh, Hermann Holzer, Jacques Teisen, Christian Verdon, and Jean-Marc LeFeuvre: thank you all and I wish you well in everything you do.

People at MIT: Lenny Rigione for the time and guidance he provided for dilatometry work; Yin-Lin Xie, for assistance with metallography; Prof. Lorna Gibson, for continued permission to use her laboratory and equipment.

Joe and Pat at Bomas Machine Specialties for their speedy and high-quality machining work, and Michael Malyn at MICI for hot-pressing work.

I would also like to thank my family, Don and Olga Whitney, as well as Cynthia and Pete Black: for always supporting me in my endeavors (no matter how crazy they seemed), and for trusting my decisions. They have given me the opportunity to succeed.

To the rest of my friends in Boston: Peter Ragone, Josh Freedman, Zepe Osborne, Darren Obridgkeit, Mike Derdan, Jose Cervantes, Andrea D'Avella, Brian Ferla, Bram Hubbell (thanks for keeping the coffee warm), and Matt Neimark: it's been a lot of fun, and I will miss you all.

Finally, Kendra Goeman, for her care, support, patience, and understanding. My bond with her has been essential to my success and certainty of a happy future.

1. INTRODUCTION

There has been much interest recently in zirconia as an engineering ceramic due the many interesting and useful properties of the material. Not only is zirconia valuable as a high temperature refractory material, but partial stabilization with additives has increased the toughness of the material to the point that it is used in room-temperature structural applications for its wear resistance such as in scissors and knives [1]. The oxide can also be made an ionic conductor, lending to application in solid oxide fuel cells as well as conventional applications in oxygen sensors [2].

However, the traditional processing routes of zirconia-based materials are limited to powder processing techniques, rather than by forming or casting processes available for lower melting temperature metals. Powder techniques for processing often require a costly machining step to create shaped parts – machining accounts for a large fraction of the cost of a ceramic part. The development of microstructural superplasticity in many materials over the latter half of this century [3, 4], has allowed shaping of many ductile and brittle materials. Microstructural superplasticity is the ability to deform a crystalline material to very large strains in tension at a relatively fast rate without failure. In terms of the mechanics of deformation, this corresponds to the avoidance of plastic neck instabilities and cavitation during elongation, and this occurs when the stress resistance due to strain hardening in a macro- or microscopic neck is greater than the increase in stress caused by a reduction in the sample cross-sectional area. Microstructurally, superplasticity occurs by diffusional processes at grain boundaries, so superplastic materials must typically have very small grains (typically <10 μm for metals and <1 μm in ceramics) [3] and a microstructure resistant to grain growth (by creation of duplex microstructures, grain-boundary pinning additives, or reinforcements). Many of types of stabilized and partially stabilized zirconia ceramics have been made superplastic by development of processing methods able to form grains less than 1 μm. Unfortunately, this leads to high costs for these specially created powders. For many other materials, no viable method of creating fine powders or a stable microstructure exists.

There is another method of achieving superplasticity: internal stress superplasticity (for a recent review, see [5]). It has been found that materials with a renewable source of internal stresses – produced by phase transformation, thermal expansion anisotropy, or other kind of internal mismatch – can achieve the conditions necessary for superplastic behavior when these internal stresses are biased by an external stress; this phenomenon occurs without the limitation of fine grains. In the absence of external stress, large internal stresses in a material can cause local plasticity by yield or creep relaxation. Since this plasticity does not occur in any preferred direction on average, strain will not be accumulated by repeated creation of the internal stress. As soon as a small external stress is applied, however, the yield or creep can occur preferentially in the direction of the applied stress. This phenomenon was originally discovered in several bulk (non-composite) materials. Iron was shown to deform rapidly during the alpha-gamma phase transformation by Sauveur [6], and thermal cycling of polycrystalline zinc also led to rapid strain due to the high degree of anisotropy in the thermal expansion coefficient of the polycrystalline material [7]. Internal stress superplasticity can also be demonstrated during thermal cycling of composites, where internal stresses can be created by thermal expansion coefficient mismatch of the constituents (CTE-mismatch superplasticity), or by mismatch of strains caused by transformation of one of the composite phases [8]. This latter mechanism, called transformation-mismatch superplasticity (TSP) has been demonstrated in composites of titanium and titanium alloys with additions of titanium carbide (TiC) while cycling the temperature around the allotropic phase transformation of the matrix material [9].

The goal of this work is to demonstrate internal-stress superplastic conditions by transformation-mismatch in zirconia ceramic composites. The material system is a fine-grained partially stabilized zirconia matrix material with 5-10% (by volume) pure zirconia (ZrO_2) particulate reinforcement. At high temperatures, the matrix remains stable, while the particles experience an allotropic phase transformation at 1200°C during heating and 1000°C during cooling accompanied by a 6% volume change [2]. Mismatch of the transformation strain between these two constituents is the source of the internal stress. Experiments were performed in which a constant external stress (5-20 MPa) was applied during repeated thermal cycling above and below the allotropic temperatures. It will be shown that enhanced plasticity did occur compared with control situations in which no cyclical internal stresses were created, and it will be demonstrated that these enhanced strain rates are due to the generation of internal stresses which were relaxed preferentially in the direction of applied stress. These results will then be interpreted in terms of three micromechanical models, and the discrepancies between experiment and theory will be discussed in each case. Finally, the extent of some of the complications associated with this work will be discussed along with recommendations for future work. Although these experiments were performed in compression and to small strains, these results prove the validity of the models of internal-stress plasticity as well as open the possibilities of application of these techniques to achieve true transformation-mismatch superplasticity in PSZ-ZrO_2.

2. BACKGROUND

2.1 CREEP REGIMES

At high temperatures compared to the melting point of a material, deformation by creep will occur in response to an applied stress. Unlike typical low temperature yielding plasticity, creep is time-dependent is typically found experimentally to be dependent on three main variables: temperature, stress, and grain size. For a given material, several different mechanisms have been identified by which deformation occurs at high temperatures, depending on the level of these three variables. In general, the mechanism can be determined by fitting experimental deformation data from several different stress levels, all else being held equal, to the empirical equation, $\dot{\varepsilon} = A\sigma^n$. In this expression, $\dot{\varepsilon}$ is the constant strain rate, A is an empirically determined constant, σ is the stress, and n is the stress sensitivity.

2.1.1 *Power-law creep*

Power-law creep, the most commonly observed and technologically important type of creep in metals, typically occurs at high stress levels in crystalline materials. This type of creep is controlled by the formation and motion of dislocations through a crystalline lattice, microstructural phenomena which are dependent on temperature, T, and stress, s. Power-law creep is typically modeled by the following expression [4]:

$$\dot{\varepsilon} = A\frac{D_{sd}\mu b}{kT}\left(\frac{\sigma}{\mu}\right)^n. \tag{1}$$

In equation (1), D_{sd} is the material self-diffusion, μ the shear modulus, b is the burgers vector, k is Boltzmann's constant, and T is the absolute temperature. In general, a diffusion coefficient, D, can be expressed by

$$D = D_0\exp\left(\frac{-Q}{R\cdot T}\right) \tag{2}$$

where D_0 is the frequency factor, Q is the activation energy, and R is the gas constant. Dislocation motion is a function of stress and causes the stress sensitivity in power-law creep to be in the range of 3-10, depending on the type of dislocation motion and on the microstructure of the material in question.

2.1.2 Diffusional creep

Diffusion creep, which is typically dominant at lower stress levels and/or at higher temperatures than power-law creep, is commonly observed in ceramics. Deformation is accumulated by a flux of atoms diffusing preferentially in the direction of applied stress. It is shown by several simple arguments that diffusional creep can occur by either mass transport through the bulk material (lattice) or through grain boundaries. These well-established regimes of behavior are referred to as Nabarro-Herring and Coble creep, respectively, and are represented by the following constitutive equations [4]:

$$\dot{\varepsilon} = \alpha_1 \frac{\Omega D_{sd} \sigma}{kTd^2} \quad \text{(lattice diffusion)} \tag{3}$$

$$\dot{\varepsilon} = \alpha_2 \frac{\Omega \delta D_{gb} \sigma}{kTd^3} \quad \text{(boundary diffusion).} \tag{4}$$

In equations (3) and (4) α_1 and α_2 are dimensionless constants, Ω is the atomic volume, and δD_{gb} is the diffusion coefficient in boundary diffusion. The material grain size, d, first comes into account in the phenomenological description of creep since diffusional creep depends on the grain boundaries as either a source and sink of atoms or as a direct mass transport path.

2.1.3 Superplasticity

Only recognized in the past several decades as a phenomenon different than power-law or diffusional creep, superplasticity is not yet very well understood. A polycrystalline material is said to behave superplastically when it can the be deformed to a high tensile elongation before failure. In terms of mechanics, this is can occur when the strain hardening due to necking is greater than the increase in stress caused by decrease in cross-sectional area, resulting in n=1 and thus avoidance of neck instabilities [4]. In fact, most superplastic experiments exhibit a stress sensitivity of n=1-3; experimental observation of a low stress sensitivity can indicate the possibility of superplasticity.

Two general types of superplasticity have been demonstrated. Most research has focused on microstructural superplasticity, first discovered in 1912 by Bengough [10]. Early investigators of this phenomenon were faced with some confusion – whether the deformation is controlled by dislocation motion (n=3-10) or diffusional processes from equations (3) and (4) with n=1. In fact, the period of transition between diffusional and power law creep as stress increases will be describable by n=1-3; however, superplastic behavior occurs at a much wider range of stresses than would be associated with a transition of dominant mechanisms. Most early researchers did attempt to attribute the behavior to a combination of power-law and diffusional flow phenomenon [11]. However, more exhaustive studies indicated that superplasticity was indeed a new deformation mechanism. Microstructural superplasticity has been proposed to occur by a grain-boundary sliding process for which Ashby & Verrall [4] presented a model based on the motion of grain boundary dislocations with a stress sensitivity exponent of n=2:

$$\dot{\varepsilon} = \alpha_3 \frac{\Omega \delta D_{gb} \sigma^2}{\mu k T d^2} \tag{5}$$

Since deformation occurs by the sliding of grains rather than transport of material by diffusion, the grains remain equiaxed and high strains may be accumulated without microstructural limitations. However, superplasticity will typically occur only in fine-grained materials, typically d<1 μm in ceramics and d< 10 μm in metals, and within a relatively narrow range of temperatures and stress levels. Microstructural superplasticity has been demonstrated in many types of engineering ceramics and metals, as described in several recent texts and reviews [3], [12].

The other type of superplasticity, internal-stress superplasticity, is distinct from microstructural superplasticity and creep in that it does not occur in a polycrystalline material held at constant stress and temperature. Rather, the above requirements of superplastic behavior can be met by a materials capable of generating internal stresses by one of several possible mechanisms, then deforming the material at high temperature while repeatedly generating internal stresses. Materials deformable by internal-stress superplasticity are not necessarily limited to fine grained microstructure or by the narrow range of stresses and temperatures required of microstructural superplasticity.

2.2 *INTERNAL-STRESS PLASTICITY*

Internal stress plasticity is created by the biasing of internal stresses by an external force. Internal stresses are caused by a mismatch of strains, and there are four separate classes mechanisms that can cause strain *in general* in a material: (1) thermal expansion - caused by temperature changes; (2) radiation swelling - caused by irradiation; (3) compressibility - caused by isostatic pressure; and (4) phase transformation - caused by temperature or stress. Any of these four types of strain may be induced externally, and, with the proper microstructural and experimental conditions, may create the mismatch leading to internal stress. Following is a review of research which demonstrated internal stress and measured the extent to which it enhances plasticity, creep, and superplasticity.

2.2.1 Review of Experimental Internal-Stress Plasticity

Internal-stress enhanced plasticity and superplasticity have been shown to occur in two distinct classes of materials: pure or single-phase materials, and two-phase or composite materials. Creation of strain mismatch in polycrystalline pure materials is possible under two cases: anisotropy of a spatially homogeneous behavior, or a spatially inhomogeneous isotropic event [5].

Enhanced plasticity due to internal stresses was first observed as the weakening of iron at its phase transformation temperature by Sauveur in 1924 [6]. In the following years, it was recognized by Greenwood and Johnson [13] and others that the plasticity is caused by mismatch of the strains at the transformation front. Those authors demonstrated internal stress plasticity caused by phase transformation during repeated thermal cycling of iron, cobalt, titanium, and zirconium. A similar effect during compression and bending tests have been observed in ceramics Bi_2O_3 [14] and ZrO_2 [15]. Internal stresses are said to be created in an inhomogeneous fashion since the mismatch occurs between grains of the two allotropic phases with different densities. Enhanced plasticity in pure materials has also been discovered during homogeneous events in materials with anisotropic behavior of individual crystallites. The internal stresses necessary for internal stress superplasticity have been demonstrated during thermal cycling of zinc [16], [7], [17] and uranium [7, 16] due to crystallographic anisotropy of thermal expansion coefficients. In addition, anisotropic swelling of uranium during neutron irradiation [18] can lead to a similar effect.

While demonstration of internal stresses in bulk single phase or pure materials is largely a function of the material properties, it is in some respects easier to design a composite which can produce internal stresses. Similar to the homogeneous formation of internal stresses in pure materials with anisotropic crystallographic properties, internal stresses responsible for the creation of internal stress superplasticity has been demonstrated during thermal cycling of Al-SiC composite samples [19], due to mismatch of the thermal coefficient of expansion of the two materials. Likewise, the same effect has been observed during pressure cycling of Al-SiC samples due to differences in compressibility [20].

Internal stresses in composite material systems may also be created by phase transformation. Application of a small biasing external stress has been shown to enhance plasticity and create superplastic conditions in composites of Ti/TiC when the experimental temperature is cycled about the phase transformation temperature of the matrix titanium phase [9]. Similar effects have also been created in composites of NiAl/ZrO_2 [21], a system in which the particle reinforcement itself undergoes the transformation.

2.2.2 *Models of Internal-Stress Superplasticity*

Experimental work in internal stress enhanced plasticity has typically shown that the strain accumulated over the stress-inducing cycle is proportional to the applied stress, a necessary condition for superplasticity. Most of this work has been interpreted in terms of Greenwood and Johnson's micromechanical derivations (described below) [13]. Since that time, there has been much work developing theories based on microstructural first principals, many based on dislocation formation and density [22]. Much of this work strives to develop understanding of single-phase transforming metals, where plasticity, rather than creep, is the deformation mechanism: e.g., LeBlond [23], Diani [24]. De Jong and Rathenau [25] and Zhang et al [26] primarily considered low temperature behavior. While the details varied, the models created by these later works all tended to confirm the linear dependence of strain during cycling on stress, and they did not contain much additional information valuable to this analysis. This review will focus on (a) the original micromechanical work by Greenwood and Johnson [13], (b) some of the initial effort toward microstructural modeling of the phenomenon predicted in mechanics (Wu et al. [7] and Kot and Weiss [27]), (c) work that presents special and/or clarifying insight to this analysis (Paterson [28]), and (d) theory which focuses on internal stresses in composites (Sato and Kuribayashi [8]), which is a similar situation to the experimental model described here.

Greenwood and Johnson [13] developed a linear theory for internal-stress enhanced plasticity at low stresses based entirely upon a micromechanical model of transforming materials that obey the Levy-Von Mises equation of flow. The theory applies to rigid perfectly plastic materials and is used in interpreting materials tested at low homologous temperatures where creep does not occur. The result of the derivation is that the strain accumulated during a cycle in which internal stresses are generated by a phase change is proportional to the change in volume (density) of the phases, $\Delta V/V$, proportional to the applied stress σ, and inversely proportional to the material yield strength, σ_y. The relationship is given by

$$\Delta\varepsilon = \frac{5}{3}\frac{\Delta V}{V}\frac{\sigma}{\sigma_y}. \tag{6}$$

This simple expression holds true for materials at low temperatures which yield plastically. For materials with internal stresses at high temperatures, the authors present a relationship representing the strains caused by internal stresses due to transformation,

$$\Delta\varepsilon = \frac{4}{3}\frac{\Delta V}{V}\frac{5n}{4n+1}\frac{\sigma}{\sigma_i}, \tag{7}$$

where σ_i is the internal stress generated in the material during the phase transformation, and n is the stress sensitivity exponent. Equation (7) is presented for the case where internal stresses cause fast creep. As reviewed below, researchers have had much success fitting experimental data for many types of internal stress experiments to these expressions; they can be a valuable first approach in interpreting experimental behavior.

Kot and Weiss [27] developed one of the first microstructural theories explaining the linear behavior of strain accumulation during transformation plasticity. The authors confirm that transformation plasticity is the result of the superposition of small external stresses on very large internal stresses, and they calculate the effect based on elementary dislocation theory. Taking a simple, scalar-based approach, the internal stresses are added (or subtracted) to the applied load and averaged over the heating and cooling cycles to describe the macroscopic strain rate. The theory results in a conclusion similar to that of Greenwood and Johnson in equation (6), except that an internal stress due to transformation is used in place of the material yield stress.

Paterson [28] avoids the yield plasticity argument and makes some interesting observations about the implications of internal stresses. In this model, stress is applied to a polycrystalline material going through a phase transformation from phase A to phase B at a transformation (volume fraction) rate of $\dot{X}$. The instantaneous macroscopic strain rate during transformation can be considered to be resulting from three different "domains":

$$\dot{\varepsilon} = \frac{1}{V}\int_{V_A}\dot{\varepsilon}_A dV + \frac{1}{V}\int_{V_B}\dot{\varepsilon}_B dV + \varepsilon_T\dot{X} \tag{8}$$

where $\dot{\varepsilon}_A$ and $\dot{\varepsilon}_B$ are local strain rates in elementary units of phase A and B, respectively, and ε_T is the strain associated with the transformation itself. The transformation strain, ε_T, is reversible and cancels upon a complete cycle, and thus does not contribute to a measured average strain rate. Local strain rates are caused by linear addition of local (transformation-mismatch induced) stresses and the external applied stress. If average local stresses are considered, and the material flows by a linear (Newtonian) constitutive relationship, the internal stresses are "self-balancing" and will not contribute to the strain caused by external applied stress. Newtonian flow corresponds to such phenomena as diffusion creep, grain-boundary sliding, and microstructural superplasticity. Furthermore, the author states that transient effects would be expected in creep relaxation which occurs with n>1, but discounts them as "not of very large magnitude". If internal stresses created by phase transformation-mismatch were much smaller than applied stresses in this model, this would be true, and is backed up by Greenwood and Johnson's statements that the effect is only anticipated at low stresses. However, if internal stresses are comparable to or larger than external stresses, then an enhancement of strain rate would be observed based on this simple representation. The author argues that transformation-enhanced plasticity can only be explained by (1) changes in material parameters such as diffusion coefficients or elastic constants, or (2) changes in dislocation density. The first possibility is worth considering when diffusion or grain-boundary sliding is a dominant deformation mechanism, while the second conjecture may be responsible for the contribution of internal stresses to strain if a material is relaxing by power-law creep. The underlying concept is one which may prove important – i.e. in the absence of yielding and when internal stresses are relaxed microstructurally by Newtonian or near-Newtonian flow, underlying microstructural phenomena may control the effect of transformation plasticity, rather than effects predicted by micromechanics.

A more rigorous theoretical treatment of the scalar internal stress addition model was created by Wu et al [7]. This model is presented for a pure polycrystalline material going through an allotropic transformation, but the results are given in a general form applicable to any situation with internal stresses. An important distinction is made initially: in a yielding, plastic matrix subject to large strains sufficient to induce matrix plasticity, the internal stress will be exactly the yield stress of the material. This makes intuitive sense, since the material will cease to strain plastically when the stress level drops to the yield stress, leaving a residual stress. In contrast to Greenwood and Johnson, this model completely ignores the "transient" effect of external stress biasing internal stresses during plasticity. Instead, it considers strains due to internal stress *after* plastic flow only. The authors propose that half of the dislocations responsible for creep are exposed to a an average internal stress and half of the dislocations are subjected to an equal but opposite internal stress, by the representation:

$$\dot{\varepsilon}_{tot} = \frac{1}{2}\left[\dot{\varepsilon}(|\sigma + \sigma_i|) + \frac{|\sigma - \sigma_i|}{\sigma - \sigma_i}\dot{\varepsilon}(|\sigma - \sigma_i|)\right] \tag{9}$$

where $\dot{\varepsilon}(\sigma)$ is the constitutive equation for creep (the absolute values are used to ensure that the proper sign is used for stress in the creep equation). Using a simplified power-law creep expression for $\dot{\varepsilon}(\sigma)$, this equation may be reduced by eliminating terms from a binomial expansion to the following:

$$\dot{\varepsilon}_{tot} = n \cdot \dot{\varepsilon}(\sigma_i) \cdot \frac{\sigma}{\sigma_i} \tag{10}$$

Equation (10) again predicts a stress sensitivity of n=1 for internal stress enhanced plasticity based entirely on the contribution of strain *after* initial yielding plasticity, confirming Greenwood and Johnson's full treatment of yielding flow. It is interesting to note that the authors do observe that increased cycling speed leads to increased strain rates, which is easily explained by the classical transient plastic flow that occurs during each thermal cycle. Yet it is explained in terms of an increase in yield stress due to the lack of recovery, although it most likely results from the plastic yield that the theory disregards. Also presented is a method of comparing thermal cycling behavior with isothermal behavior with the introduction of an "effective diffusivity", an integrated average diffusivity over a thermal cycle. Creep occurring isothermally at the temperature corresponding to this effective diffusivity will, in the absence of any other effects, occur at a rate equal to that during thermal cycling. Interestingly, no primary creep occurred at the beginning of the thermal cycling experiments, although no further note was taken of this effect.

Sato and Kuribayashi [8] derived a more sophisticated model of internal stress plasticity based on continuum micromechanics to model experiments in CTE-mismatch plasticity of particulate-reinforced composites (Al-SiC). This model rests on several basic distinct assumptions: the matrix materials behaves plastically (or according to power-law creep), the particle (inclusion) is spherical and strong (does not yield), and internal stresses are generated by thermal mismatch between the two constituents. The authors assert that flow is created not only by (1) creep due to external stress and (2) plastic flow accommodation of the matrix due to internal stress during heating and cooling, but also (3) by diffusional accommodation *of the inclusion* due to the misfit strain left in the matrix around it. While this may indeed be an important consideration, it seems more likely that diffusional accommodation would occur (if at all over the time scales involved) in the matrix itself; the weak matrix surely can diffuse or creep faster than the "strong" particle to accommodate the strains and resultant stresses. Similar to the model presented by Wu et al. [7], the internal stress after the matrix ceases to yield is the yield stress, still large enough to cause flow by creep. Nevertheless, the result is a complete, closed-form solution, which applies equally to heating and cooling without the need for arbitrary sign changes due to the tensor-based approach. In the process of the derivation, several other useful relationships are derived, including the fact that stresses in the matrix are purely deviatoric, and that deviatoric stress has two components: one which is spatially constant, and one that is spatially variant. It is also noted that the inclusion is in a state if purely isotropic stress.

2.3 *MATERIALS*

2.3.1 *Properties*

Zirconia (ZrO_2) is found in nature as the mineral baddleyite, often mixed with the similar oxide hafnia (HfO_2). Zirconia has a molecular weight of 123.2 g mol^{-1} and is white or clear in its fully oxidized condition. In its pure form, zirconia exists in three well-defined polymorphs (most zirconia data here may be round in ref. [2]): monoclinic (m), tetragonal (t), and cubic (c) (a high pressure orthorhombic form also exists). The monoclinic phase is stable to about 1200°C, has a theoretical density of 5.68 g cm^{-3}, and a coefficient of thermal expansion of 7.0×10^{-6} K^{-1}. At about 1200°C upon heating, the tetragonal form of zirconia is created ($m \rightarrow t$). This phase transformation causes a remarkable 6% volume change (2% linear strain) leading to a density of 6.05 g cm^{-3} [1]. The linear coefficient of thermal expansion at that temperature is 12×10^{-6} K^{-1}. It has been found that the phase transformation is a martensitic one, requiring no diffusion of atoms, and thus occurs quite rapidly after nucleation [29]. However, the reaction is nucleated heterogeneously, leading to significant supercooling during the reverse ($t \rightarrow m$) transformation that depends, among other things, on the size of the transforming grains [30]. The grain size dependence of the transformation is due to the fact that nucleation occurs on impurities, dislocations, or defects and, once the reaction begins, proceeds in a military fashion; larger grains will contain more nucleation sites, thus decreasing the amount of undercooling necessary to create the statistical conditions necessary for transformation [31]. The hysteresis can be as large as 500°C for very fine-grained material [32]. In addition, there is some evidence that constraining stresses can suppress the phase transformation even further [33]. Above 2370°C the cubic phase is stable, and ZrO_2 melts at 2680°C.

Early attempts to form pure ZrO_2 into dense shapes were often unsuccessful [34] since the spontaneous phase transformation during cooling from sintering temperatures created internal stresses far in excess of the material strength. The result was cracked and often shattered parts. However, additives of other oxides such as calcia (CaO), magnesia (MgO), yttria (Y_2O_3), or ceria (CeO) alter the transformation temperature, stabilizing the structure of zirconia in either the tetragonal or cubic form. Although the exact temperatures of transformation vary with the material grain size, two general classifications of stabilized zirconia have come into recognition in engineering practice [2]. Fully stabilized zirconia is completely cubic in form, has a high index of refraction, and is often used in single crystal form in jewelry. Tetragonal zirconia polycrystals (TZP) stabilized with yttria typically contain > 3 mol percent Y_2O_3 and are made up of tetragonal crystals with a significant fraction of cubic grains, depending on the thermal history of the material. Partially stabilized zirconia (PSZ) stabilized with yttria contains approximately 3 mol. percent Y_2O_3, which decreases the thermodynamic equilibrium allotropic transformation temperature to near room temperature. It is this material which has received the most attention as an engineering material, as the phase transformation may be activated by stress; the large increase in volume accompanying the transformation arrests growing cracks in the material, contributing to an increase in toughness. ZrO_2-3% Y_2O_3 is often referred to as transformation-toughened zirconia, and it is at this level of yttria addition that a local maximum in material toughness is found.

This increased toughness lends to application of PSZ in wear-resistant parts such as scissors, knives, and other cutting tools [2]. In addition, zirconia is an excellent refractory, often used in insulation and refractory bricks. Zirconia also is conductive at high temperatures, leading to its use in resistive heating elements for very high temperature furnaces. One of the most exploited properties of zirconia, however, is its oxygen ion conductivity – ZrO_2 is one of the most common materials used as an oxygen ion conductor in fuel cells and oxygen sensors.

2.3.2 *High temperature mechanical behavior*

In order to fully comprehend the behavior of zirconia ceramic composites during internal stress enhanced plasticity, a review of prior research of its high temperature behavior is in order. While there has been much interest in the behavior of various stabilized forms of zirconia, the demonstration by Wakai et al. [35] of over 100% deformation of a fine grained 3 mol.% yttria partially stabilized zirconia (3Y-PSZ) has spurred research on that material over a wide range of testing conditions. The highlights of an excellent review of creep in ceramics by Chokshi [11] are summarized here, with an emphasis on the behavior of material tested under circumstances similar to those used in the experimental work described in section 3.

The parameters of interest in the creep and superplastic properties of ceramics are given in the following general model of high temperature steady-state flow:

$$\dot{\varepsilon} = \frac{ADGb}{kT}\left(\frac{b}{d}\right)^p\left(\frac{\sigma}{G}\right)^n, \qquad (11)$$

where A is a dimensionless constant, D is the diffusion coefficient (which incorporates the activation energy, Q, as above), G is the bulk modulus, b is the burgers vector, k is Boltzmann's constant, T is the absolute temperature, d is the material grain size, σ is the applied stress, p is the reverse grain size exponent, and n is the stress sensitivity. Chokshi's article tabulates the corresponding experimental values of several of these factors. Over a wide range of experimental conditions, stress exponent values ranged from n=1-3, while experiments performed at low temperatures ($1000°C \leq T \leq 1250°C$) and low stresses ($\sigma \leq 20$ MPa) resulted in n=1.0-1.9. Strain rates were reported at 10^{-8} s^{-1} for the lowest stress and temperature values, and as much as 10^{-3} in the upper limit of this parameters. Experiments yielding n=2 were considered to represent creep occurring by grain boundary sliding or grain boundary dislocation motion, two of the proposed mechanisms for superplastic behavior. Grain size was found to play a significant part in experiments under all conditions, with exponents raging from p=1.5-3.0. Activation energy for creep varied widely, with most reported values between 560-600 kJ mol^{-1} for lower temperature creep. These values represent testing performed by a variety of researchers on high density materials under compression from a variety of manufacturers (including Tosoh). A number of causes for the wide range of values were proposed, including variations in impurity content, effects of testing atmosphere, grain growth occurring during sample ramp and soak, and testing method used (bending, compression, and tension were cited in the review).

One general trend in the summarized information is a transition from $n \approx 2$ at high (>20 MPa) stresses to $n \approx 3$ at lower stresses (at $T \approx 1450°C$). Bravo-León et al. [36] attribute this effect to a threshold stress to superplastic flow phenomena. However, experimental evidence suggests that the lower stress sensitivity (and low strain rates) of low-temperature, low-stress experiments is likely due to diffusional flow rather than the grain boundary processes which could be associated with the threshold stress. It is generally well agreed that no intragranular dislocation creep occurs at the stresses and temperatures of interest in the review, and Chokshi presents some experimental evidence in support of this assumption. Several important microstructural phenomena are also noted. During superplastic conditions, the grains in the materials retained an equiaxed shape, and failure typically occurred by the accumulation of internal cavitation damage. The density loss due to cavitation reached as much as 7%. Bravo-León [37] further observe that the extent of cavitation damage increases with decreasing applied stress.

	ZrO_2 + 3 mol% Y_2O_3		Pure ZrO_2	
Young's Modulus (GPa)	110	(1200°C)	(same)	
	200	(25°C)		
Poisson's Ratio 0.27	0.20	(m)		
Density (g·cm-3)	6.05	(25°C)	5.68	(m)
			6.10	(t)
CTE (10-6 K-1)	10	(200°C)	7	(m, 1200°C)
			12	(t, 1200°C)

Table 2.3.1. Table of relevant engineering properties for partially stabilized zirconia (PSZ) and pure zirconia. Monoclinic properties are indicated by "m" and tetragonal properties by "t".

3. EXPERIMENTAL

3.1 *TESTING APPARATUS*

A high temperature stress testing apparatus capable of applying low stresses (< 100 MPa) up to relatively high temperatures (1300°C) was assembled and tested. The main components of the system were the electromechanical testing system, radiant furnace, temperature control system, and data acquisition unit.

3.1.1 *Mechanical testing system*

An Instron (Canton, MA) load frame (model 1361) with electromechanical actuator (model 3800) was chosen to perform tension and compression testing. This is a screw-type actuator capable of a displacement rate as low as 1 μm per hour and as high as 350 mm per minute, with a resolution of 0.05 μm. This electromechanical system was chosen over available hydraulic systems since it is able to operate at much slower constant strain rate than a valve controlled fluid actuator. Stroke (displacement) is measured at the actuator with a linear voltage displacement transducer (LVDT) to 1 μm resolution.

The analog electronics (Instron model 2150) provide closed-loop control of position, strain rate, or load with an attached load cell. An Interface (Scottsdale, AZ) 500 lb. (2224 N) maximum capacity load cell (model 1010AJ-500) was chosen to provide load feedback during operation in constant load control, and was attached to the analog electronics with an appropriate connector. The electronics were calibrated for linearity of the LVDT and load cell, and the proper scale settings on the electronics were determined and set. It was determined that the load required for testing would not exceed 100 lb. (445 N); likewise, the maximum sample displacement was not expected to exceed 10 mm. The ranges and output of the electronics were set as such.

The crosshead on the Instron was moved to approximately 1.5 meters above the actuator base to leave ample space for the furnace as well as to thermally separate the heat-sensitive load cell from the hot zone. The load cell was affixed directly to the actuator base, rather than the top of the column, to avoid rising drafts of heated air. For the tension tests, a load "train" which was held together by pins to ensure that applied tensile forces would remain uniaxial and self-aligning. At the top of the column a coupler incorporating a universal-joint was affixed, then pinned to a stainless steel coupler, with a lower pin hole offset 90° to that at the top. A similar configuration was used at the bottom, without the universal-joint. A water-chilled copper collar was clamped to the stainless steel coupler above the furnace to cool the steel parts, while a small fan cooled the lower connector.

Silicon carbide pullrods were machined from Carborundum (Niagara Falls, NY) Hexoloy 13.5 mm diameter rod to 200 mm in length to extend into the heated zone. The rods slid into the stainless steel couplers and were affixed with a steel pin, allowing several degrees of angular rotation. At the other end of the rods, a slit was cut in which the flat tensile samples were inserted, with a pin-hole drilled perpendicular. A drawing of these pull-rods has been included in appendix 1. The compression testing setup also used the SiC rods, but they were machined and polished to create low-friction parallel faces. In addition, the universal joint was removed and all the pinned joints were clamped to provide rigid and parallel compression faces.

3.1.2 Furnace

Since the samples were to be tested in air and with rapid cycle durations, it was decided that a furnace heating directly by radiation should be used. Typical insulated clamshell furnaces would have too much thermal mass to heat and cool quickly enough, while other types of inductive furnaces require an inert atmosphere or vacuum, which can pose problems with the testing of an oxide. The Research, Inc. (Eden Prarie, MN) E4-10 radiant furnace was used to focus the radiant energy of four 254 mm long tungsten filament lamps with parabolic polished aluminum reflectors onto the sample, for a total of 8 kW of available flux power. The reflectors are water-cooled, keeping the thermal mass low, and the furnace is able to heat a small sample at 100 $K \cdot s^{-1}$. The entire furnace was mounted on the Instron load frame, in a custom designed bracket to hold the heated zone in line with the tensile axis of the mechanical tester. The furnace was controlled by a Model 663 240 VAC continuously variable flux output phase-angle power controller, also made by Research, Inc., which was interfaced with the temperature control loop, as discussed below. The top and bottom furnace openings were packed with alumina high temperature insulating fiber.

3.1.3 Temperature measurement and control

The sample temperature was monitored by an 0.010" wire R-type unshielded thermocouple (model P13R-010) which was purchased from Omega Engineering (Stamford, CT) and insulated with Omegatite ceramic insulation. The small bead and white insulation were chosen to minimize the thermal mass and radiant absorption, respectively, which could skew the temperature measurement. The thermocouple assembly contacted the sample gage through a small (10 mm diameter) access port through the side of the upright furnace. The temperature was controlled with a programmable Omega controller (model CN-3003-F3).

This temperature controller was chosen for its ability to obey temperature profiles with up to 255 segments and cycle repetition, a requirement for thermal cycling experiments. The furnace power (flux) controller was regulated with a closed 4-20 mA current loop.

K-type thermocouples were also affixed to several other places on the apparatus to monitor the uniformity of the experimental conditions during testing. Temperature was measured on the load train above and below the furnace to monitor the effectiveness of the cooling system. The furnace case and ambient air temperature were also recorded.

3.1.4 Data acquisition

A Keithley KDAC-500 data acquisition unit with installed analog voltage and thermocouple input boards was connected to a Dell computer running Labtech Notebook 4.3.5 data acquisition and control software. The Instron control electronics provided real-time analog (0-10V) signals for load and stroke, and the temperatures listed above were monitored by the acquisition setup. All the data was sampled real-time at 1 Hz and simultaneously displayed in plots versus time on the computer display.

3.2 HIGH TEMPERATURE EXPERIMENTS

3.2.1 Procedure

High temperature tensile and compression experiments were conducted on 5% and 10% composite samples as well as pure PSZ (0%) control samples. Testing was performed at 5, 10, and 20 MPa, stresses high enough to allow measurable flow rates ($> 10^{-8}$ s^{-1}) while low enough for transformation-mismatch superplasticity to occur. These tests were actually performed under constant load, not stress; however, since the accumulated strain was no more than 10%, it is a close approximation to true stress. For further compatibility between tests, all samples (except the last two) were tested for equal durations. All experiments were performed in laboratory air.

The general methodology for performing high temperature tensile and compression testing was the same. The Instron electronics, actuator, data acquisition unit, and cooling water were all switched on for at least an hour prior to each run. The sample was ultrasonically cleaned in acetone and wiped off with methanol prior to insertion in the furnace. The furnace interior as well as the silicon carbide rods were also cleaned with methyl alcohol to avoid contamination of the samples. The samples were inserted in the load apparatus with plastic tongs, then a small holding load (less than 100 kPa) was applied to the samples. The R-type thermocouple was slid into place such that a small spring force held the bead against the wide edge of the sample, directly in the middle of the testing gage.

Thermal cycling experiments were performed over the temperature profile shown in figure 3.1.1. The samples were heated to 200°C in 12 minutes, then ramped to 1250°C at 15 °C·min^{-1}. That temperature was maintained for a 60 minute soak to bring the system to thermal equilibrium, then the temperature was taken through one thermal cycle (no load) to reach a steady-state thermal profile in the furnace before stress testing. Thermal cycling was performed between 950°C and 1250°C with linear heating and cooling rates of 30°C·min^{-1} and a 1 minute hold at either temperature. A thermal cycle in this context refers to cooling the sample from 1250°C to 950°C then heating back to 1250°C, resulting in a 22 minute complete loop. These experimental conditions were determined based on the results of several exploratory experiments, described below.

The deformation behavior of composite samples tested during thermal cycling were compared with creep tests on composites at the *isothermal effective temperature*, T_{eff}. This is the temperature at which the steady state creep rate of a pure PSZ sample would be the same as the average strain rate over a 1250-950°C thermal cycle. This temperature was calculated to be 1451K (1178°C) by performing an averaging integration of equation (11) with Q=580 kJ·mol^{-1} (based on prior results described in [11]) over the thermal cycle, as shown in appendix 2. Notice that T_{eff} is higher than the average temperature (1100°C) of the thermal cycle. Samples tested isothermally at T_{eff} were heated to 200°C in 12 minutes, then ramped to 1178°C at 15 °C·min^{-1} (70 minutes). Samples were then maintained at that temperature throughout the experiment.

Load was applied to the sample after 164 minutes of ramp and thermal conditioning in both types of experiments. Strain was set to zero 15 seconds after the load was applied. At the end of the experiment, the sample was unloaded and cooling was initiated immediately. Load was applied and removed over 15 seconds to avoid shocking the sample. Cooling was controlled at 15 °C·min^{-1} to 200°C, then the samples were allowed to cool naturally.

3.2.2 Experiments performed

As was mentioned earlier, three main variables are under investigation in this work. First is stress level, which was set at 5, 10, and 20 MPa. Second, three thermal profiles were investigated: 1178°C, 1250°C, and cycling between 950°C and 1250°C. It was estimated early that the strain rates resulting from testing isothermally at 950°C would be unmeasurable, thus these experiments were not performed. The third experimental variable is particulate volume fraction, designated as 0%, 5%, and 10%. In addition to these three main variables, samples were also tested in compression and tension. A second experiment was also run on several samples, adding yet another dimension to the experimental matrix. The variables measured to determine the relationships are total strain and strain rate.

A full factorial experimental plan to determine a constitutive equation for these variables would involve (3 stresses) x (3 volume fractions) x (3 temperature profiles) x (2 experiment types) = 54 experiments. Inclusion of a second run brings this total to 108 experiments, and proper certainty can only be ascertained after a repetition, leading to 216 necessary experiment. However, due to (1) limitations of time, (2) a finite number of samples, (3) problems with some experiments, and (4) prior work, a subset of these experiments were performed, and a smaller subset yielded relevant data.

Several preliminary exploratory experiments were performed for a basic understanding of the thermal shock characteristics, primary creep, mechanical integrity, and physical characteristics of the samples before beginning the controlled experiments. First, an experiment was performed to determine the sensitivity of the experimental setup to length changes of the sample (specifically, whether it could resolve the phase transformation). A 10% sample was cycled at several heating and cooling rates (0.25, 1.0, and 5.0 $^\circ\mathrm{C{\cdot}s^{-1}}$) under zero applied load. It was found that the equipment lacked the sensitivity to measure the phase dilatation of the sample, expected to be on the order of $(1/3)\cdot f\cdot(\Delta V/V) = 0.2\%$ if the elastic strains are relaxed by plastic deformation. Next, four exploratory runs were performed, all on 10% composite tensile samples to gain a working understanding of the experimental materials at high temperatures.

All of the controlled transformation-mismatch superplasticity (TSP) experiments were performed under the conditions described in section 3.2.1, and a summary of these experiments are listed in appendices 3 and 4. Tensile experiments were performed under cycling and isothermal conditions, on samples with 0, 5, and 10% ZrO_2 particles, and at 5 and 10 MPa stress only, yielding 12 separate experimental conditions. Many samples fractured during the experiments; those that did not were tested for subsequent runs under identical conditions. In addition, two pure PSZ (0%) samples were tested isothermally under 5 MPa at 1250°C to determine the behavior of the material at high temperature. Experiments were initiated for all 13 conditions, but only samples under only 10 of those survived application of stress for sufficient duration. In all, 30 experiments were initiated under those 10 conditions. Only 13 of the experiments survived full (25 cycle) runs: of those, 7 were under the 12 original conditions, 5 were subsequent runs, and 1 was a trial run on scrap material. Thus, there is adequate information for only following conditions: cycled- 5 and 10 MPa; 0, 5, and 10% (some multiple runs); isothermal- 5 MPa only; 0, 5, and 10% (some multiple runs). All samples were tested in the as-received conditions.

Compression tests were performed on pure PSZ (0%) and PSZ-5% ZrO_2 material only due to lack of PSZ-10% ZrO_2 materials. Most testing was performed at 10 and 20 MPa, while several were at 5 MPa. Ten experimental conditions were investigated: 0% material cycled and isothermal at 10 and 20 MPa (4 experiments); 5% material cycled and isothermal at 5, 10, and 20 MPa (6 experiments). All samples were run under stress for 9.2 hours, except for the 5 MPa runs which were held for 16.5 hours. No high-temperature (1250°C), or subsequent (second-run) experiments were performed. Twenty-one total experiments were initiated, with three ended early due to experimental difficulties, yielding 18 full-length experiments. 4 experiments were repeated on new samples 3 times, while 3 experiments were repeated on new samples 2 times. Experiments were performed on as-received samples until it was found that density variations were problematic. Several experiments were repeated on re-sintered samples. Sintering was performed as described below at 1500°C for 2 hours, but with 5°C per minute ramping. The experiments on re-sintered samples yielded good results for the following 6 experiments: 5% material tested isothermally and during cycling under 5, 10, and 20 MPa. These are also summarized in appendix 4.

3.3 MATERIALS

3.3.1 Powder preparation

A review of the literature on zirconia [11] revealed several major sources of stabilized zirconia for academic studies. Powder from Tosoh Corporation is widely used, quite pure, and was reported to sinter reliably to high density; thus it was chosen for this work. Tosoh TZ-3YB powder from lot number Z304073B was used for all experiments. The as-received powder has a compositional purity as follows, in weight percent: $5Y_2O_3$, <0.005 Al_2O_3, 0.008 SiO_2, <0.002 Fe_2O_3, and 0.021 Na_2O. The average crystallite size is 280 Å, and the powder is pre-mixed with an acrylic pressing binder. It pours to about 1 $g\cdot cm^{-3}$, or 17% theoretical density. The powder was used as-received during processing.

Pure zirconia for the particulate reinforcement phase was also purchased from Tosoh. As-received, the Tosoh TZ-0 powder was made up of very small (270 Å) crystallites which caused a very large hysteresis of the heating and cooling transformation temperature. The material as-received transforms from monoclinic to tetragonal at 1225°C during heating, and from tetragonal to monoclinic at 975°C during cooling, based on differential scanning calorimetry (described below). Thus, the transformation temperature increases for larger grained material, decreasing the hysteresis. A smaller hysteresis for transformation-mismatch superplasticity testing allows a narrower range of temperature cycling and thus more rapid thermal cycling. It was decided therefore that the particulate material should be coarsened to achieve larger grains.

David Lee [38] performed some coarsening studies on Alfa Aesar Puratronic ZrO_2 by annealing powder at 1475°C for 24 hours. Based on the positive results of this work, it was decided to repeat that schedule on the Tosoh powder, in addition to a longer run at 1650°C for 48 hours. The 1475 °C coarsening was performed in an open-air Lindberg box furnace (model 51333), and the 1650 °C coarsening was run in an Lindberg crucible-style furnace. Both powder batches were poured in a high-purity alumina crucible purchased from Alfa Aesar and tapped to pack. The powders coarsened at the higher temperature had a decreased hysteresis for transformation (see section 4.1) and were chosen for use in the composites. The coarsened powders densified somewhat during coarsening and were broken up with a mortar and pestle. The crushed powders were then separated by size with a series of sieves between 25 and 63 μm. Roughly 50% of the powder after crushing was between 32-38 μm, and this batch of powder was used in the final experimental samples.

3.3.2 Processing

Small parallelepipeds of Tosoh TZ-3YB as well as composites were created by pressing and sintering in a dual-plunger (floating) uniaxial die press for early laboratory studies. Matrix and reinforcement powders for 5% and 10% composites were measured on an analytical scale and poured together into polyethylene bottles. The bottles were placed on a rolling mill (without milling media) for several minutes to ensure complete mixing. Powder was poured into the stainless steel die of rectangular cross-section, 25.4 by 8.3 mm, and tapped to 15-20% density. Samples were pressed at 70 MPa in the die lubricated with hydrocarbon oil on a Carver Model C laboratory bench hydraulic press to roughly 50% green density. The samples were placed on a high purity (99.7%) alumina rectangular plate which was cleaned with methanol. The samples were sintered in a Lindberg tube furnace (model 54233) for 2 hours at 1500 °C with 2 °C per minute ramp rates, except through the transformation cool (1300°C to 750 °C) and the dewaxing ramp (25°C to 750°C), which were run at 1°C per minute.

Samples for high temperature stress testing were created by uniaxial hot pressing at Malyn Industrial Ceramics Incorporated (Akron, NY). After a review of prior work in hot pressing techniques [39], samples were sent for hot pressing under vacuum at 25 MPa in a graphite die 38 mm in diameter. The 10% composite tensile samples were hot pressed for 30 minutes at 1400°C, while the 0% and 5% material was hot pressed for 45 minutes at 1500°C. The three billets of material formed by hot pressing were 40-50 mm in height and were black in color throughout due to slight loss of oxygen. Follow-up experiments revealed that a one hour anneal at 1000°C was sufficient to return the samples to fully oxidized (white) condition. It was found that this anneal caused no change to the material density or dimensions; thus it was decided that a long anneal would be performed prior to stress testing in the main experiments.

Tensile and compression specimens were machined by Bomas Machine Specialists (Somerville, MA). To create the tensile samples, 37 mm by 14 mm flat plates 3 mm thick were first cut from the cylindrical billet perpendicular to the hot pressing direction. The gage section was then ground in to create a testing area 12.7 mm long and with a constant reduced width between 2.4 - 4.8 mm (depending on the sample). Holes 4.8 mm in diameter were then drilled into the larger heads for the holding pin. An engineering drawing of the tensile specimen is shown in appendix 5. Rectangular cross-section compression samples were ground from the leftover billet pieces to blocks roughly 3 by 5 by 9 mm. The ends of the compression samples were polished with diamond paste to prevent excess friction with the compression pushrods.

3.4 CHARACTERIZATION

3.4.1 Thermal

The thermal characteristics of various powders and samples were characterized on a Seiko model 320 Differential Scanning Calorimeter (DSC). The DSC measures the differential temperature measured (under constant heat output) between the experimental sample and a thermally inert reference, yielding the temperature at which spontaneous thermodynamic changes, such as phase transformations, occur [40]. DSC was performed on (1) as-received Tosoh TZ-3YB, (2) as-received Tosoh TZ-0, (3) TZ-0 powder coarsened at 1475 for 24 hours, (4) TZ-0 powder coarsened at 1650°C for 48 hours, (5) a sintered composite sample containing 10% powder from (3), and (6) a sintered composite sample containing 5% powder from (5). DSC was performed on 10-20 mg of material in a small alumina crucible, with an equivalent amount of alumina powder in an alumina crucible as a reference. The materials were heated from room temperature to 700°C or 800°C at 50°C·min^{-1}, then ramped at 10°C·min^{-1} to a maximum temperature of 1300-1400°C (depending on the experiment). The samples were measured during cooling at 10°C·min^{-1} to 700°C or 800°C then cooled to room temperature at 50°C·min^{-1}. All experiments were performed under 50 ml min^{-1} nitrogen gas.

Dilatometry experiments were conducted on a representative 10% composite samples (13 mm x 4 mm x 5 mm) from hot pressing to determine the mechanical behavior during thermal expansion and phase transformation. Dilatometry was performed on a Netzsch Gerätebau GmbH dilatometer within an alumina sample tube and push rod. The sample temperature was monitored with an S-type thermocouple placed within several millimeters of the sample. The samples were heated under an O_2 atmosphere to 1350°C at $10°C{\cdot}min^{-1}$ and cooled to room temperature at the same rate. Overall extension (of the sample and pushrods) was recorded on a PC, which was then adjusted by a calibration curve of pure alumina to yield extension, then divided by sample length to yield expansion strain versus temperature and time.

3.4.2 Microstructural

Samples were prepared for microscopy by sectioning with a low-speed Buehler saw (model 11-1180) with a low-concentration diamond blade (model 11-4253), and subsequent mounting in bakelite. Representative composite samples tested in compression and tension were sectioned both transverse and parallel to the uniaxial testing direction. The samples were rough polished with wet #80, #500, and #1200 grit silicon carbide paper on a Struers Rotopol-1 rotational polisher, then fine-polished on cloth wheels on a Varipol VP-50 with Buehler diamond pastes to 1 μm. Reinforcement phase powders were also observed in bakelite or applied to double-sided tape on a glass slide. Samples were cleansed in ultrasonic baths of water with added detergents and rinsed fully between each polishing step and after the final polish. Optical microscopy was performed at high power, and photographs were taken on Polaroid 52 film.

The samples and powders observed with optical microscopy were also imaged with an environmental SEM to determine the matrix microstructure. Since an environmental SEM was used, the materials did not require a conductive coating for imaging, and the photographs represent the virgin surfaces.

3.4.3 Physical

Density of samples was determined on a Mettler Gram-Matic laboratory balance by the Archimedes technique. The samples were weighed normally air in the laboratory scale to yield the mass, m. Then a wire of measured mass m_{wire} was wrapped around the sample to allow it to be suspended from above. The sample was immersed in water, suspended by the wire, and attached to the balance bar. After carefully removing all observable air bubbles from the surface of the sample, the weight in water, m_W, was recorded. With careful measurement of the water temperature, T_W (which is often lower than room temperature due to evaporation), and calculation of the density of the water to several decimal places, the density of the measured sample may be calculated by the following formula:

$$\rho = \frac{m \cdot \rho_w}{m - \left(m_w - m_{wire}\right)} \tag{12}$$

It is very important that the mass values in equation (12) be measured very accurately due to the propagation of error in this equation. Using a measured error in mass of ± 0.5 mg and error in the measurement of the water density of ± 0.001 g·cm^{-3}, an expression for the error associated with a sample may be described by

$$\begin{aligned} \Delta\rho = \frac{\left(m_{wire} - m_w\right)\rho_w}{\left(m - m_w + m_{wire}\right)^2}\Delta m + \frac{m\left(1-\rho_w\right) - m_w + m_{wire}}{\left(m - m_w + m_{wire}\right)^2}\Delta m_w + \\ \frac{m\left(1+\rho_w\right) - m_w + m_{wire}}{\left(m - m_w + m_{wire}\right)^2}\Delta m_{wire} + \frac{m}{m - m_w + m_{wire}}\Delta\rho_w \end{aligned} \tag{13}$$

Inserting some typical numbers into equation (13), it is observed that a sample of mass m=1.0 g and a density of 6.0 g·cm^{-3} will have density calculated to within ± 0.05 g·cm^{-3} (± 0.83%). For typical samples greater than 5.0 g, the error drops off to a negligible ± 0.01 g·cm^{-3} (± 0.17%). Sample density was measured before and after each experiment or heat treatment. In addition, some tensile samples were sectioned to separate the gage section of interest from the heads, and the gage section only was measured for density. Sample densities are listed in appendices 3 and 4.

Sample dimensions were measured before and after every experiment. External (outside) measurements less than 25 mm were made with a Mitutoyo digital point micrometer to ± 0.001 mm, while inside measurements were taken with a Mitutoyo digital caliper with ± 0.001 mm accuracy. Tensile samples were measured for width at each head, width of the gage, length of the gage in four places, length between pin-holes, size of pin-holes, and thickness in six places. Compression samples were measured for length, width, and thickness. Three measurements were taken at each point and averaged. Damage was inspected visually before and after each experiment as well, with careful observation of cracking and other surface features. For the compression experiments, barreling, cracking, and flaring were recorded by visual inspection and subjectively rated on a scale of 0-3, where 0 corresponds to no observed surface cracking, while 3 indicates excessive splitting (compression) or fracture (tension).

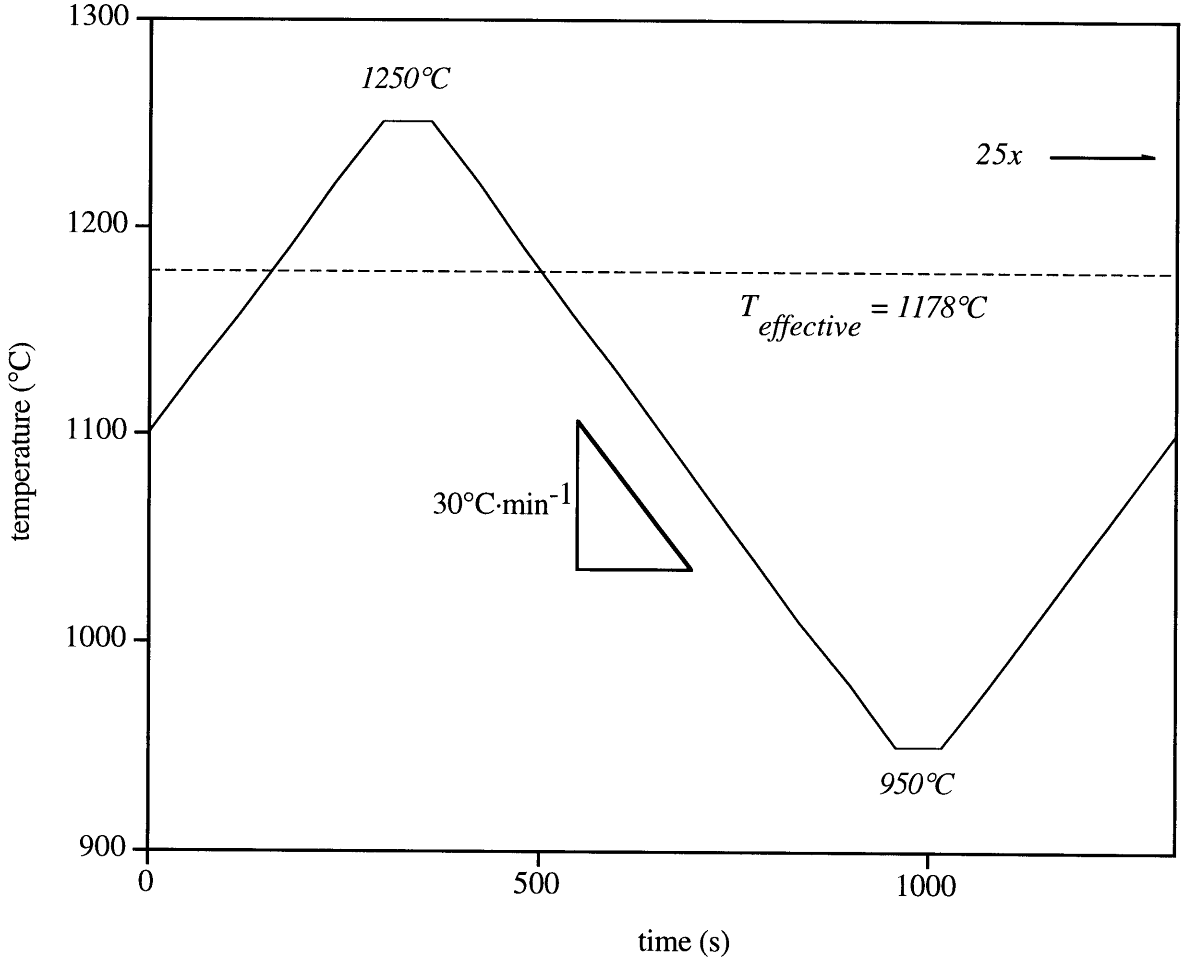

Figure 3.1.1. Schematic of the experimental cyclical temperature profile.

4. RESULTS

4.1 EXPERIMENTAL MATERIALS

Scanning electron micrographs of the pure ZrO_2 particles used in the experimental materials are shown in Figure 4.1.1 and 4.1.2. These powders, which were coarsened at 1650°C for 48 hours, then crushed and sieved to 32-38 μm diameter, still retained a quite wide variation in size and shape. There appear to be three distinct types of particles: (1) nearly spherical uncrushed particles about 30 μm in diameter, (2) rough, angular agglomerated particles (from crushing larger powders) 10-30 μm in size, and (3) individual grains or clumps of grains < 10 μm that either were not removed during filtering or which were separated from the larger powders during handling. However, most of the powder appears to be about 30 μm in size, and 38 μm may be considered an upper bound from filtering of the particles. The grain size within the individual particles may be observed in figure 4.1.2, and appears to be 5-10 μm in size.

Figures 4.1.3 through 4.1.6 show micrographs of the 10% hot-pressed material (5.85 $g \cdot cm^{-3}$) prior to creep and TSP experimentation. Figure 4.1.3 is an optical micrograph at low magnification showing the spatial distribution and size of the particles within the matrix, which indicates that the particles survived hot pressing well, without much crushing or separation. An SEM micrograph focused on a polished surface of the matrix PSZ is shown in figure 4.1.4, which shows no evidence of cracking or porosity. Figure 4.1.5 shows a typical irregularly-shaped particle in the matrix, which measures roughly 20 μm in size. Some particle breakup did occur during hot-pressing, yet a majority of the fractional particulate volume is retained in large particles such as this. What is imaged in the figure is not actually a polished surface of a particle, but, rather, a cavity from which some grains have been shed. It appears that the small particle agglomerates could not withstand the stresses created by transformation during cooling, and they seem to have cracked intergranularly within the matrix. Thus, upon sectioning with a low-speed diamond saw, the grains in the interior of the particles were ground loose, leaving behind only those grains from the particles which were well bonded to the matrix. This is observed in figure 4.1.6, a micrograph of another sectioned particle *prior to polishing*. Although the figures may not show it, it was verified by focusing depth in the SEM that the back surface of the particle cavity is indeed depressed from the level of the matrix. This conclusion is further supported by the observation during polishing with diamond paste below 20 μm of considerable contamination and scratching of the polished surface, which was an indication that more of these large grains were loosening from the sectioned particles. Evidence for loss of cohesion in the particles may have an effect on the generation of internal stress, which is discussed below. The matrix material in the 10% hot-pressed sample is observed to consist of very fine grains, 0.2-0.3 μm in size, in the rough cross-section of Figure 4.1.6. This figure is consistent with those discussed in reviews of zirconia superplasticity, in which Tosoh TZ-3YB was processed by a variety of means to a typical 0.3 μm grain size [11].

The monoclinic to tetragonal transformation properties of these powders were determined by differential scanning calorimetry (DSC), as shown in Figure 4.1.7. The figure shows the transformation temperatures during heating and cooling for the original powders, powders from the low-time and temperature (1475°C, 24 hours) coarsening, and the high-time and temperature coarsening (1650°C, 48 hours). It appears that the coarsening was successful, as evidenced by the change in the allotropic temperature during cooling from 970°C (as-received) to 1039°C (low-temperature) to 1068°C. One effect that was not anticipated is the change of the transformation temperature during heating; although it appears to only have shifted 12°C to 1226°C, the phase transformation was supposedly not dependent on nucleation and was understood to occur at a constant temperature independent of grain size during heating [31]. Another interesting trend is the narrowing of the temperature range over which phase transformation occurs during cooling and the rapid onset of transformation as indicated by DSC.

Once the powders were processed with the matrix material into composite samples, it was possible to directly measure the dilatational response of a 10% composite sample by dilatometry, shown in Figure 4.1.8. The strain response curve, plotted with respect to time, is shown along with temperature and an expected response. The expected expansion curve represents a composite coefficient of thermal expansion, α_c,

$$\alpha_c = f \cdot \alpha_p + (1-f) \cdot \alpha_m \tag{14}$$

where α_p and α_m, the coefficients of thermal expansion for the particle and matrix, are $7 \cdot 10^{-6}$ K^{-1} and $12 \cdot 10^{-6}$ K^{-1}, respectively [2]; f, the volume fraction of particles, is 0.10. This yields a composite CTE of $\alpha_c = 11.5 \cdot 10^{-6}$ K^{-1}. The sample exhibits thermal expansion slightly greater than that expected during heating and slightly less than that expected during cooling. The expectation curve incorporates a strain due to transformation calculated in a similar way as equation (14); a composite with f=0.10 particles transforming 2.0% in linear strain is expected to yield (0.10)(2.0%) = 0.2% strain by this technique. The actual strain observed during transformation is far less – about 0.03%, or a sixth of that predicted by the linear model (see section 5.1 below for a more thorough discussion). The most striking result of this experiment, however, is that the particles in the composite transform at significantly lower temperature (960-970°C, figure 4.1.7) than in the unconstrained state (1050°C, figure 4.1.8). In addition, the allotropic temperature during heating was measured to be 1165-1180°C, significantly less than the value of 1225°C observed for pure particles in DSC (figure 4.1.7). It was on the basis of these results that the temperature range of 950-1250°C during TSP was decided. A small amount of ratcheting strain was also recorded, as evident from the offset after cooling, and was measured to be about 0.025%.

The density of each material billet (0, 5, and 10%) was monitored closely. All samples from the 0% billet had a density between 5.92-5.95 $g{\cdot}cm^{-3}$, with most centering on 5.93 $g{\cdot}cm^{-3}$. These materials are 98% dense based on a theoretical density of 6.05 $g{\cdot}cm^{-3}$, the maximum possible density of TZ-3YB reported by Tosoh. Theoretical values for composite materials are calculated by a rule of mixture of the densities of the individual phases. Using the above value and 5.68 $g{\cdot}cm^{-3}$ for the monoclinic particle [2], density of 6.03 $g{\cdot}cm^{-3}$ would be expected for a 5% composite, and 6.01 $g{\cdot}cm^{-3}$ for a 10% composite. Samples from the 5% hot-pressed material were measured to have density spanning the range of 5.20–5.85 $g{\cdot}cm^{-3}$ (86-97% dense). It was discovered that a gradient of density existed axially in the billet; the material at the top and bottom were most dense, while the center had the lowest measured density (this was not noticed prior to the first experiments, since the first few samples were fairly high density). Furthermore, it was found that a radial density gradient also existed; the material in the direct center of the billet, which is where the sample gage was sectioned, achieved significantly lower density than the sample as a whole. There was also a variation in the density of the 10% samples, though less dramatic. All of the 10% samples had densities of 5.74-5.96 $g{\cdot}cm^{-3}$ (96-99% dense). The materials were uniformly black in color from a small amount of oxygen loss caused by sustained high temperatures in vacuum during hot pressing.

4.2 CREEP/TSP EXPERIMENT OVERVIEW

Figures 4.3.1 through 4.4.7 show the results of several tension and compression experiments. There were three main problems that hinder analysis of the resultant data, and of the tensile experiments in particular. Since these concerns affect how experimental data is presented, it is useful to discuss them in advance.

(1) *Cracking during the experiment:* Several experiments yielded erratic results, often with jumps in the level of strain. This can only be attributed to cracking occurring in the

heads or gage of the sample, and this conclusion is supported by observation of visible cracks in many samples after the experiments. Large cracking in the sample was also often associated with large changes in density which could not be rationalized by microstructural changes. Cracking was an uncontrollable, unanticipated experimental variable that did not occur in a steady-state fashion; thus, data cannot be adjusted for cracking to give true plastic strain rates. Experiments which indicated this type of behavior (predominantly 0% material) were not included in the calculation of steady-state strain rates. In the extreme case, many samples tested in tension fractured during the experiment; if this occurred in the gage section, accuracy in measurement of gage strain was no longer possible.

(2) *Material flow at the heads:* The tensile sample was designed to concentrate stresses on the thinned gage section of the samples; however, it was found that a significant amount of strain was accumulated in the heads, most likely caused by higher temperatures created there due to the experimental setup. In addition, cracks grew in many samples at the heads from the concentrated stress at the pin-holes and contributed to the LVDT displacement. In cases where this was the only problem (i.e. cracking was not initiated and there were no density gradations), it was assumed that flow at the heads occurred proportionally to strain in the gage in steady-state and the data was adjusted by a factor to represent the strain in the gage only. This is not a concern in compression experiments.

(3) *Density changes and gradients within the sample*: Primarily a concern with experiments conducted on 5% composites, excessive porosity centered in the gage section of tensile samples led to gradients in density and concurrent densification (sintering) of the samples during experiments. Since the local density of the gage section of the low density samples is unknown, it is impossible to correct for density changes which took place. Since the extent of this density gradiation varied from sample to sample, it is also impossible to compare the strain or displacement results with other samples. However, the data from some experiments did show creep occurring in the heads, which is presented. Smaller compression samples typically had higher density with minimal gradients, thus density variation is not a concern for those results. If density changes occurred in samples with a uniform initial density (high density tensile samples and most compression samples) and cracking was not observed, it was assumed that the changes are due a homogeneous increase in porosity or *uniform* concurrent densification.

As a result of these variations, it is estimated that the strain rate may be calculated from experimental tensile data to ±25%. For compression data, much of this uncertainty is eliminated and strain rates are presented to within ±10% accuracy. Details for each of the experiments discussed may be found in appendices 3 and 4 with the experiment name and number given in the text.

4.3 *TENSILE EXPERIMENTS*

In general, tensile tests showed strain rates on the order of 10^{-6} s^{-1}, with significant amounts of primary creep typically occurring in the first half of the 9 hour long experiments. Surface cracks were widely observed on pure PSZ (0%) samples, but very rarely in the PSZ-ZrO_2 composites.

4.3.1 *Results from tensile tests on pure PSZ (0%) composite samples*

Several pure PSZ (0%) control samples were tested in tension at 5 MPa and 10 MPa. Two samples with initial densities of 5.92 and 5.94 $g \cdot cm^{-3}$ were tested at 5 MPa under thermal cycling and isothermal conditions, respectively. While both samples encountered significant cracking in the heads, preventing any useful analysis of the resultant displacement data, dimensional measurements of the sample gage showed 6.2% strain for the cycled sample and 5.7% strain on the sample tested isothermally. There was some indication of transformation strains and/or some microcracking during cooling, evidenced by the measured head-to-head displacement being larger that recorded by the LVDT. If it is assumed that this strain occurs uniformly over the sample, the adjusted strain on the gage of the cycled sample is 4.7%, while that of the isothermally crept sample is 4.8%. The overall density of the cycled and isothermal samples was 5.25 and 5.31 $g \cdot cm^{-3}$, respectively (note that, due to cracks measured as voids by the density measurement, this is not representative of the gage section, only of the condition of the material as a whole). The similarity of these two total measures of strain indicates that the isothermal-effective temperature is determined correctly. It was noted, however, that both samples went through a region of fast strain, presumably primary creep. The primary creep range for the isothermally tested sample is discussed below. The sample which was tested through 25 thermal cycles was unmounted, measured, and tested again under the same conditions; this second run is shown in Figure 4.3.1. The sample appears to have reached a steady-state flow rate throughout the second experiment, and the strain rate, after correction for head strain, is $9.8 \cdot 10^{-7}$ s^{-1}. The sample density remained virtually unchanged, decreasing from 5.25 to 5.21 $g \cdot cm^{-3}$; 3.3% total strain was measured on the sample gage, close to the calculated value of $(9.8 \cdot 10^{-7}\ s^{-1}) \times (35000\ s) =$ 3.4%.

Figure 4.3.2. plots the results of two successive 10 MPa tensile experiments on 0% samples during thermal cycling (C2A0_10, #11 and C2B0_10, #22). Between the two experiments, the sample was unloaded, cooled, removed, measured, reinstalled, held at

temperature for several hours, and reloaded. Again, significant problems with cracking prevent the discussion of this experiment in terms of strain, but it is useful to observe the changes in recorded length which occur during the experiment. In addition, there seemed to be some contamination of the surface of the sample which appeared glassy and had small (1-2 mm) round surface craters. The overall sample density changed from 5.93 to 5.08 g·cm^{-3} during run #1, then from 5.08 to 5.05 g·cm^{-3} in run #2.

Several isothermal creep experiments were also performed on tensile samples at 1250°C under a stress of 5 MPa (H1A0_5, #7 and H2A0_5, #21). During both experiments, the samples fractured after fewer than 8 "effective cycles" (about 10,800 seconds) by failure through the heads. The strain response of both samples was similar, and it was observed that the strain rate was still decreasing through a primary regime when the samples broke. However, the results of this primary creep is plotted in figure 4.3.3 with a comparable experiment performed at 1178°C (E1A0_5) for comparison of the initial strain response of PSZ at different temperatures. Both samples were initially 5.9 g·cm^{-3}, and the strain response of the both experiments are shown without modification.

4.3.2 Results from tensile tests on PSZ-5% ZrO_2 composite samples

Two trends are evident in the 5% tensile test data. As was mentioned before, significant variation of density between samples, as well as gradients within samples prevent valid comparisons. However, one 5% sample was tested during thermal cycling under 5 MPa stress through three successive runs (C2A5_5, C2B5_5, and C2C5_5), as shown in figure 4.3.4. Although negligible strain was accumulated on the gage (less than 0.5% or 60 μm total strain occurred during each run), appreciable flow (more than 10 times that in the gage) did occur in the heads. Since the gage section was at a relatively steady-state, the results may be interpreted as a test of the material in the heads themselves. As the figure shows, the samples maintained a fairly uniform steady-state displacement rate after about 15000 seconds in the first experiment; furthermore, a steady-state was maintained through the second run, and until failure in the third run at about 18000 seconds (the tertiary creep was not shown on the plot, but the start of failure may be seen above 10000 seconds in the third run).

Another pair of isothermal tensile 5 MPa experiments (E3A5_5, E3B5_5) were also performed on a 5% composite sample without fracture. The strain measured in the gage during both runs was *less* than that measured during thermal cycling (6 μm versus 60 μm); however, these tiny strains cannot be compared realistically, especially considering that there were also density problems in these samples. However, a third experiment was performed (CEA5_5) on this sample at 5 MPa during thermal cycling. The displacement rate during this experiment was significantly greater, $1.5 \cdot 10^{-2}$ μm·s^{-1} versus $8.0 \cdot 10^{-3}$ μm·s^{-1} (about 2x), than the previous isothermal run on the same sample. The displacement data from these two experiments (isothermal run #2 and subsequent cycled run) are plotted in figure 4.3.5.

4.3.3 Results from tensile tests on PSZ-10% ZrO_2 composite samples

Two 10% composite samples were tested in tension at 5 MPa under thermal cycling and isothermal conditions (C1A10_5, E1A10_5). Unfortunately, both showed complications due to cracking and inconsistent density changes, giving no conclusive results. Another thermal cycling experiment was performed at 5 MPa on a 10% sample previously pulled to 8% strain during exploratory experiments (C0A10_5) which is shown in figure 4.3.6. This uncorrected data shows a very consistent strain rate over the latter (>10000 s) part of the run, and indicates a strain rate of $9.4 \cdot 10^{-7}$ s^{-1}. The overall sample density was 5.23 g·cm^{-3} (original density was not recorded, but no evidence of cracking was seen in displacement data or observations). A second run on the sample from the aforementioned experiment (C1B10_5) showed a similar strain rate.

4.4 COMPRESSION EXPERIMENTS

Since there were far fewer complications from head creep and cracking, data from compression experiments is more easily interpreted. In addition, density was typically higher and more constant, since all compression samples were machined from the extremities of the hot-pressed billet; however, the small size of the samples magnify the errors in density measurement (±0.05 g·cm^{-3}). One concern in particular that arose with compression experiments is enhancement of observed primary creep due to "settling" of the compression platens which was not a problem in tensile testing due to the self-aligning load train. If the faces of the compression samples were not parallel to within several μm (less than 1° of angle), the beveled edge in contact with the compression platen would relax under high stress until the full face of the sample contacted. It was estimated that all settling should be completed within 10000 seconds; thus the beginnings of most experiments have been omitted. All experiments were performed on pure PSZ (0%) and PSZ-5% ZrO_2 samples, and most at 10 or 20 MPa; no successive experiments were performed on any compression samples.

4.4.1 Results from compression tests on pure PSZ (0%) samples

Pure PSZ (0%) materials tested in compression were measured to have density between 5.87-5.98 g·cm^{-3}. After compression testing, all samples were often found to be cracked or split along the compression axis, preventing both accurate measurement of final density and accurate interpretation of some of the displacement results. One isothermal and one thermal cycling experiments were performed at 10 MPa (CCA0_10, #1 and EDA0_10, #17); problems occurred during the thermal cycling experiment which caused loss of control over the load, thus cracking the sample. It will not be discussed here. The isothermal (1178°C) experiment, however, yielded reliable data which is shown in figure 4.4.1. After a sharp drop in displacement which was likely caused by settling (confirmed by the low value of measured strain compared to that shown in the data), the sample crept at a steady-state $4.5 \cdot 10^{-7}$ s^{-1}. This result is questionable, however, since the sample did exhibit severe splitting upon subsequent observation.

One isothermal and two thermal cycling experiments were performed at 20 MPa (CCA0_20, #8, CDA0_20, #9, and ECA0_20, #11). The first thermal cycling experiment ended early due to equipment malfunction, thus only the first several cycles are valuable. The second sample stressed during thermal cycling flared severely and showed a large amount of strain as a result; it will not be discussed here. The isothermal experiment was more successful, and is presented in figure 4.4.2 along with the several thermal cycles of the first experiment mentioned above. The results shown in figure 4.4.1 are also presented in 4.4.2 for comparison. The primary creep behavior appears to be similar for both thermal cycling and isothermal creep for the 0% material under 20 MPa of stress. Although both samples were cracked during the experiments, the final measured strain was similar — 4.0% and 4.2% for the cycled and isothermal experiments, respectively. Again, final density was not measured, due to excessive cracking.

4.4.2 Results from compression tests on PSZ-5% ZrO_2 composite samples

A number of experiments were also performed on PSZ-5% ZrO_2 composites in compression. Although it was expected that these samples would not be hampered by variations in density since they were machined from the extremities of the billet, a range of densities was still observed, from 5.44 to 5.98 $g \cdot cm^{-3}$. Observable sample splitting and fracturing was much less prevalent than in the 0% materials, but some evidence of cracking was still found in density measurements as well as in the displacement data.

Several experiments were performed at 10 MPa, during both thermal cycling and isothermal creep. All three experiments performed at 10 MPa showed some evidence of cracking in the form of displacement drops in the data; there were problems with equipment water cooling as well, and these experiments will only be summarized, in favor of the results of experiments on sintered samples, discussed below. It was observed, however, that a steady-state strain rate of $4.9 \cdot 10^{-7}$ was maintained on an isothermal creep experiment

(ECA5_10, #3); however, the density of the sample, which decreased from 5.89 to 5.33 g·cm^{-3} during the run, suggests significant cracking. Interestingly, an experiment repeated under the same conditions (EDA5_10, #10) also displayed evidence of cracking in the displacement data, but the density as measured actually increased from 5.61 to 5.77 g·cm^{-3}. The early part of this experiment (before evidence of cracking) is shown in figure 4.4.3 for comparison with a similar isothermal creep experiment on a 0% material (from EDA0_10, figure 4.4.1). In this figure, it is shown that the pure material does creep slightly faster than the composite, but its behavior is very similar.

The results of creep and thermal cycling experiments performed on PSZ-5% ZrO_2 at 20 MPa will also be largely deferred in favor of experiments on sintered samples due to density and cracking complications (see CCA5_20, #5, CDA5_20, #15, ECA5_20, #12, and EDA5_20, #16 in Appendix 4). Similar to the tests above, density typically decreased, and cracking was observable in the data but rarely visible on the sample surfaces. All experiments had similar measured strains, from 5.7 to 6.4%, and there was virtually no difference between thermally cycled and isothermally crept samples. However, internal cracking and density changes significantly decrease the resolution within which accurate conclusions may be made.

4.4.3 Results from compression tests on sintered PSZ-5% ZrO_2 composite samples

Several of the above compression tests on 5% samples were repeated on re-sintered samples. 5% composite compression samples with very low density (4.9-5.2 g·cm^{-3}) were re-sintered to very high density (5.82-6.01 g·cm^{-3}) for these tests. Two experiments, one isothermal and one thermally cycled, were each performed at 5, 10, and 20 MPa. These experiments provided the most consistent results, with fewer complications due to cracking and density changes. The six samples had no observable cracking, flaws, barreling, or flaring of the ends; the samples after testing looked nearly identical to initial conditions except for the accumulation of 0.8-2.1% compressive strain. In the figures discussed below, the first several minutes of the experiments have been omitted, since it was discovered that a significant amount of displacement occurred due to "settling" of the slightly non-parallel faces to the compression platens. However, it was observed for all three stress levels that the extent of this was always greater for the isothermal experiments than the thermal cycling ones; but since the experiments were not properly configured for the analysis of primary creep, this effect cannot be considered conclusively.

Figure 4.4.4 shows the strain response of the two experiments performed at 5 MPa, yielding steady-state strain rate of $1.3 \cdot 10^{-7}$ s^{-1} during thermal cycling and $0.85 \cdot 10^{-7}$ s^{-1} during isothermal creep. Both samples appeared to have decreased slightly in density, possibly indicating the formation of porosity. The density of the sample in the thermal cycling experiment decreased from 5.82 to 5.91 g·cm^{-3}, and that of the isothermal experiment decreased from 6.01 to 5.98 g·cm^{-3}. Such a decrease in density could be attributed to the formation of cracks; however, no evidence was found in the data or during visual inspection which would indicate this, as was obvious in other experiments where excessive cracking occurred. The minor cyclical fluctuations in the data are a result of the correction factor used to incorporate data from the cool point of individual cycles, and are typically within the 10% experimental error considered in this analysis.

Figure 4.4.5 depicts similar results for isothermal and thermal cycling experiments performed under 10 MPa of compressive stress (ESA5_10, #14, and CSA5_10, #13). Similar to the results from 5 MPa testing, the strain rate during thermal cycling was greater than that during isothermal creep. The steady-state strain rate was measured by linear fit to be $3.9 \cdot 10^{-7}$ s^{-1} during thermal cycling and $2.0 \cdot 10^{-7}$ s^{-1} for isothermal creep. There was again evidence of some porosity formation in the density results; the sample tested isothermally changed from 5.86 to 5.85 g·cm^{-3}, while the sample tested in thermal cycling changed from 5.91 to 5.84 g·cm^{-3}.

The results of the 20 MPa compression experiments are shown in figure 4.4.6. These experiments do not show the same trend as in the case of 5 and 10 MPa. Instead, the strain rate during thermal cycling is $4.4 \cdot 10^{-7}$ s^{-1}, while isothermal testing caused strain at $5.3 \cdot 10^{-7}$ s^{-1}. However, while direct measurement of the cycled sample confirms the 2.1% strain evident in the data, only 1.7% strain was measured on the isothermal sample, compared to the 2.3% strain predicted by displacement data. Also unlike most previous experiments, both samples were found to have *increased* in density during the experiments; the density of the sample tested isothermally increased from 5.95 to 6.00 g·cm^{-3}, and that of the sample tested in thermal cycling increased from 5.93 to 5.97 g·cm^{-3}. If this density change occurred homogeneously throughout the samples, this would correspond to a 0.2% linear strain. The results from compression of PSZ-5% ZrO_2 sintered samples deformed isothermally at 1178°C are presented in figure 4.4.7 for comparison of the isothermal creep behavior of the samples at the three levels of stress under investigation.

4.5 MICROSTRUCTURAL EVOLUTION

Following the observation of density decreases in samples, a microstructural investigation of tensile samples was performed. Figure 4.5.1 shows a high resolution SEM micrograph of the matrix PSZ (far from any particles) in a 10% composite sample pulled in tension during thermal cycling to 4.4% linear strain. This photograph represents a cross-section perpendicular to the direction of applied stress. In comparison with figure 4.4.1, it is seen that significant porosity has developed, most likely due to creep damage or internal stresses. The bulk tensile sample density decreased from 5.85 to 5.26 $g \cdot cm^{-3}$ during the experiment (corresponding to 12% porosity by volume), which is easily accounted for by porosity observed in the figure. This sample was not observed to have cracked at the surfaces or in the sample heads.

Figure 4.5.2 shows an optical micrograph of the same sample at low magnification in a cross-section parallel to the testing direction. Two interesting observations may be made in this figure. First, there appears to be a slight elongation of the particles in the direction of the applied stress (vertical). In addition, many small cracks may be observed in the matrix, typically stemming from the particles, and often bridging between them. These features are not observed in the comparative as-received composite material, shown in figure 4.1.3. Figure 4.5.3 shows an SEM micrograph of a fractured surface of a 10% composite which was broken while at high temperature and under tensile stress. This figure again demonstrates the 5-10 μm particulate grain size as well as the 0.2-0.3 μm matrix PSZ grains which were found in figure 4.1.6, indicating that excessive grain growth at the moderately high experimental temperatures is not of great concern.

4.6 FIGURES AND ILLUSTRATIONS

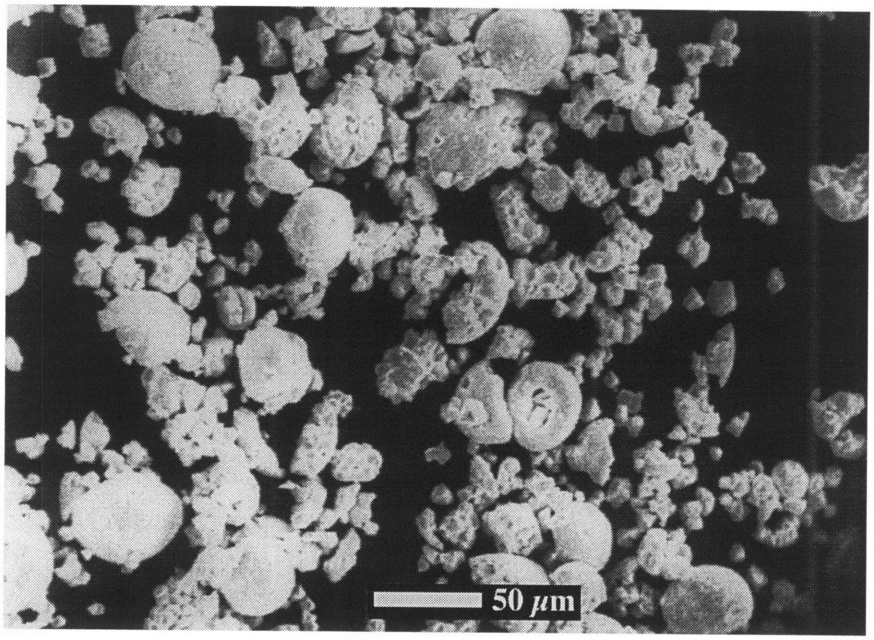

Figure 4.1.1. SEM micrograph of the coarsened ZrO_2 powders used in the composite samples. Original size range was 32-38 μm, but some particle fragmenting has occurred.

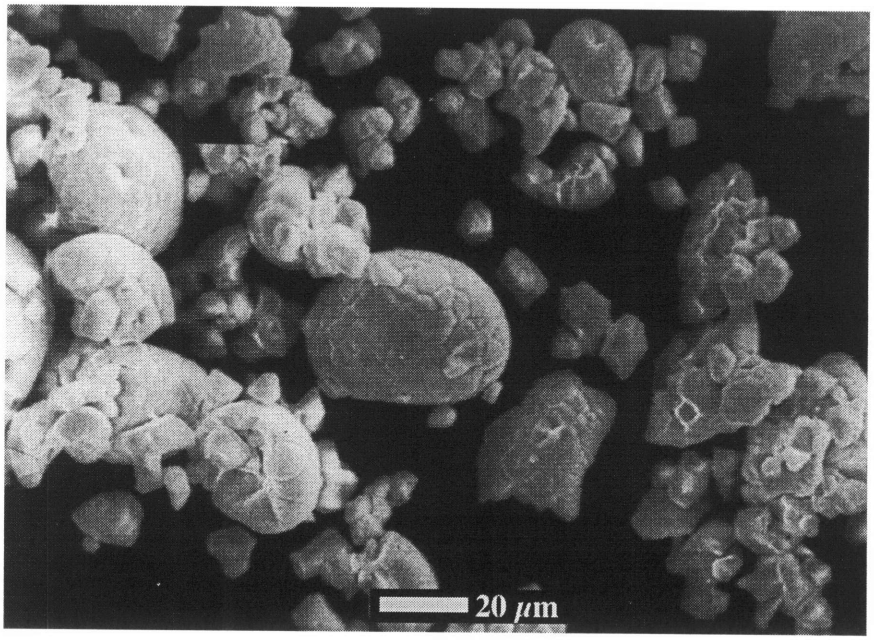

Figure 4.1.2. SEM micrograph (high magnification) of the ZrO_2 particles used in the composite. The large particle in the center reveals the 5-10 μm grains in the powder.

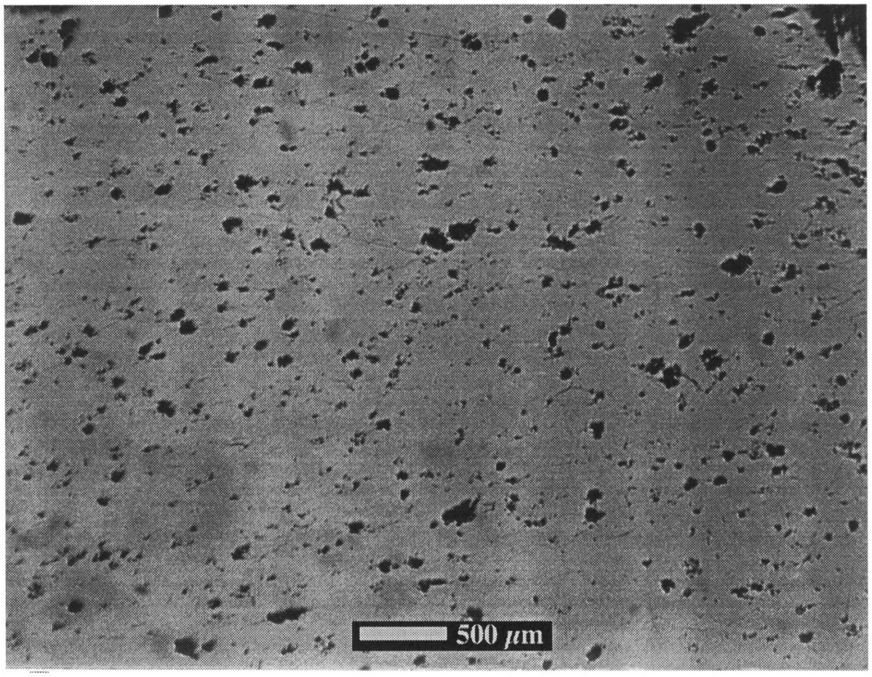

Figure 4.1.3. Optical micrograph of an as-received 10% composite sample. Shows size and distribution of the particulate phase.

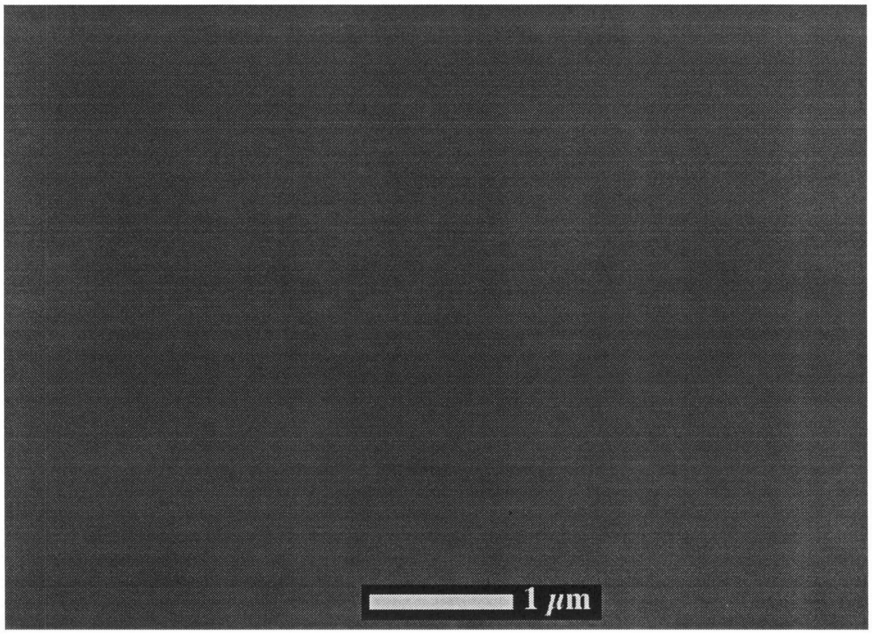

Figure 4.1.4. SEM micrograph of polished matrix PSZ in a 10% composite sample at high magnification. This illustrates the absence of pores in the matrix after hot pressing.

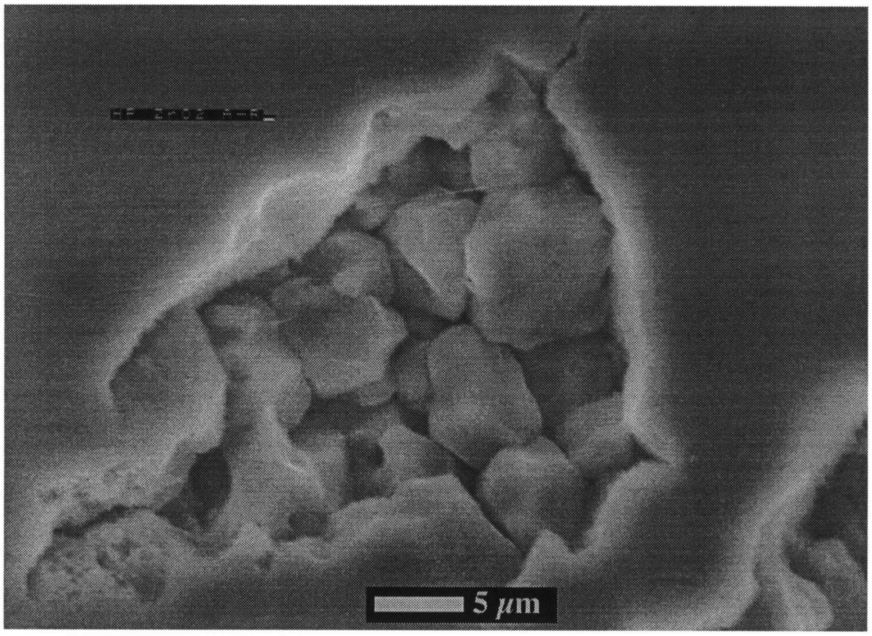

Figure 4.1.5. SEM micrograph of a sectioned particle in a polished 10% composite. The particle grains are unpolished and visible since they are in a cavity depressed from the level matrix surface.

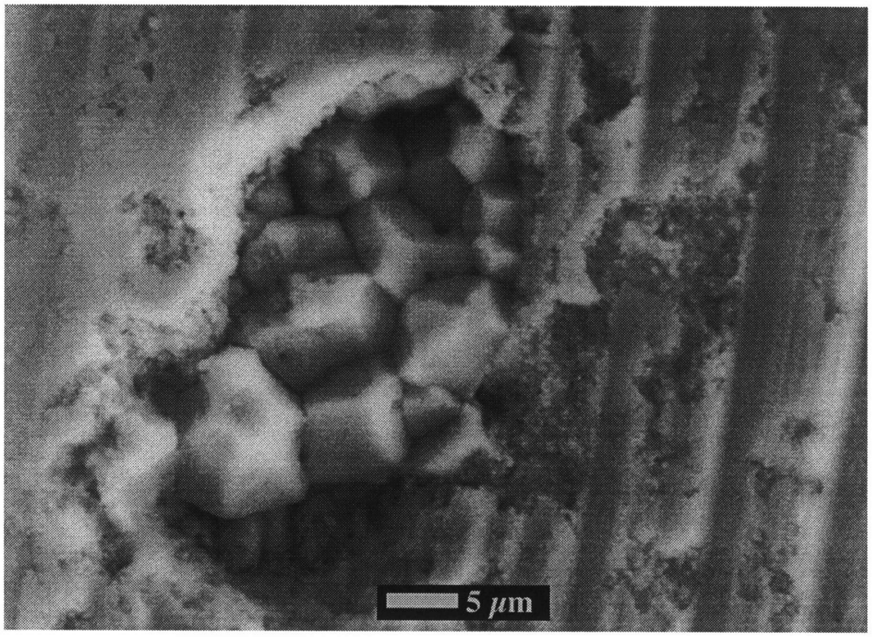

Figure 4.1.6. SEM micrograph of an unpolished, sectioned 10% composite surface. This illustrates particle fall-out during the sectioning process. The 0.2-0.3 μm PSZ matrix grains are also visible.

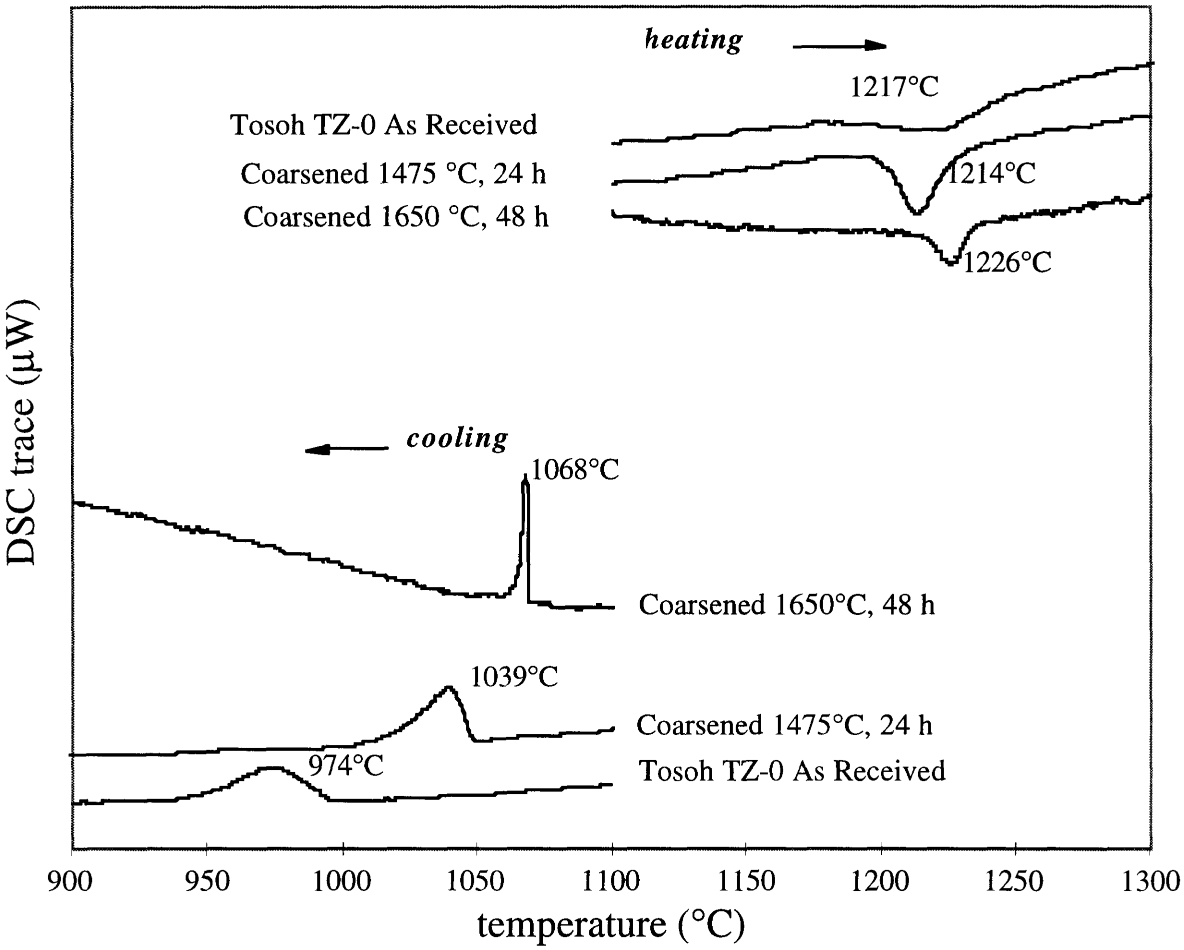

Figure 4.1.7. Differential scanning calorimetry results of ZrO_2 powders from coarsening pre-treatments. The coarsened 1650°C, 48 hour powder was used in the composite for creep and internal-stress plasticity testing.

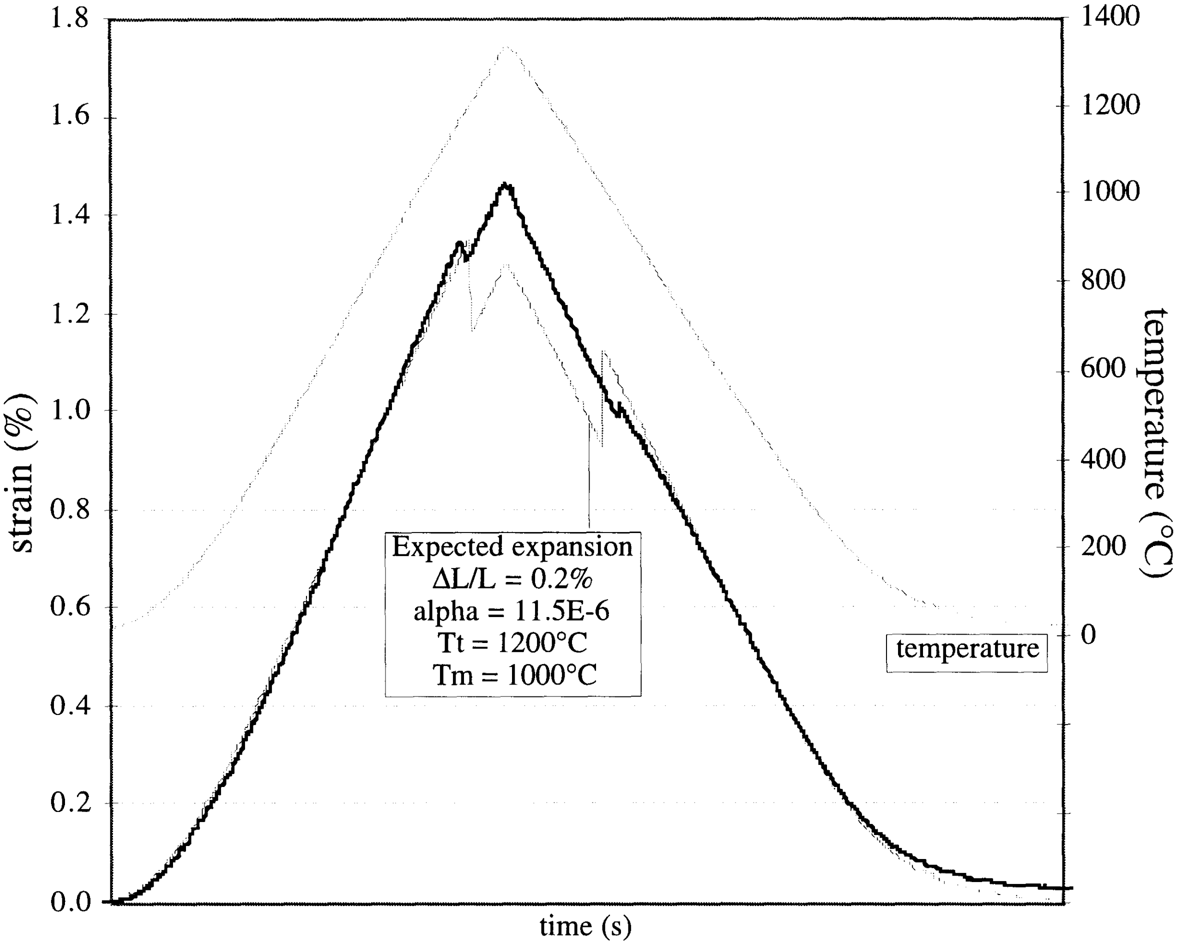

Figure 4.1.8. Complete dilatometry results for hot-pressed 10% composite, compared with a simplified expected curve. Sample length is 11.7 mm. Note suppression of transformation strain in the composite, and the small amount of ratcheting strain retained after the experiment.

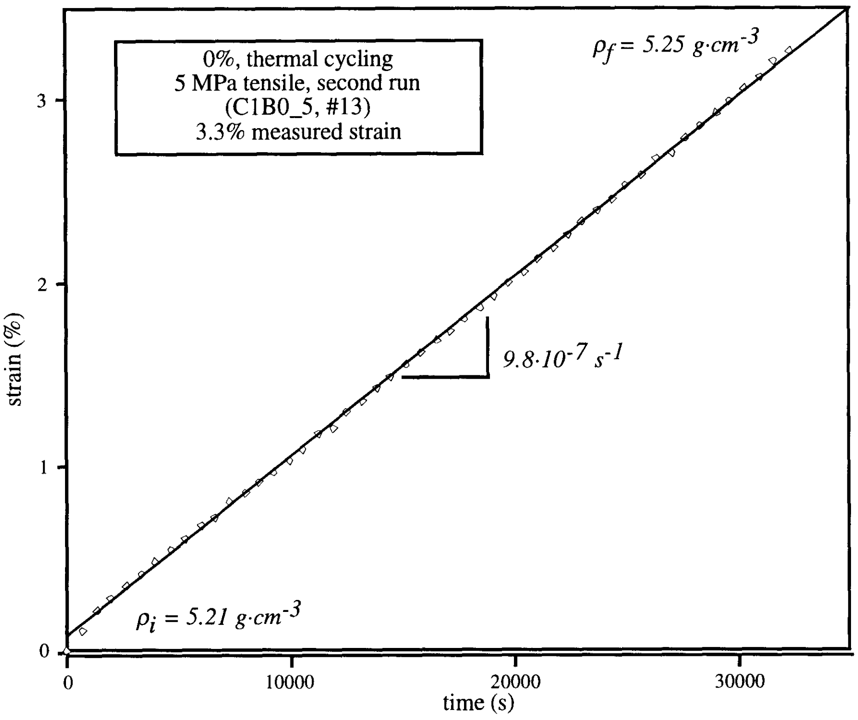

Figure 4.3.1. Corrected strain versus time for thermal cycling experiment on pure PSZ (0%) material at 5 MPa tensile stress, second run. This shows achievement of a steady-state strain rate. Note the low density measurement due to measurement of cracking in the heads.

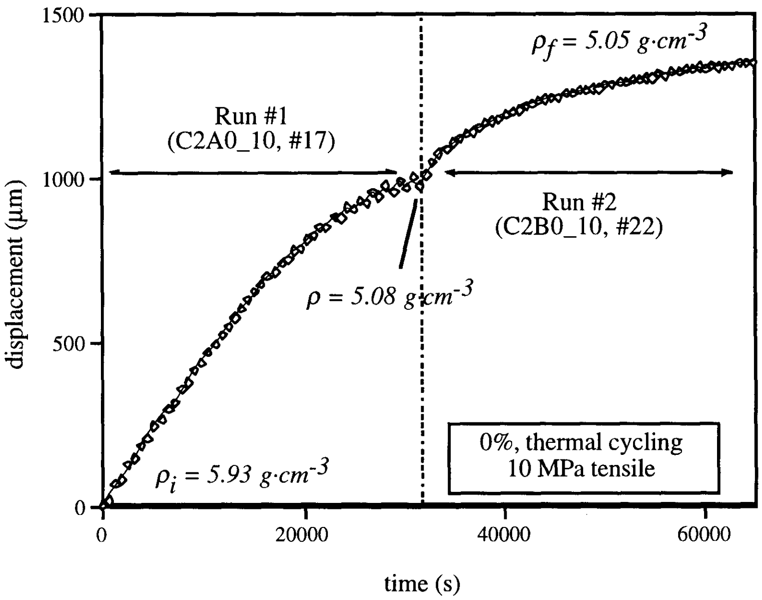

Figure 4.3.2. Displacement versus time for two successive 10 MPa thermal cycling tensile experiments on a sample of pure PSZ (0%). At this higher stress, more time is required to achieve steady-state creep.

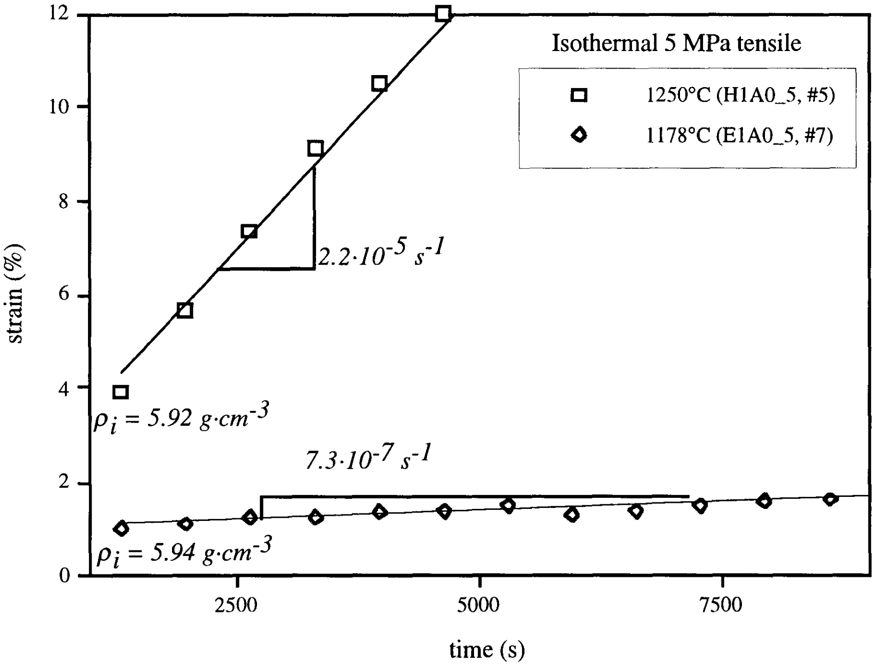

Figure 4.3.3. Primary, isothermal creep displacement of pure PSZ (0%) samples at 5 MPa, showing creep at 1250°C and 1178°C.

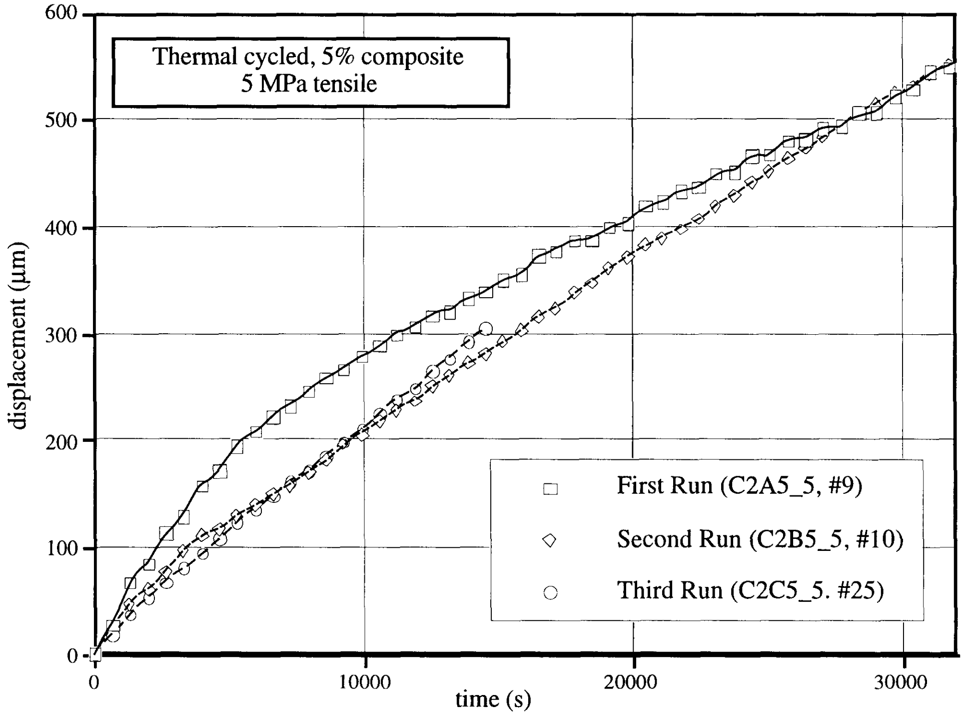

Figure 4.3.4. Transformation-mismatch plasticity during thermal cycling of 5% material at 5 MPa tensile stress through three successive runs until failure. This demonstrates the achievement of steady-state conditions during thermal cycling at low stress within the first run

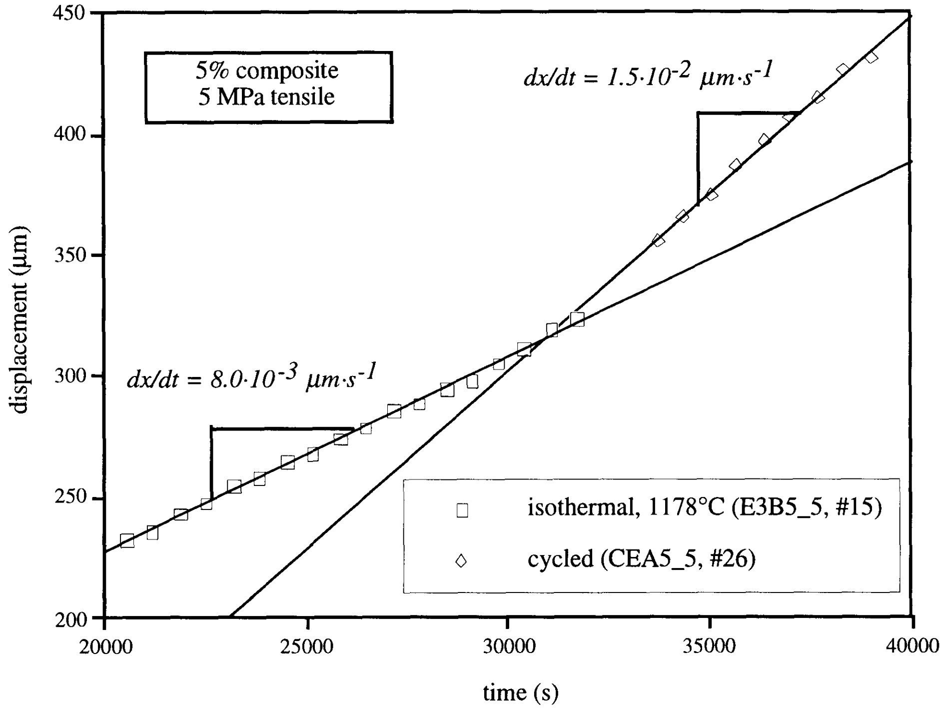

Figure 4.3.5. Deformation of a PSZ-5% ZrO_2 sample during thermal cycling after isothermal creep under 5 MPa tensile stress. Although strain could not be calculated, displacement rate approximately doubled.

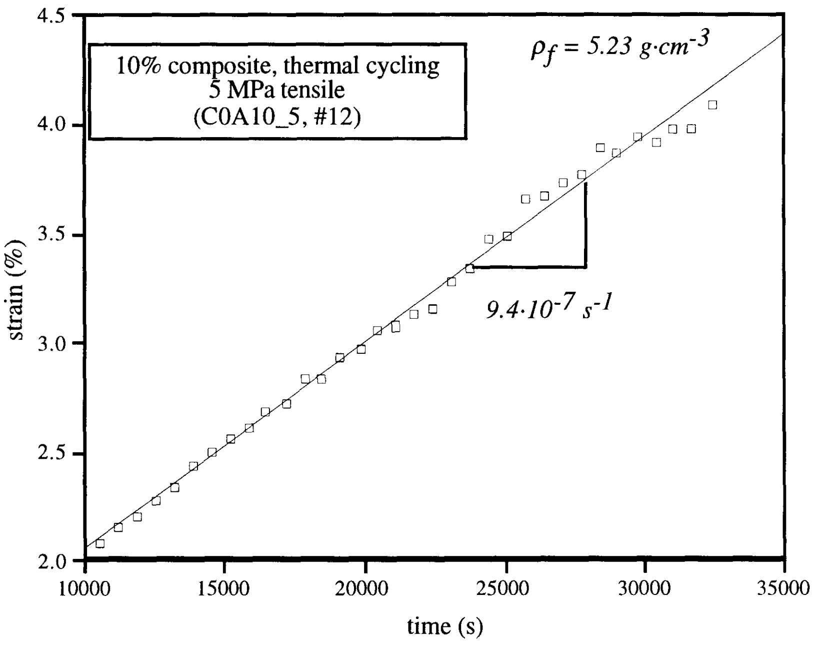

Figure 4.3.6. Transformation-mismatch plasticity during thermal cycling of a PSZ-10% ZrO_2 composite at 5 MPa tensile stress, second run. Again, a steady-state is maintained throughout the experiment.

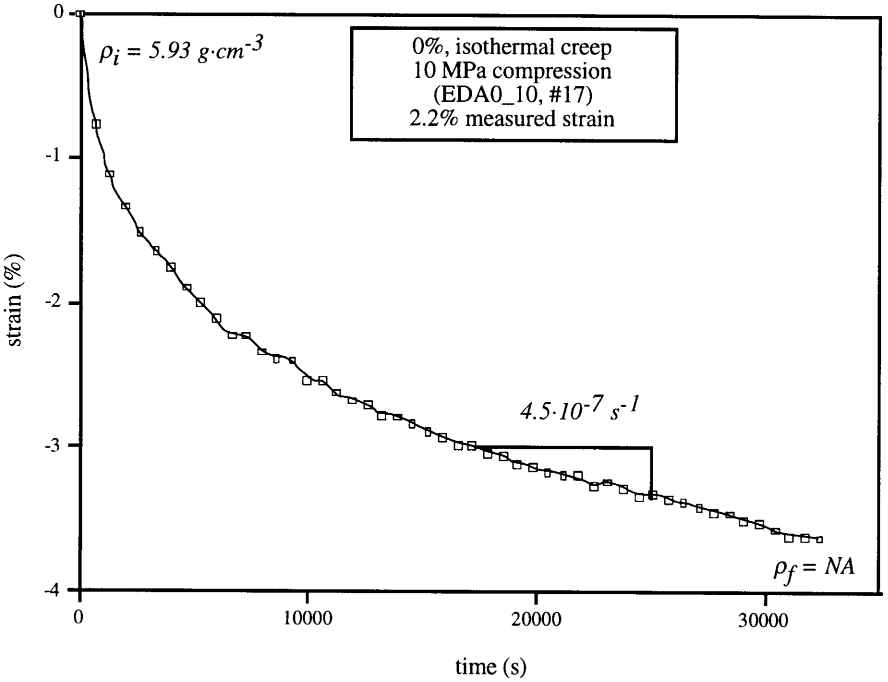

Figure 4.4.1. Isothermal (1178°C) creep of a sample of pure PSZ (0%) under 10 MPa compressive stress. Shows attainment of a 4.5·10^{-7} s^{-1} steady-state strain rate. Final density could not be measured due to excessive cracking.

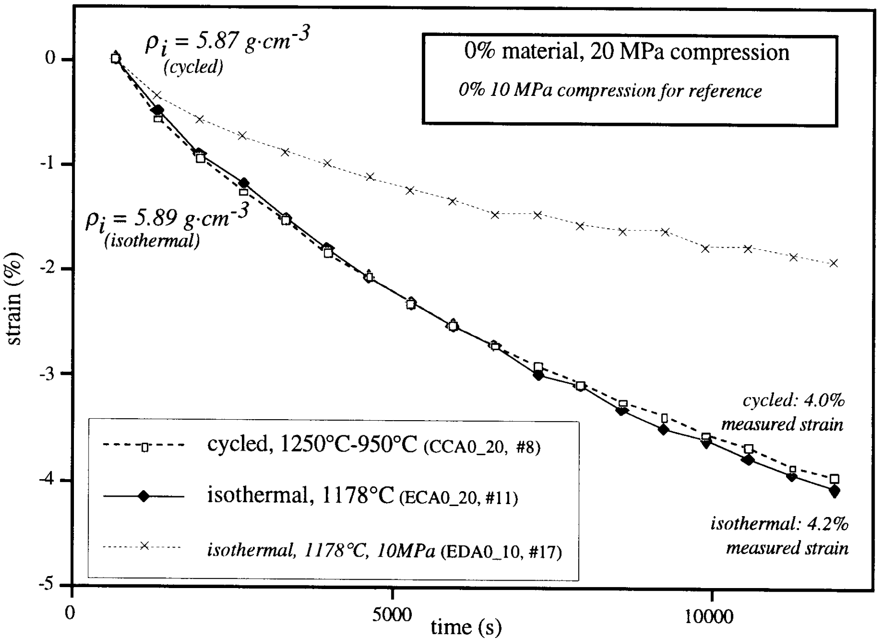

Figure 4.4.2. Comparison of 20 MPa compression experiments during isothermal (1178°C) and thermal cycling conditions on pure PSZ (0%). This shows the similar strain response of the two experiments.

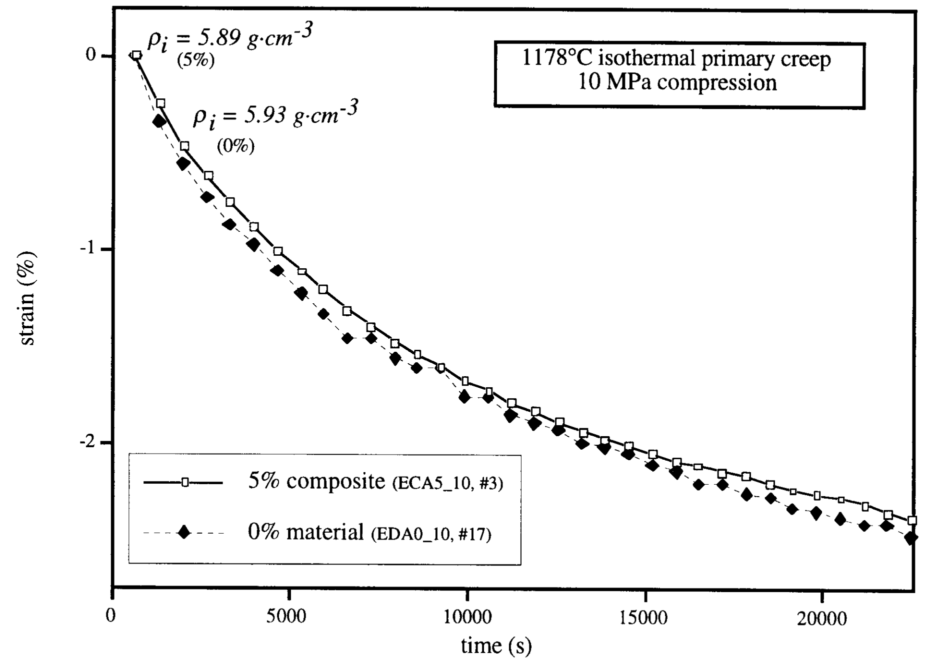

Figure 4.4.3. Primary creep behavior of pure PSZ (0%) and PSZ-5% ZrO_2 composites during isothermal (1178°C) compression creep at 10 MPa.

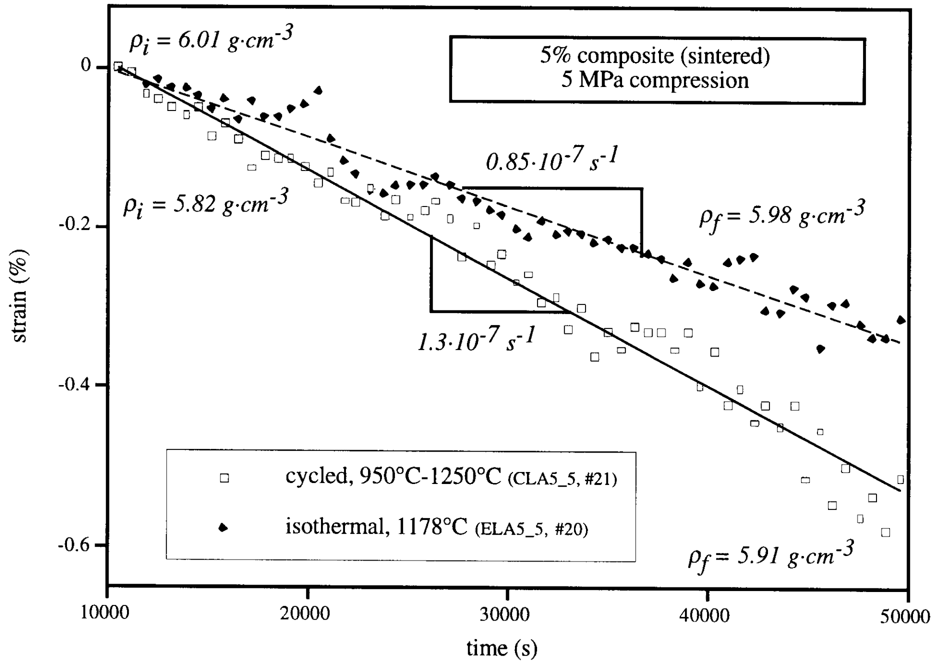

Figure 4.4.4. Comparison of 5 MPa compression experiments during thermal cycling and isothermal creep on a PSZ-5% ZrO_2 composite. Shows the faster steady-state strain during thermal cycling.

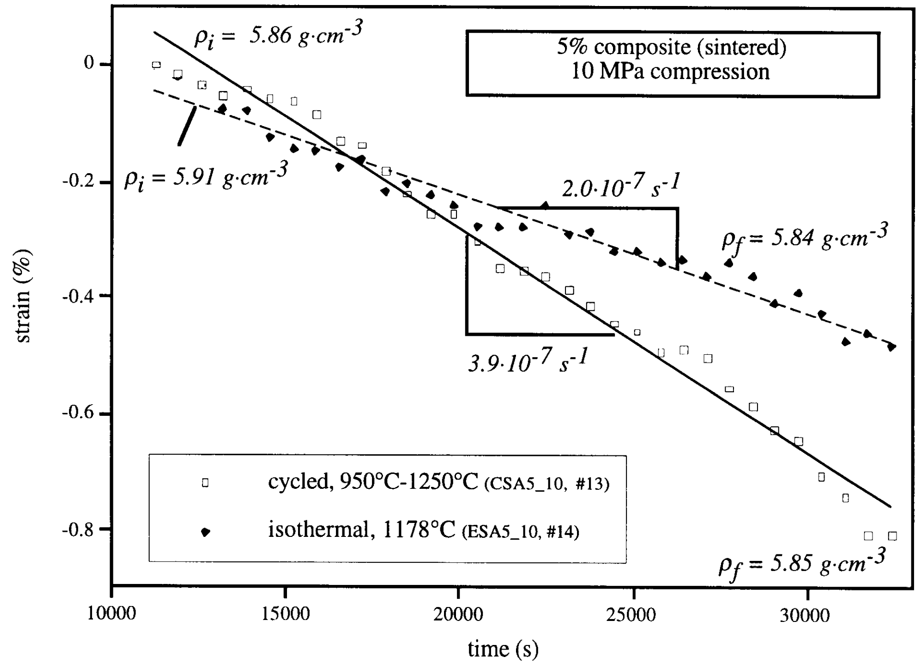

Figure 4.4.5. Comparison of 10 MPa compression experiments during thermal cycling and isothermal creep on a PSZ-5% ZrO_2 composite. Shows the faster steady-state strain during thermal cycling.

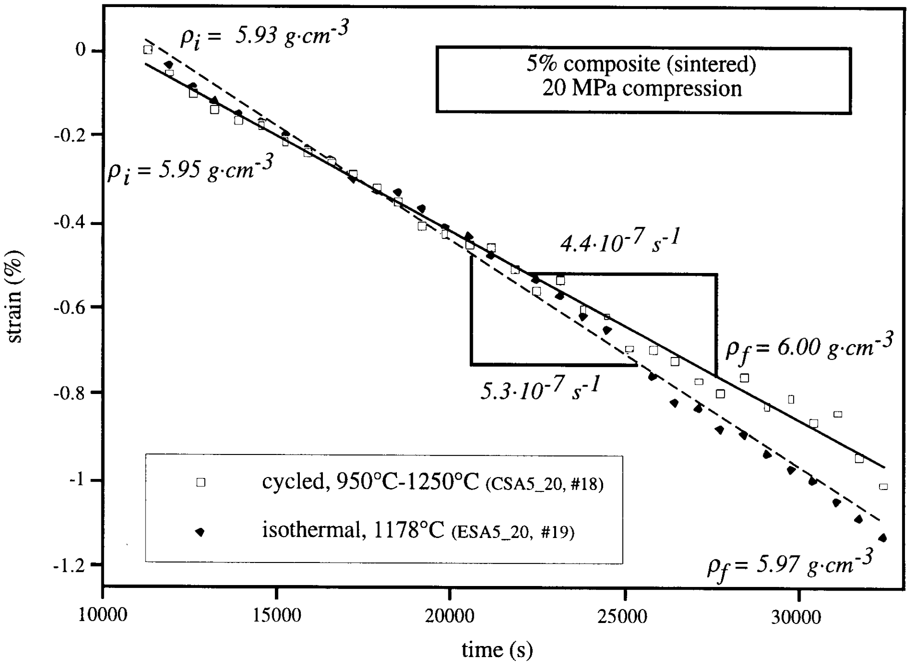

Figure 4.4.6. Comparison of 20 MPa compression experiments during thermal cycling and isothermal creep on a PSZ-5% ZrO_2 composite. Shows the faster steady-state strain during thermal cycling.

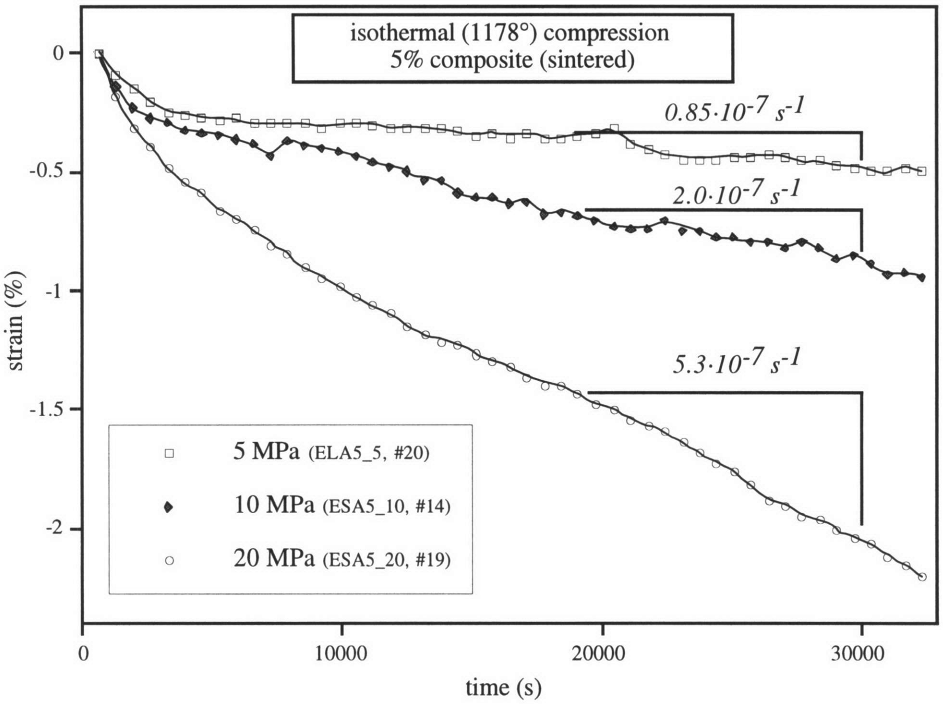

Figure 4.4.7. Deformation behavior of PSZ-5% ZrO_2 composites under various isothermal compressive stress experiments at 1178°C.

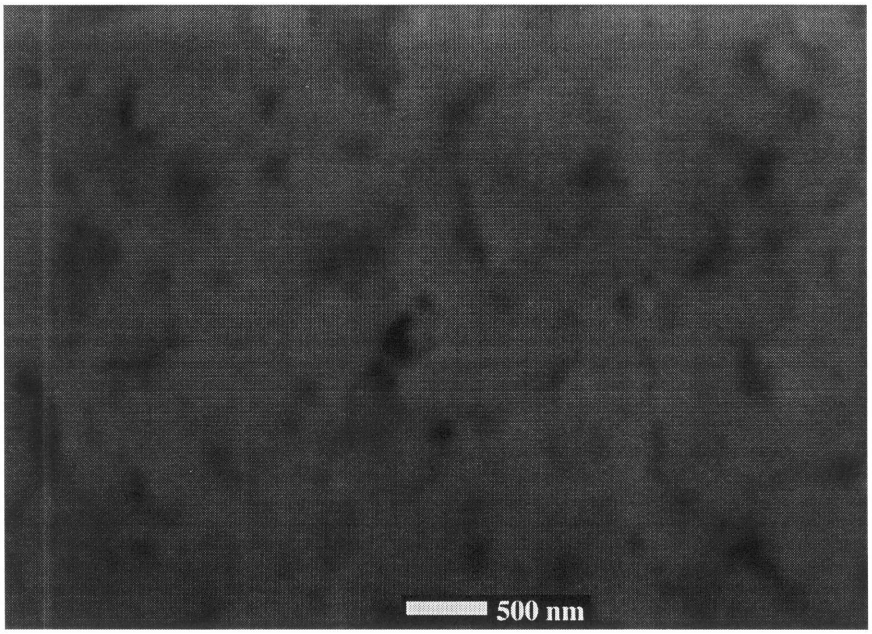

Figure 4.5.1. SEM micrograph at high magnification illustrating void (cavity) formation in a material pulled to 4.4% strain in tension during thermal cycling at 5 MPa. The sample density changed from 5.85 to 5.26 $g \cdot cm^{-3}$ during the experiment. Compare with figure 4.1.4.

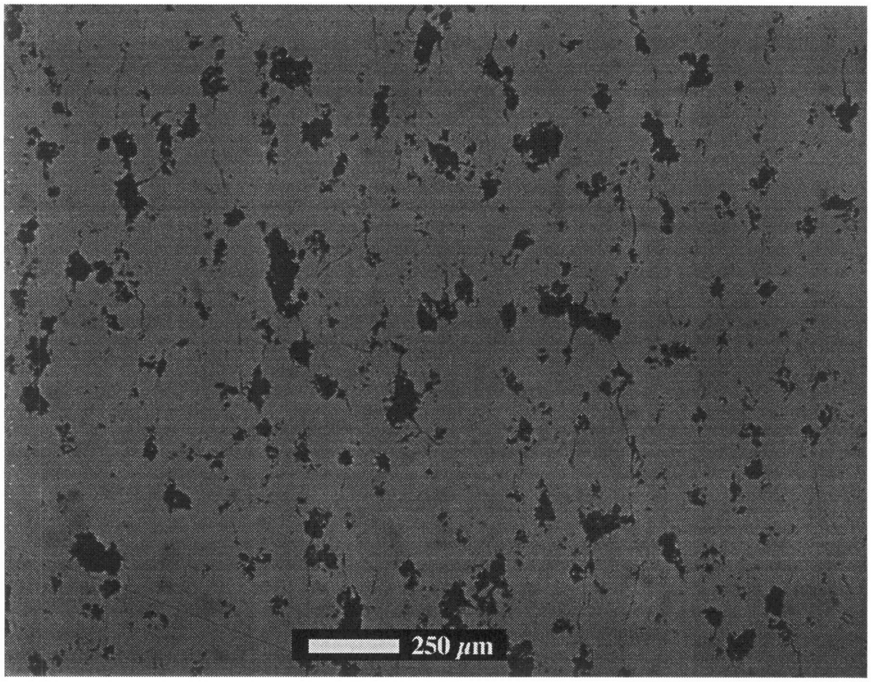

Figure 4.5.2. Optical micrograph of a polished PSZ-10% ZrO_2 composite after tensile strain to 4.4% during thermal cycling. Illustrates microcracking occurring in the matrix between particles.

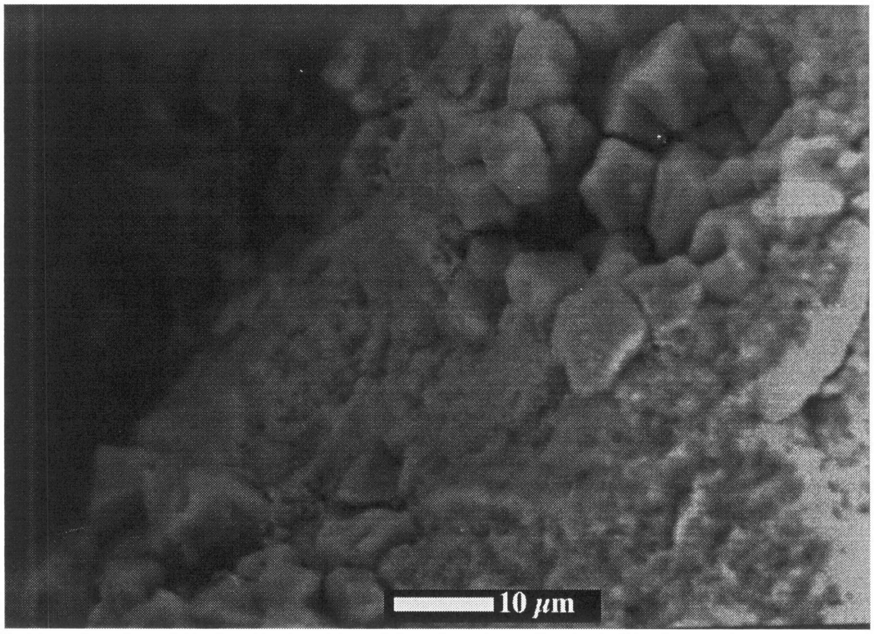

Figure 4.5.3. SEM micrograph of a fracture surface from a PSZ-10% ZrO_2 composite sample broken at high temperature and under 5 MPa tensile stress. Grain size of both the matrix PSZ and particle ZrO_2 can be observed.

5. DISCUSSION

5.1 RESULTS OF CREEP EXPERIMENTATION

To properly interpret the results of internal-stress plasticity during thermal cycling of PSZ-ZrO_2 composites, the creep behavior of the materials must be understood. Drawing from the results outlined in section 4, three important issues need to be addressed: (1) verification of the isothermal effective-temperature calculations, (2) calculation of the stress sensitivity during compression experiments performed on 5% composites, and (3) calculation of an activation energy for creep. These results may then be combined into a complete constitutive equation for 5% composite compression creep.

As was shown in figure 4.4.2, the creep response of pure PSZ samples during thermal cycling about 950-1250°C and during isothermal experiments was nearly identical, verifying the assumptions that were made during the calculation of the isothermal-effective temperature (1178°C). These calculations were made using an activation energy for creep of 580 $kJ \cdot mol^{-1}$, (given earlier), which is now considered to be the proper value for the operative mechanism involved with this low-temperature, low-stress creep. Figure 4.4.3 also presented the comparison of isothermal creep in pure PSZ and the 5% composite in compression, which confirms the above conclusion. There is, however, a very small difference in the strain rate between the two materials, which may be accounted for by the fact that the large particle grains may be serving as obstacles to a grain-boundary based diffusional flow process. The effect was expected to be minimal due to the low (5%) volume fraction of affected grains.

The value of the activation energy for creep may be verified by calculation from the results shown in figure 4.3.3, taking into consideration that the strain rates used are from the primary region which may involve a different activation mechanism; the result may thus not be reliable. Using the standard empirical form for fitting low-stress creep data in ceramics [11]:

$$\dot{\varepsilon} = \frac{A}{T}\sigma^n \exp\left(\frac{-Q}{RT}\right), \tag{15}$$

with the strain rates observed at 1523K and 1451K under 5 MPa yields a value of Q=580 $kJ \cdot mol^{-1}$, precisely confirming the average literature value used above.

Since the sintered 5% compression results yielded very reliable data (figure 4.4.4) without excessive complications in density or cracking, the results of isothermal creep under those conditions may be formed into a constitutive equation for creep. Again, using equation

(15), the three measured strain rates are fit to a power law with respect to stress, yielding an accurate n=1.32, shown in figure 5.1.1. Averaging the constant for the three equations gives the pre-exponential constant as $A=1.32\cdot10^8$ (for stress in Pa and strain rate in s^{-1}). In the full form, then, PSZ-5% ZrO_2 composites tested at temperatures about 1178°C and at stresses between 5-20 MPa will creep at steady state according to the following semi-empirical expression:

$$\dot{\varepsilon} = \frac{1.32\cdot 10^8}{T}\sigma^{1.32}\exp\left(\frac{-580{,}000}{RT}\right) \tag{16}$$

Notice that in these experiments the value of n=1.32 is slightly less than that typically observed in experiments on superplasticity in zirconia [11]; however, it is still in the range of observed stress sensitivities (1.0-2.6). In addition, the mechanisms responsible for superplasticity as described above with n=2 may not be active at temperatures of 950-1250°C, which are lower than those typically used in microstructural superplastic experiments; indeed the lower value of n most likely indicates that creep is controlled by lattice or grain boundary diffusion (n=1), not by grain boundary sliding.

5.2 *MODELS OF INTERNAL STRESSES*

To accurately interpret the effect of internal stresses during the thermal cycling creep experiments, a complete understanding of the nature of those stresses within the material must be achieved. Consider the case of a PSZ-ZrO_2 composite during cooling from high temperature in the absence of an externally applied stress. Assuming that the average internal stress in the matrix, σ_M, is zero at the onset of the transformation during cooling at 1000°C, the particles will expand into the matrix, creating an internal stress. Eshelby developed an analytical technique for the case of an ellipsoidal particle expanding (or contracting) to a different extent than the matrix surrounding it, as summarized in [19]. Eshelby presents a "cutting and welding" thought experiment to better understand the resultant stress and strain states of the particle and matrix, as shown in figure 5.2.1. In this schematic representation of one ZrO_2 particle (P) expanding in the PSZ matrix (M), the particle is "cut" out of the matrix, allowed to fully expand (1) by $\varepsilon=\varepsilon_T^0$, the transformation strain. Then the unconstrained, stress-free particle (assuming an isotropic transformation) is compressed to its original size, reinserted in the stress-free matrix, then allowed to expand to equilibrium size. This leaves the particle in an isostatic compressive state, while the matrix is in a complex state of stress which is tensile when averaged over the entire matrix. In this condition the particle is constrained, and the actual particle strain, ε_p, will be less than the transformation strain.

Eshelby formulated the S tensor (the Eshelby tensor) which expresses the relationship between the unconstrained transformation strain, ε_T^0 and the actual transformation strain, ε_T, achieved under matrix constraint. Development of this conceptual model to consider the effects of non-dilute systems (as is the case here) results in a series of equations for calculating the average stress and strain in the particle and matrix based on volume fraction, f, the transformation strain, ε_T, Young's modulus, E=110 GPa, and Poisson's ratio, υ=0.27. These data are listed in table 2.3.1 for ZrO_2 and PSZ. Incorporating not only the transformation strain but also the small amount of thermal mismatch strain between the two phases, this technique has been used to calculate mean internal stresses for the PSZ-5% ZrO_2 and PSZ-10% ZrO_2 composites in appendix 6. During heating, when the m→t transformation occurs, the stresses and strains developed will be exactly opposite those encountered during cooling (again assuming a zero stress state in the material before transformation). The results of those calculations are summarized in Table 5.2.2. The matrix constraint is evident in the $<\varepsilon_P>=-0.81\%$ compressive strain calculated in the particle (compared to the free state); in effect, the particle only achieves a transformation strain of $\varepsilon_T=\varepsilon_T^0+<\varepsilon_P>=1.19\%$.

	Matrix		Particle	
	$<\sigma_M>$	$<\varepsilon_M>$	$<\sigma_P>$	$<\varepsilon_P>$
PSZ-5% ZrO_2	108 MPa	0.045%	-2052 MPa	-0.86%
PSZ-10% ZrO_2	216 MPa	0.090%	-1943 MPa	-0.81%

Table 5.2.1. Results of Eshelby internal stress calculations for PSZ-5% ZrO_2 and PSZ-10% ZrO_2. Positive values are tensile while negative indicates compression.

The calculated mean stresses will be very important in the interpretation of the experimental results. However, the actual state of stress in the matrix is more complex. A very simple model may be created to better understand the state of stress in the matrix after the t→m transformation by examination of the stresses developed in an elemental volume of material adjacent to the transforming particle, as shown in figure 5.2.2. Considering the three directions in this spherically symmetrical model, it may be shown that the stress developed *radially* in the matrix, σ_r, is compressive, while the two tangential components, σ_θ and σ_ϕ, are tensile. An approximation of these stresses may be calculated by using the simple models shown in figure 5.2.3. Here a one-dimensional pipe of material in the composite of length L is considered between two particles. If it is assumed that L remains constant (the composite does not dilate) during the allotropic transformation and the particles expand by ε_T (1.19%), the uniaxial stress in the pipe will be

$$\sigma_r = 2E\frac{\varepsilon_T r}{L} \tag{17}$$

where E is the Young's modulus of the material (the same value is used here for the matrix PSZ and the particle ZrO_2). Using the relationship between the length and radius in terms of the volume fraction,

$$L = r\left(\frac{4\pi}{3f}\right)^{\frac{1}{3}}, \tag{18}$$

gives an expression for the radial stress independent of the length and radius used in the model:

$$\sigma_r = 2E\varepsilon_T\left(\frac{3f}{4\pi}\right)^{\frac{1}{3}}. \tag{19}$$

Inserting the proper values in equation (19) gives σ_r= -754 MPa for a 10% composite. In a similar fashion, figure 5.2.2b depicts a particle exhibiting a transformation strain of 1.19% to the new size (dotted line). If the interface is "unwrapped" and the circumferential strain is considered at the interface, we find the interface strain, $\varepsilon_\theta = \varepsilon_\phi = \varepsilon_T$. The tensile stress induced in the matrix directly adjacent to the particle will then be $\sigma_\theta = \sigma_\phi = E\varepsilon_T$, or +1309 MPa, independent of volume fraction. Note that this is a maximum stress, and the level will decay with distance from the particle. Despite the many assumptions in these calculations, the valuable result is the prediction of tensile stresses tangential to the particle and compressive stresses in the direction between particles. Note that again, the opposite case (during negative transformation during heating) will yield equal and opposite results. More precise solutions to this problem is given in [8] and [19]

Actual internal stresses encountered in composite samples during thermal cycling in the absence of external stresses may be calculated based on the results from dilatometry of a PSZ-10% ZrO_2 sample, presented in section 4.1. Figure 5.2.4 highlights an expanded region of the dilatometry data in which the transformation strain during the heating is 0.034% and during cooling is 0.027%. Comparing these results with the 0.090% mean matrix strain in

Table 5.2.1 for the 10% composite material indicates a discrepancy with the Eshelby theory. The lower measured bulk transformation strain may be attributed to the following five possible effects. (1) Internal matrix cracking under the large tensile stresses accompanying both the positive and negative transformations could be occurring. These cracks could open and close during transformation to absorb some of the strain which was expected to be measured externally. (2) Particle fragmentation, as observed during sectioning of the composites in Figure 4.1.6, could also indicate intergranular cleavage paths which could accommodate the strains of transformation. (3) Debonding of the particles from the matrix may occur. Strains could be taken up by these voids in the same way as the first two reasons. (4) Creep of the matrix may relaxing some of the internal stress which does not result in dilation. (5) There may be partial suppression of the phase transformation itself by stabilization from yttrium diffusion or stress constraints from the matrix. However, there is no broadening of the transformation temperature peaks in figure 5.2.4, which would be expected in (4) or (5). Microstructural observations in section 4 show evidence of both (1) and (2); however, the particle grains in figures 4.1.5 and 4.1.6, are presumed to be bonded directly to the matrix material at the "bottom" of the cavity, and they maintained a strong bond with the matrix through the rigors of mechanical polishing. In two subsequent dilatometry experiments on the same sample, the peak size and shape were maintained. Thus, regardless of the mechanism responsible for the reduction of the bulk transformation strain, this strain indicates the true level of transformation strain affecting the matrix, and has an impact on the true calculated internal stress that exists.

Taking the average value from dilatometry as the mean matrix strain, $<\varepsilon_m>=0.031\%$, the actual level of internal stress is calculated considering the bulk modulus:

$$\langle \sigma_M \rangle = \frac{E}{1-2\upsilon} \langle \varepsilon_M \rangle \tag{20}$$

This yields $<\sigma_M> = 74$ MPa for PSZ-10% ZrO_2 compared with $<\sigma_M> = 216$ MPa calculated with the Eshelby technique above. It is important to realize that the mean stress is the stress *difference* caused by transformation; this is different from the average stress, which is the actual stress level in the matrix. Thus the internal stress may or may not be zero, while the average stress increases or decreases by the amount of the internal stress when transformation occurs. Unfortunately, dilatometry was not performed on a 5% composite; however, the Eshelby results show that, in theory, mean matrix internal stress is directly proportional to volume fraction between 5-10%; thus the experimental level of internal stress in the 5% composites described below is taken as $<\sigma_M> = 37$ MPa, compared to the Eshelby value of $<\sigma_M> = 108$ MPa.

5.3 INTERNAL-STRESS PLASTICITY

The results from transformation-mismatch plasticity testing are again shown in figure 5.1.1 along with the isothermal creep experiments on PSZ-5% ZrO_2 materials, which were discussed in section 5.1 above. As was presented in section 4.4, the two thermal cycling experiments at 5 MPa and 10 MPa yielded strain rates which were significantly higher than those during isothermal creep. However, the 20 MPa thermal cycling experiment exhibited a strain rate *less* than that during isothermal creep. However, within experimental error, the strain rates at 20 MPa may be considered to be similar. There are several explanations for this result. First, if there was significant debonding or cracking in the sample, possibly due to the very high externally applied stress, no internal stresses would be generated, yielding the same creep rate as in the isothermal experiment. Second, there may have been variation of the particle volume fraction in the original sample billet, and this sample may have been cut from an area with very little pure ZrO_2 particles, again resulting in far less internal stress creation. Finally, if there were errors in the measurement of temperature, and the isothermal experiments were conducted even 10°C higher than indicated, the effective temperature would no longer be valid, and the thermally cycled 20 MPa experiment may indeed yield different results. Since there is no opportunity to repeat experiments or perform additional ones, analysis of these data will be accomplished by comparison with results from several successful models described in section 2. Models based on Greenwood and Johnson [13] (section 5.3.1), Sato and Kuribayashi [8] (section 5.3.2), and Wu, Wadsworth, and Sherby [7] (section 5.3.3) are compared with experimental results.

5.3.1 *Modeling based on Greenwood and Johnson*

In section 2.2.2 the results of a model for analysis by Greenwood and Johnson [13] was reviewed which was based on the yielding flow of the weaker of two phases during allotropic transformation of metals. Their model for materials at high homologous temperatures was modified using a modified Levy-Von Mises equation to describe the behavior of such pure allotropic materials in which the flow of the weaker phase will be rate-dependent. This expression was given in equation (7):

$$\Delta\varepsilon = \frac{4}{3}\frac{\Delta V}{V}\frac{5n}{4n+1}\frac{\sigma}{\sigma_i} \tag{21}$$

where σ_i is the internal stress and n is the stress exponent. This expression must be modified in three ways for application to this system. First, The PSZ-ZrO_2 composite may be considered to be a pure material which is transforming only partially, to the extent of the volume fraction of ZrO_2; thus the expression must be scaled by f. Second, although the model does not attribute transformation plasticity to internal stress, and indeed the strain per cycle is inversely proportional to the level of internal stress, the experimental internal stress, $<\sigma_M>$ is used in place of σ_i. Finally, a factor of 1/Δt, the time for a full thermal cycle is inserted to calculate an average strain rate comparable with the experimental variables. Also expressing ΔV/V as $3\varepsilon_T$, these modifications yield the following result:

$$\dot{\varepsilon} = \frac{1}{\Delta t}4f\varepsilon_T\frac{5n}{4n+1}\frac{\sigma}{\sigma_i} \tag{22}$$

Since this model does not consider creep outside of the transformation range, the isothermal creep strain rate has been added to the strain rate predicted by this equation in the results shown in figure 5.3.1. These data were calculated with n=1.32, $<\sigma_M>$=37 MPa, and f=0.05 in equation (22). Also included in this figure are results of the equation for internal stress of 216 MPa (the dashed line represents the semi-empirical creep curve for isothermal creep at 1178°C). The same results are plotted on a logarithmic plot in figure 5.3.2 to describe the behavior of this system at higher stresses. It is seen that an internal stress of 37 MPa predicts very large values for transformation-mismatch plasticity even at extremely low stress levels. In addition, the line representing the larger internal stress level unexpectedly indicates a decrease in the expected strain rate. While this model has been used successfully for modeling much of the experimental work in internal stress plasticity in metals (see [4]), it appears to be unsuitable for the case of a transforming-particle, non-yielding system which exhibits transformation plasticity due to the relaxation of internal stresses only.

5.3.2 Modeling based on Sato & Kuribayashi

The model of internal stress plasticity developed by Sato and Kuribayashi, discussed in section 2 and incorporating the diffusional flow of the particle in a composite has been used (see appendix 7) to create a model based on equation (30) in ref. [8]:

$$\dot{\varepsilon} = \frac{\sigma}{\Delta t_{1/2}}\left(\frac{\varepsilon'_T}{\Delta t_{1/2}}\right)^{1-1/n}\frac{\left(1-f^{1/n}\right)f}{\left(1-f\right)^2 f^{1/n}}\frac{2n(n+4)}{2^{1/n}5}\cdot\int_{\Delta t_{1/2}}\left[\frac{A}{T(t)}\exp\left(\frac{-Q}{RT(t)}\right)\right]^{1/n} dt \qquad (23)$$

Since the authors presented equation (23) in the form for a continuous thermal expansion mismatch, it has been modified here with ε'_T, the sum of the transformation strain and the mismatch strain, which is divided by the time for one half thermal cycle, $\Delta t_{1/2}$=660 s, to yield the average strain rate. The creep parameters in the integral were discussed above, but the temperature, T(t) has been considered as a function of time over the thermal cycle.

Using appropriate values for the PSZ-ZrO_2 system under investigation for several stresses yields the results seen in figure 5.3.3. Despite the concerns regarding some of the model's assumptions, a value of internal stress is not necessary for the calculation of the strain encountered during internal-stress plasticity. The predicted strain per cycle is dependent only on the mismatch strain, applied stress, stress exponent, volume fraction, and intrinsic creep properties (eq. 16), and again predicts a linear relationship between stress and strain, as shown in figure 5.3.4. The model appears to provide a more realistic prediction of the flow rate during internal-stress plasticity, but it still does suggest significantly higher strain rates than were measured. It is interesting to note, however, that the curve would be a reasonably good fit of the experimental data if the 20 MPa thermal cycling test were ignored.

5.3.3 *Modeling based on Wu et al.*

Perhaps the most effective method to predict these results of internal-stress plasticity is by a model based on the concept of Wu, Wadsworth, and Sherby [7], which was first discussed in section 2. This model is based on the simple concept that the average stress in half of the material in an externally stressed body with regions of non-isotropic, spherically symmetrical, constant internal stress will be enhanced by the mean stress while it will be reduced by the mean internal stress in the other half. Repeating equation (9) shown in section 2 here, we write

$$\dot{\varepsilon}_{tot} = \frac{1}{2}\left[\dot{\varepsilon}\left(\left|\sigma+\sigma_i\right|\right) + \frac{\left|\sigma-\sigma_i\right|}{\sigma-\sigma_i}\dot{\varepsilon}\left(\left|\sigma-\sigma_i\right|\right)\right]. \qquad (24)$$

As pointed out by Paterson [28], the enhancement and reduction of strain for the two "halves" of material will be the same magnitude in a material with Newtonian (n=1) flow; thus the effects of internal stresses in PSZ-ZrO_2 composites, with an intrinsic n=1.32, will be small. Although it was found that the expression may be expanded and simplified to yield a linear relationship of strain rate and stress, equation (24) has been used to calculate the results shown in figures 5.3.5 and 5.3.6 for modeling of the PSZ-ZrO_2 system. Although the strain rates predicted based on $<\sigma_M>=37$ are much higher than experimental values for 5 and 10 MPa tests, use of an internal stress value of 15-20 MPa provides a more accurate fit.

5.4 *FURTHER MODELING*

Despite the success of equation (24) in fitting the data, the true value of mean internal has not been resolved, since the calculated stress (37 MPa) based on dilatometry is too large to accurately predict the results based on the Wu et al. model in section 5.3.3. A probable explanation for this difference is that the model considers a constant level of internal stress, while, in fact, internal stresses generated by phase transformation decay at high temperature; it is proposed that this relaxation can account for the discrepancy in stresses by dilatometry and internal stress plasticity. A simple analysis of the extent of internal stress relaxation over a thermal cycle can give some additional insight to interpretation of the plasticity results.

Reviewing the results from dilatometry (figure 5.2.4), it may be considered that the 37 MPa internal stress calculated from the dilatational change during phase transformation is not actually a mean level of internal stress, but a *change* in the internal stress state, $\Delta<\sigma_m>$, which is -37 MPa at the m⟶t transformation and +37 MPa during the t⟶m transformation. Indeed, the measurement from dilatometry was calculated from a *difference* in the resultant data. If no creep relaxation occurred and the matrix was initially at zero stress, the m⟶t transformation would create -37 MPa and that value would be maintained over one half of the thermal cycle; the subsequent t⟶m transformation would reduce $<\sigma_m>$ back to zero for the other half cycle, resulting in 19 MPa time-averaged mean internal stress.

Internal stresses, however, do relax at high temperature, and the mean stress will actually vary with time. In addition, due to the allotropic transformation hysteresis and the shape of the thermal cycle used during these experiments, the temperatures over which the mean tensile and mean compressive stresses relax will vary substantially. A simple numerical model will be developed here in an effort to better understand how internal stresses evolve during thermal cycling with phase transformations, what the magnitude and signs of those stresses are, and the time scales over which they develop. The graphical results of this numerical model are shown in figure 5.4.1. It appears from this figure that mean matrix compressive stress created during heating will more rapidly decay, since the sample goes though the high temperature portion of the cycle (1200-1250-1000°C) before reversal of the internal stress. When the composite is cooling and a mean internal tensile stress is created, the tensile stress may only decay over the low temperature portion (1000-

950-1200°C) of the thermal cycle. (Averaging equation (16) with these temperature ranges to yield isothermal-effective values, it is found that $T_{hi=}1215$°C and $T_{low}=1160$°C, which would correspond to a creep rate 8.3 times faster at the higher temperature.) Beginning at t=0 with zero matrix mean stress, $\Delta\langle\sigma_M\rangle = -37$ MPa mean compressive stress is created by the m→t transformation. Relaxation of this stress over one half of a cycle (t=660 s) may be calculated with a creep relaxation equation,

$$\sigma(t) = \left[AE(n-1)t + \sigma_0^{\,1-n}\right]^{\frac{1}{1-n}} \tag{25}$$

In this simple model, the temperature profile has been divided into 20 second segments over which the temperature is averaged and assumed to be constant as used in equation (16). We find that the higher temperatures experienced during the first mean compressive cycle allow nearly all of the internal stress to be relaxed. Repeating this stress "jump and relax" model, it is shown that the mean tensile stresses created after the t→m transformation decay far less, decreasing in this first cycle from 35 MPa to 22 MPa. Iterating this process over a few cycles, it is found that a steady-state stress profile is developed over a thermal cycle, and the time-average of the mean stress in the matrix is tensile. In this steady-state profile, $\langle\sigma_M\rangle$ decays from 36 to 23 MPa while in tension in the low-temperature half-cycle. Then $\langle\sigma_M\rangle$ changes to -14 MPa and relaxes to -1 MPa through compression over the higher-temperature half cycle.

An average tensile mean internal stress does not, however, indicate external compressive stresses will be enhanced more than tensile stresses during transformation-mismatch plasticity, for several reasons. First, the mean internal stress is still a triaxial stress state of both tensile and compressive exponents. Thus, large compressive stresses are still "available" when the mean matrix stress is tensile. Second, the Wu model predicts that the internal stress is added to half of the material, and subtracted from the other half. Tensile forces may be pulling perpendicular to a uniaxial external compressive stress, having a positive effect on the overall strain rate. Finally, although stresses are large in tension, the stresses *are* relaxing slowly, and the high value of internal stress does not have much of an effect. To properly substantiate these claims, a true closed-form solution with tensor based stresses, or true 3-D finite element analysis would be necessary, which is beyond the scope of this analysis.

This model of time-variant internal stress may be easily applied to the model discussed in section 5.3.3 above which was based on Wu et al. Rather than applying a constant mean internal stress as was done in that section, the time-variant internal stress from figure 5.4.1 is used in the model, equation (24). While the internal stress profile above was calculated based on the absence of an external stress, it is considered a reasonable approximation. Figure 5.4.2 shows the results of this modification in the predicted strain rate versus stress compared with the expected isothermal creep based on equation (16) and results of the model for a constant 19 MPa internal stress. As is seen in the figure, incorporating the relaxation changes the effect only slightly. Compared with the model for a time-averaged, non-relaxing 19 MPa internal stress, the transformation-mismatch effect considering relaxation is decreased for low values and increased for high values of stress. This resultant model, based on relaxing internal stresses, is similar to what would be expected of a model based on Wu et al for an average internal stress of about 10 MPa. In effect, then, for this system which has stresses relaxing from a maximum mean 37 MPa, use of an average value of 10 MPa in models may yield more accurate results.

5.5 FIGURES AND ILLUSTRATIONS

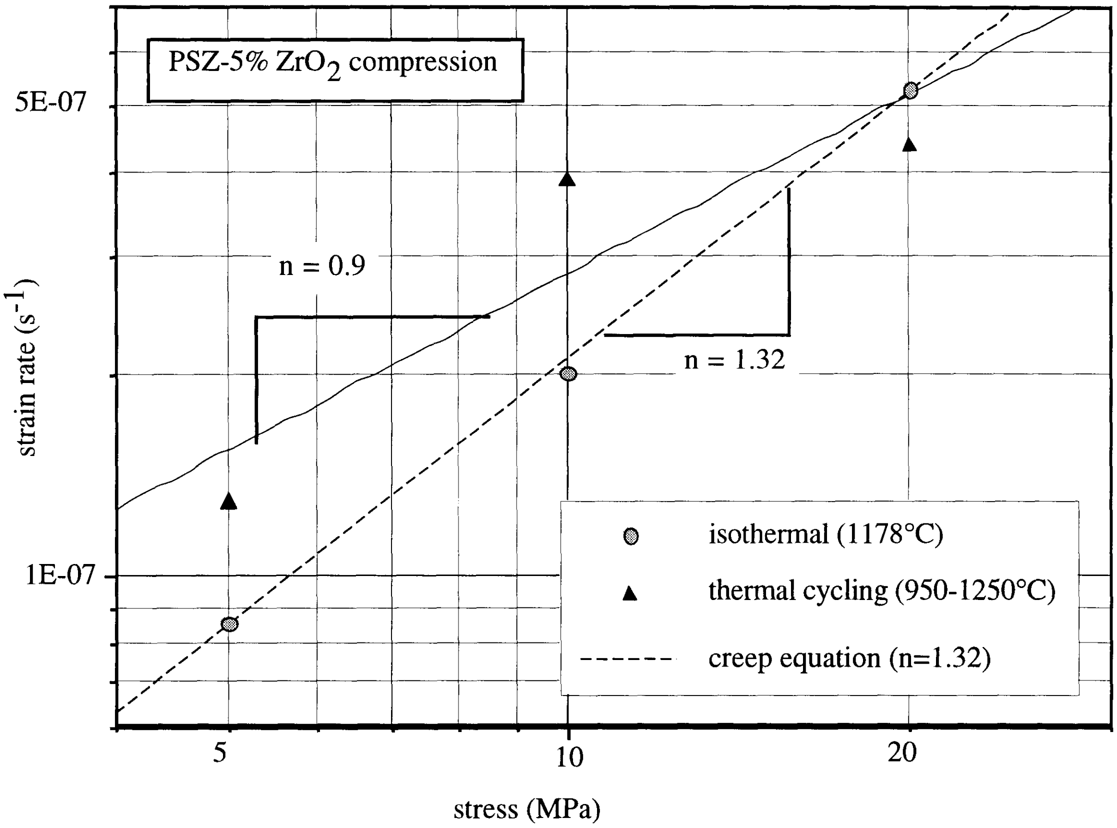

Figure 5.1.1. Steady-state strain rates of thermal cycling and isothermal (1178°C) compression creep experiments on high density PSZ-5% ZrO_2 composites.

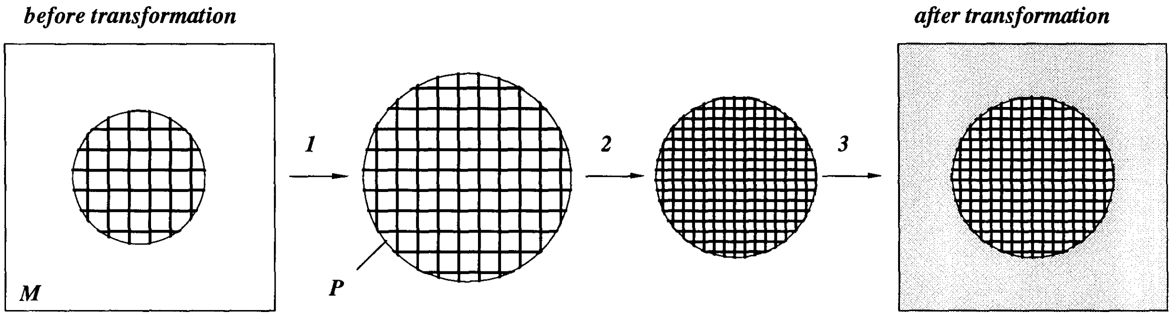

Figure 5.2.1. Eshelby's conceptual cutting and welding exercise to understand the states of stress and strain imposed by a transformation mismatch in a composite. "M", the matrix material is PSZ, while "P", the particle, is pure ZrO_2.

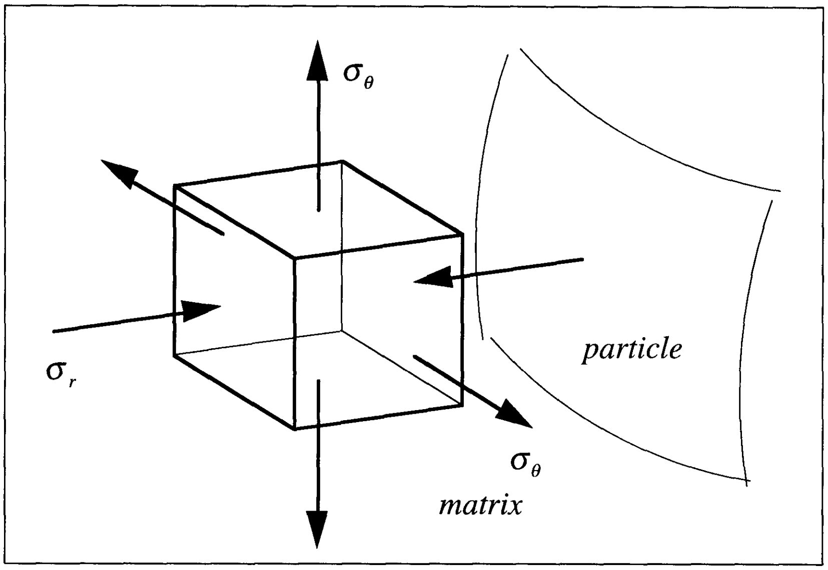

Figure 5.2.2. Schematic of the stresses created in the matrix adjacent to the particle due to allotropic transformation in the particle during cooling. The particle volume expands by a uniform positive ΔV/V.

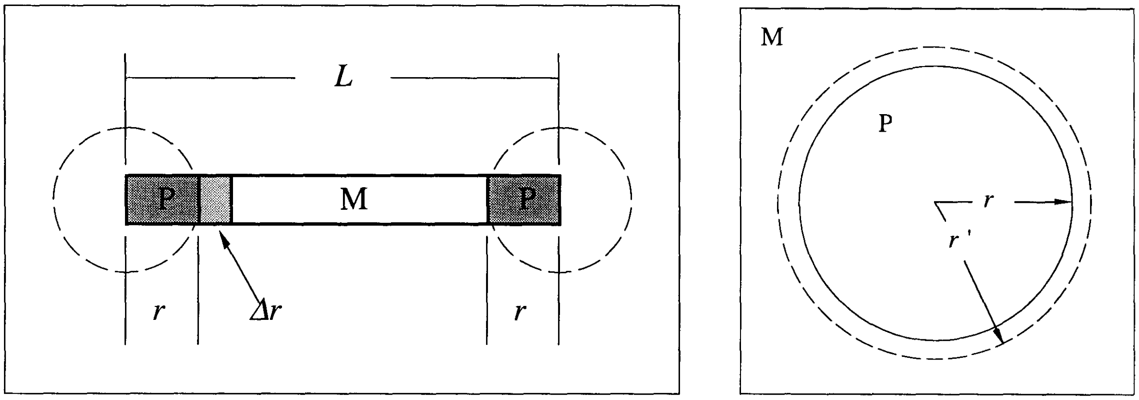

Figure 5.2.3. Simple conceptual models for estimating the sign and magnitude of matrix internal stresses during the particle transformation.

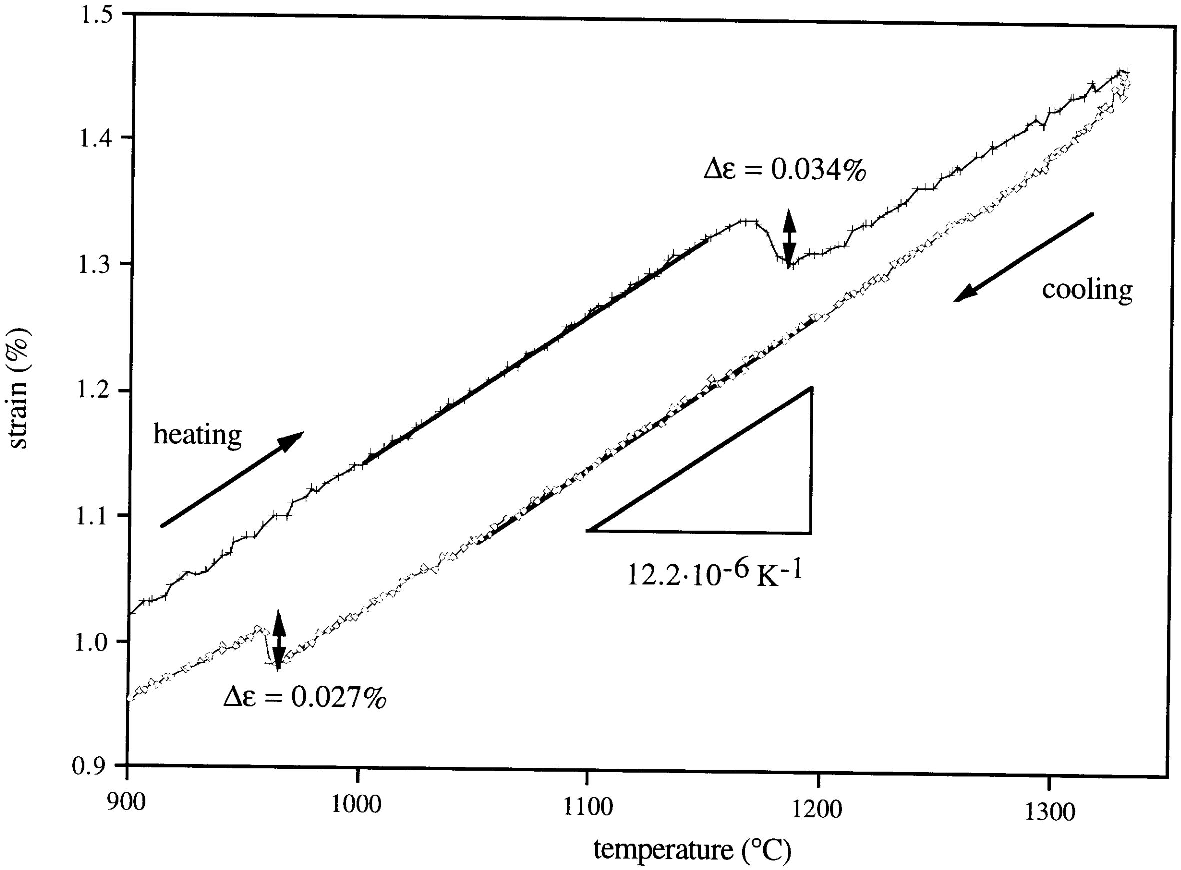

Figure 5.2.4. Highlights of dilatometry results with measurements of mean internal matrix strain changes, $<\varepsilon_M>$, and measured coefficient of thermal expansion.

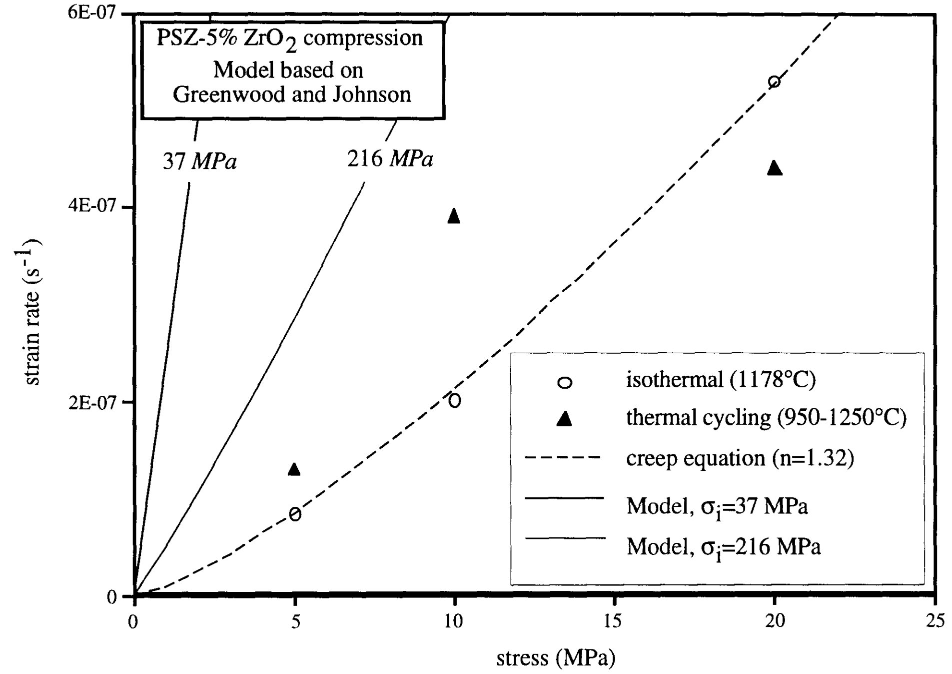

Figure 5.3.1. Linear results of compression experiments on PSZ-5% ZrO_2 composites at 5 MPa fitted with a model based on Greenwood and Johnson.

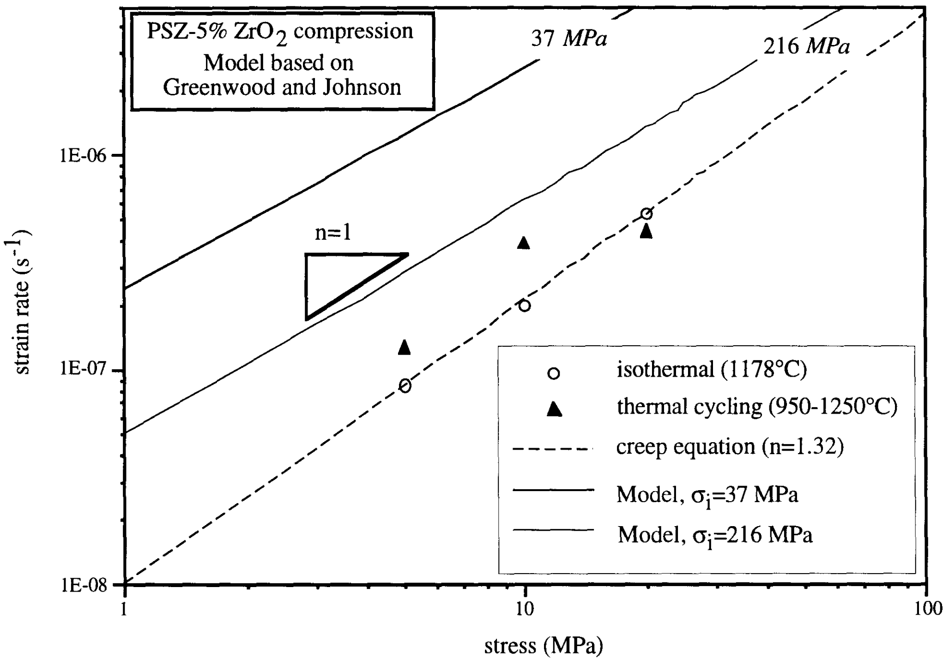

Figure 5.3.2. Logarithmic results of compression experiments on PSZ-5% ZrO_2 composites at 5 MPa fitted with a model based on Greenwood and Johnson.

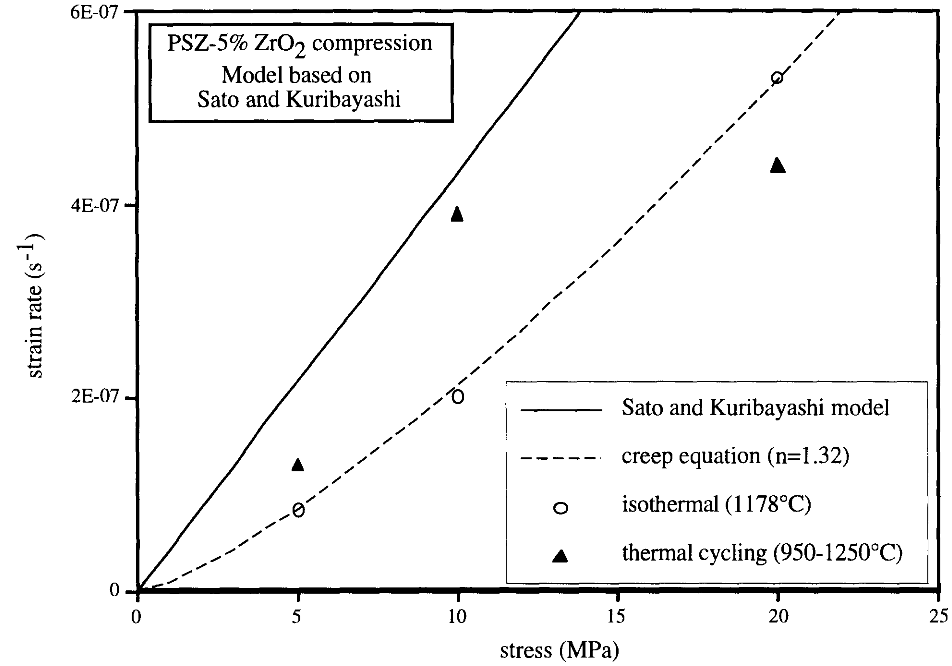

Figure 5.3.3. Linear results of compression experiments on PSZ-5% ZrO_2 composites at 5 MPa fitted with a model based on Sato and Kuribayashi.

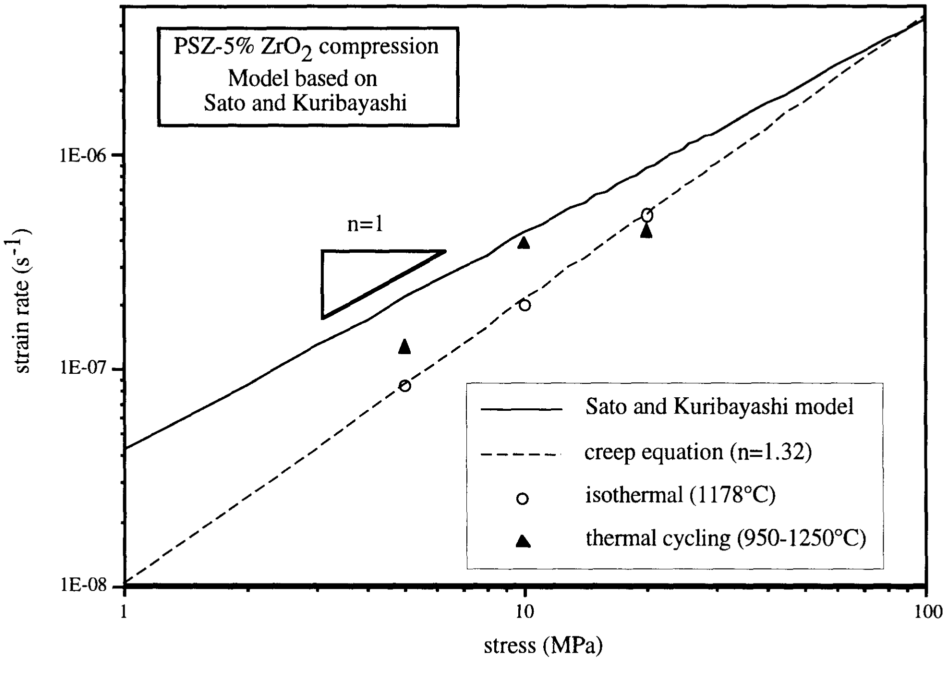

Figure 5.3.4. Logarithmic results of compression experiments on PSZ-5% ZrO_2 composites at 5 MPa fitted with a model based on Sato and Kuribayashi.

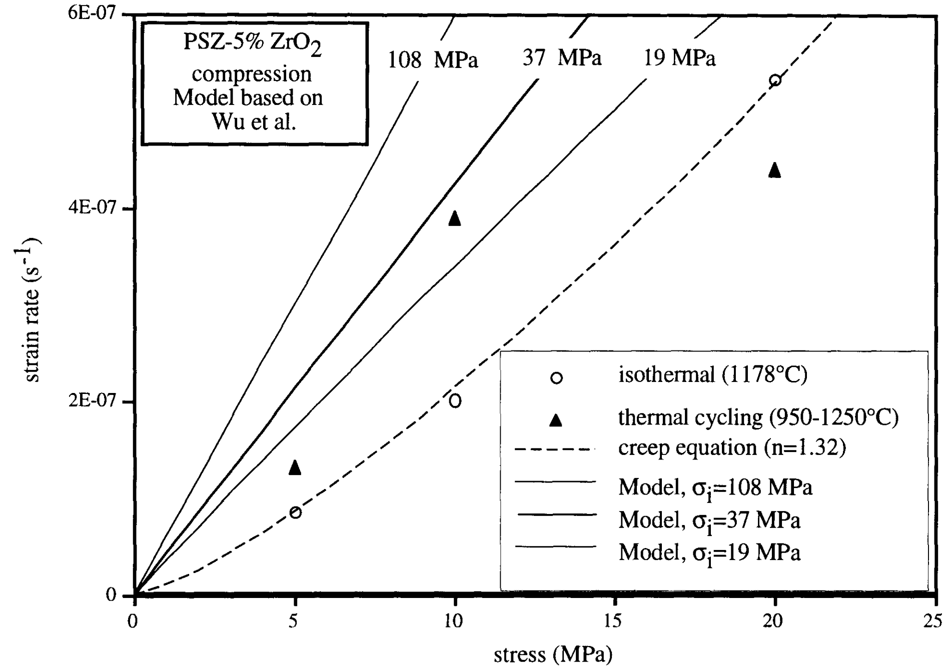

Figure 5.3.5. Linear results of compression experiments on PSZ-5% ZrO_2 composites at 5 MPa fitted with a model based on Wu, Wadsworth, and Sherby.

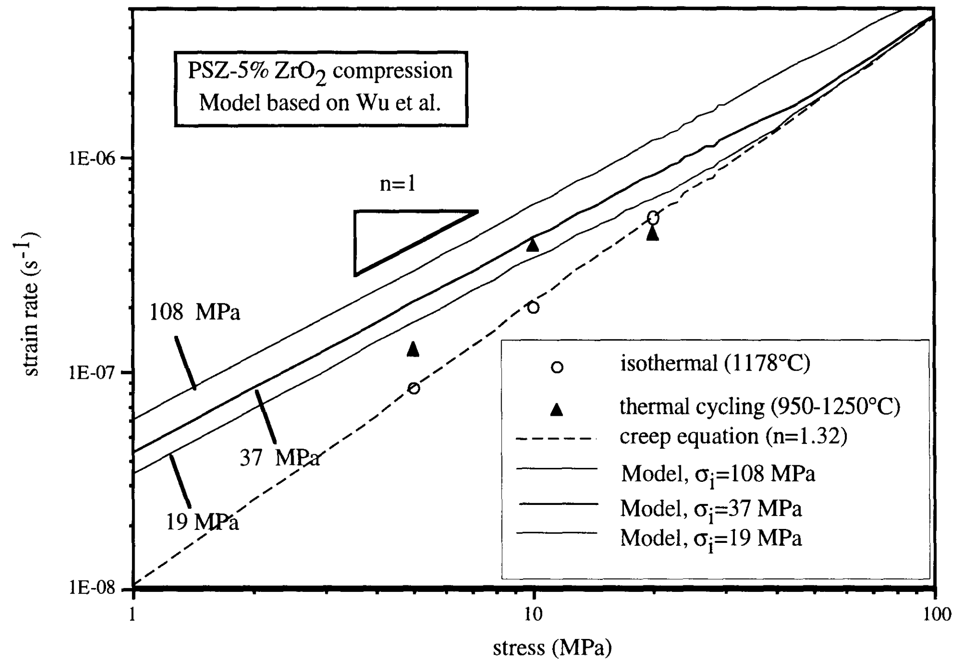

Figure 5.3.6. Logarithmic results of compression experiments on PSZ-5% ZrO_2 composites at 5 MPa fitted with a model based on Wu, Wadsworth, and Sherby.

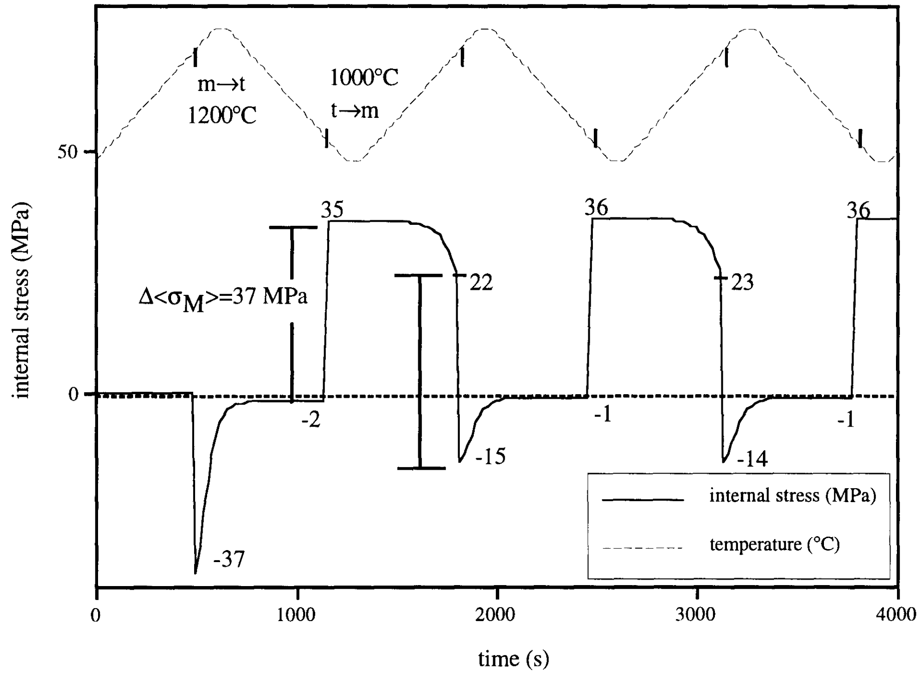

Figure 5.4.1. Plot of expected internal stress relaxation over several transformation thermal cycles. The initial matrix stress was set to zero.

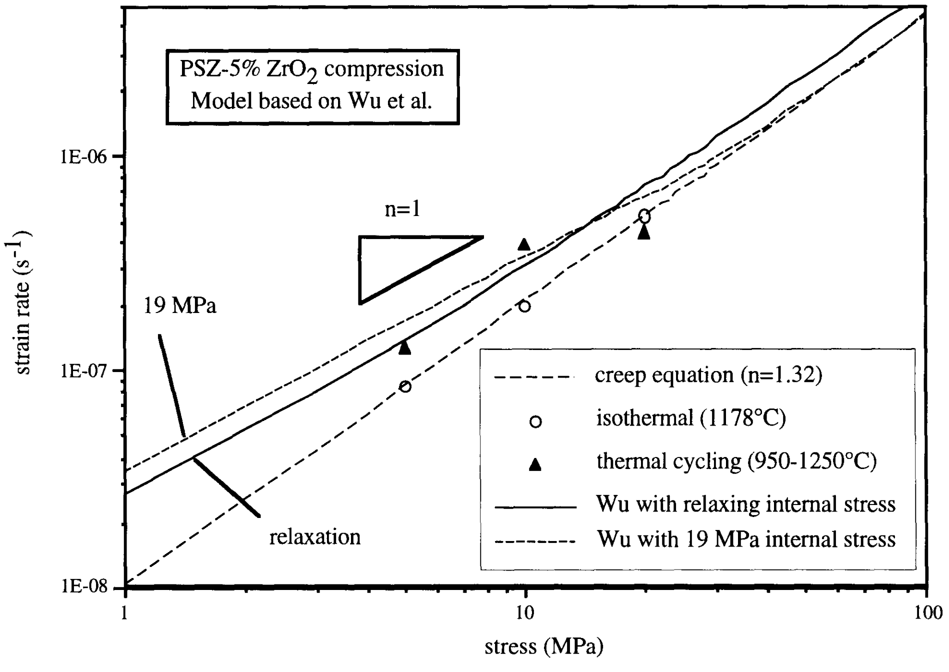

Figure 5.4.2. Results of compression experiments compared with Wu model incorporating relaxation of internal stresses from Figure 5.4.1.

6. CONCLUSIONS

(1) Internal stresses were created in a controlled, repeatable manner by transformation mismatch between allotropic zirconia particles and a non-transforming partially stabilized zirconia (PSZ) matrix. These stresses were calculated from dilatometry experiments to be approximately 37 MPa for a PSZ-5% ZrO_2 (by volume), or approximately one third the amount predicted by the Eshelby technique [19]. Microstructural evidence of particle fragmentation has been found which accounts for the lower stress value.

(2) Transformation plasticity has been demonstrated for the first time in a ceramic composite. PSZ-5% ZrO_2 deforms under 5 and 10 MPa stress more rapidly when internal stresses were created by thermal cycling about the allotropic transformation of ZrO_2, compared to equivalent isothermal experiments for which no internal transformation stresses were generated.

(3) Reproducible and cumulative enhancement of plastic strains due to transformation mismatch stresses has been observed for the first time in zirconia. Previous bending and compression experiments of bulk transforming zirconia [15] showed transformation plasticity, but these conditions destroyed the samples in doing so, preventing repetition of the effect.

(4) The results from transformation-mismatch plasticity experiments have been compared to three existing models, by Greenwood and Johnson [13], Sato and Kuribayashi [8], and Wu, Wadsworth, and Sherby [7]. The first model does not apply as well to this material system as it does to many metal-based systems investigated in the past. The second model yielded realistic predictions slightly higher than predicted experimentally. The third model gave comparable results to experimental values when the experimentally determined level of internal stress (smaller than theoretically calculated) was used as a parameter.

(5) Relaxation of internal stresses by creep has been shown to diminish the expected effect of internal-stress plasticity based on the latter model. A time-based numerical model for these effects was created for this system.

(6) This work has developed the fundamental knowledge necessary for a complete demonstration of transformation-mismatch superplasticity to large tensile strains in a ceramic composite with allotropic zirconia particles.

7. SUGGESTIONS FOR FUTURE WORK

Although transformation-mismatch plasticity has been demonstrated, more compression experiments would need to be performed to accurately describe the effect of internal stresses on the strain of these materials under internal stress. Experiments need to be repeated at 5, 10, and 20 MPa, and more tests must be performed at lower and higher stresses (as well as stresses in between these values) to describe the effect as a function of externally applied stress. This work merely demonstrates the phenomenon and compares those results with model predictions.

Following are several suggestions for future work which would allow transformation-mismatch plasticity to be demonstrated in tension and to large strains to create true internal stress superplasticity in partially stabilized zirconia. Two fundamental situations created by the intrinsic properties of zirconia caused the magnitude of the effect measured in this study to be so small that they were difficult to measure experimentally, and were overshadowed by other effects, including density changes and cracking. In addition, one materials design suggestion for enhancing internal stress in composites with transforming particles will be given.

First, the homologous temperature at which experiments were performed was relatively low (0.4 - 0.5 T_m), leading to small strain rates and brittleness of the matrix. There are two solutions to this problem which could be pursued: (1) Increase the testing temperature to increase creep rates of the matrix material. Since the testing temperatures are fixed by the phase transformation temperature, this can be achieved by alloying hafnia (HfO_2) and zirconia to increase the phase transformation temperature [29], [33]. However, testing at higher temperatures may lead to stabilization of the particles by yttrium diffusion from the matrix. (2) Remain at the allotropic zirconia temperatures and decrease the creep strength of the matrix. This has been achieved by additions of Fe_2O_3 [1], CuO [1], and SiO_2 [41] to PSZ. Unfortunately, additives may also adversely affect the room temperature properties of PSZ.

Second, the intrinsic stress sensitivity was quite low (n=1.32) at the experimental temperatures, which also diminished the potential effect of internal-stress plasticity in this material. Ideally, a material which deforms by yield would be best suited; for TSP of non-yielding zirconia, however, it has been observed that the stress sensitivity at slightly higher temperatures (1400-1500°C) is about 2-3 (see [11]). Thus, alloying of the zirconia particles with hafnia appears to be the best of the two solutions presented above.

Finally, there is one modification which could be made to the microstructure of the composite which could optimize the level of internal stress and thus increase TSP. It was observed that the internal stress calculated from dilatometry was one third that predicted by the Eshelby technique, and it is supposed that this decrease is caused by fracturing of the particles during the intense hydrostatic tensile forces that the particle encounters during the m→t phase transformation. The use of single-crystal particles rather than polycrystalline particles would rectify that problem since cracking of particles typically occurs at the grain boundaries. This can be achieved by crushing the coarsened particles until their size is similar to the grain size. Another advantage is that smaller particles would also create smaller maximum local stresses around the particle, reducing the chances of microcracking in the matrix. The use of small particles may, however, be limited by the diffusion of yttrium from the matrix into the particles, stabilizing the material and preventing internal stress generation.

APPENDIX 1. ENGINEERING DRAWING OF TENSION PULLRODS

(All dimensions are in inches)

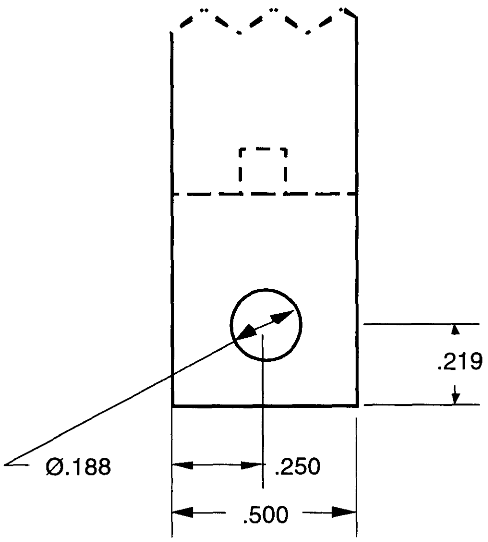

Note: Upper hole to receive a 4.0 mm pin (0.157") or a 5/32 inch (0.156") pin. Slot to receive tensile sample 3.0 mm (0.118") thick.

Note: Platform inserts to be fitted into slot and hole (see separate drawing). Please ensure proper fit.

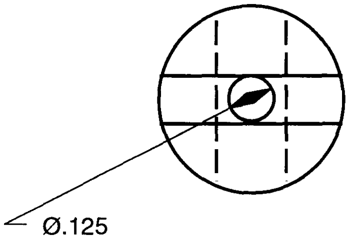

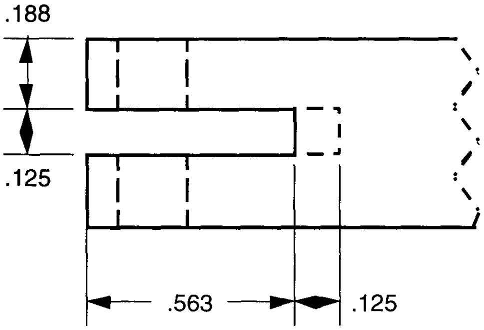

APPENDIX 2. ISOTHERMAL EFFECTIVE TEMPERATURE CALCULATION

If a sample is being deformed under a temperature profile (cycle) which varies with time, T(t), then the instantaneous strain rate, $\dot{\varepsilon}_{cyc}(t)$, also varies with time by equation (15). If a certain time interval Δt is considered, a total strain of $\Delta\varepsilon_{cyc}$ will be accumulated on the sample by

$$\Delta\varepsilon_{cyc} = \int_{t=0}^{\Delta t} \frac{A}{T(t)} \sigma^n \exp\left(\frac{-Q}{R \cdot T(t)}\right) dt. \tag{1}$$

There also exists an isothermal temperature (or effective temperature, T_{eff}) which would cause the same amount of strain $\Delta\varepsilon_{Teff}$ under the same level of stress as during the thermal profile:

$$\Delta\varepsilon_{Teff} = \Delta t \cdot \frac{1}{T_{eff}} \exp\left(\frac{-Q}{R \cdot T_{eff}}\right) \tag{2}$$

Equating these expression and canceling the constant coefficient A and the stress, yields the following:

$$\Delta t \cdot \frac{1}{T_{eff}} \exp\left(\frac{-Q}{R \cdot T_{eff}}\right) = \int_{t=0}^{\Delta t} \frac{1}{T(t)} \exp\left(\frac{-Q}{R \cdot T(t)}\right) dt \tag{3}$$

Considering constant heating and cooling rates over a cyclical profile from $T(t=0) = T_1$ to $T(t=\Delta t) = T_2$, T(t) for one half of the thermal cycle may be written as

$$T(t) = T_1 + \frac{T_2 - T_1}{\Delta t} t. \tag{4}$$

If the limits of integration in (3) are put in terms of T by (4), this gives

$$\frac{1}{T_{eff}} \exp\left(\frac{-Q}{R \cdot T_{eff}}\right) = \frac{1}{T_2 - T_1} \int_{T_1}^{T_2} \frac{1}{T} \exp\left(\frac{-Q}{R \cdot T}\right), \tag{5}$$

The isothermal effective temperature may be calculated by equation (5) in terms of Q, the activation energy, T_2 and T_1, the upper and lower temperatures for thermal cycling, and R, the gas constant. Notice that this relationship is independent of the heating rate, and it yields the same value whether heating or cooling; thus it may be used over only one half-cycle to yield an effective temperature valid for an entire cycle. Using Maple to solve (5) for T_{eff} with T_1=1223K (950°C) and T_2=1523K (1250°C), and Q=580,000 kJ·mol^{-1}(averaged from literature values in [11]), yields T=1451K = 1178°C. Multiple thermal segments may be combined but need to be weighted for time accordingly.

APPENDIX 3. TENSION EXPERIMENT SUMMARY

Expt. Num	Title	Percent	Stress	N Cyc	Sample code	GL fract	hole fract	surface X	Broken	measured GL disp	measured pin disp	strain	initial density	final density
-	-	%	MPa	-	-	-	-	-	-	µm	µm	%	g/ cm3	g/ cm3
4	C1A0_5	0	5	*25*	0-3-A			1	N	768	1283	6.2%	5.92	5.25
13	C1B0_5	0	5	*25*	0-3-B	X			X	432	317	3.3%	5.25	5.21
7	E1A0_5	0	5	*25*	0-8-A			2	N	724	1499	5.7%	5.94	5.31
17	C2A0_10	0	10	*25*	0-5-AT			1	N	819	1537	6.4%	5.93	5.08
22	C2B0_10	0	10	*25*	0-5-BT			1	N	38	133	0.3%	5.08	5.05
5	H1A0_5	0	5	*7*	0-4-A		X	0	X	413	2242	3.3%	5.92	5.30
20	H2A0_5	0	5	*6*	0-7-A		X	1	X	648	3200	5.1%	5.94	5.32
3	C1A5_5	5	5	*8*	5-9-A		X	0	X	629	1981	4.9%	5.82	5.33
9	C2A5_5	5	5	*25*	5-3-A			0	N	64	533	0.5%	5.50	5.62
10	C2B5_5	5	5	*25*	5-3-B			0	N	44	413	0.3%	5.62	5.59
25	C2C5_5	5	5	*8*	5-3-C		X	0	X	0	na	0.0%	5.59	5.61
14	E3A5_5	5	5	*25*	5-8-A			0	N	6	311	0.0%	5.37	5.74
15	E3B5_5	5	5	*25*	5-8-B			0	N	6	241	0.0%	5.74	5.74
26	CEA5_5	5	5	*7*	5-8-C		X	0	X	13	152	0.1%	5.74	5.76
19	C1A5_10	5	10	*11*	5-4-AT	X			X	178	279	1.4%	5.34	5.66
2	C0A10_5	10	5	*25*	10-4-B		X	0	X	438	438	3.4%	lost	5.23
8	C1A10_5	10	5	*25*	10-8-B			0	N	381	610	3.0%	5.96	5.75
12	C1B10_5	10	5	*12*	10-8-C		X	0	X	222	902	1.7%	5.75	5.75
16	E1A10_5	10	5	*25*	10-9-A			0	N	775	1886	6.1%	5.76	5.42

APPENDIX 4. COMPRESSION EXPERIMENT SUMMARY

Expt Num.	Title	Percent	Stress	N Cyc	Sample code	Date Run	flared	barrelled	cracked	length	LVDT displace	measured displace	*strain*	initial density	final density
-	-	%	MPa	-	-	-	-	-	-	µm	µm	µm	%	g/cm3	g/cm3
1	CCA0_10	0	10	*15*	0-C1-A	24-Feb-97	1	0	3	8582	-701	-438	*-5.1%*	5.91	N/A
17	EDA0_10	0	10	*25*	0-C7-A	5-Mar-97	1	0	3	8582	*-309*	-185	*-2.2%*	5.92	N/A
8	CCA0_20	0	20	*9*	0-C4-A	28-Feb-97	1	0	3	8584	-2043	-340	*-4.0%*	5.86	N/A
9	CDA0_20	0	20	*25*	0-C5-A	1-Mar-97	3	0	2	8582	-980	-1061	*-12.4%*	5.88	N/A
11	ECA0_20	0	20	*25*	0-C6-A	2-Mar-97	0	1	3	8584	-987	-365	*-4.3%*	5.97	N/A
4	CDA5_10	5	10	*25*	5-C8-A	26-Feb-97	0	0	0	8585	5	-227	*-2.6%*	5.66	5.72
3	ECA5_10	5	10	*25*	5-C2-A	26-Feb-97	0	1	2	8585	-610	-14	*-0.2%*	5.88	5.33
10	EDA5_10	5	10	*25*	5-C12-A	2-Mar-97	0	0	0	8588	-554	-235	*-2.7%*	5.61	5.76
5	CCA5_20	5	20	*25*	5-C11-A	27-Feb-97	0	0	0	8578	-534	-490	*-5.7%*	5.44	5.78
15	CDA5_20	5	20	*25*	5-C13-a	3-Mar-97	0	1	0	8677	*-639*	-542	*-6.2%*	5.91	5.58
12	ECA5_20	5	20	*25*	5-C5-A	3-Mar-97	0	1	1	8585	-525	-546	*-6.4%*	5.98	5.40
16	EDA5_20	5	20	*25*	5-C14-A	4-Mar-97	0	0	0	8680	-571	-493	*-5.7%*	5.79	5.53
21	CLA5_5	5	5	*49*	5-C20-B	26-Apr-97	1	0	3	8010	*-79*	-22	*-0.3%*	5.82	5.90
20	ELA5_5	5	5	*49*	5-C19-B	25-Apr-97	1	0	3	8322	*-73*	-98	*-1.2%*	6.01	5.87
13	CSA5_10	5	10	*25*	5-C3-B	3-Mar-97	0	0	0	8175	-125	-107	*-1.3%*	5.90	5.83
14	ESA5_10	5	10	*25*	5-C4-B	4-Mar-97	0	0	0	8194	*-119*	-64	*-0.8%*	5.86	5.84
18	CSA5_20	5	20	*25*	5-C6-B	23-Apr-97	1	0	3	8246	*-178*	-172	*-2.1%*	5.95	5.99
19	ESA5_20	5	20	*25*	5-C9-B	24-Apr-97	1	0	3	8307	*-217*	-141	*-1.7%*	5.93	5.97

APPENDIX 5. ENGINEERING DRAWING OF THE TENSILE SAMPLE.

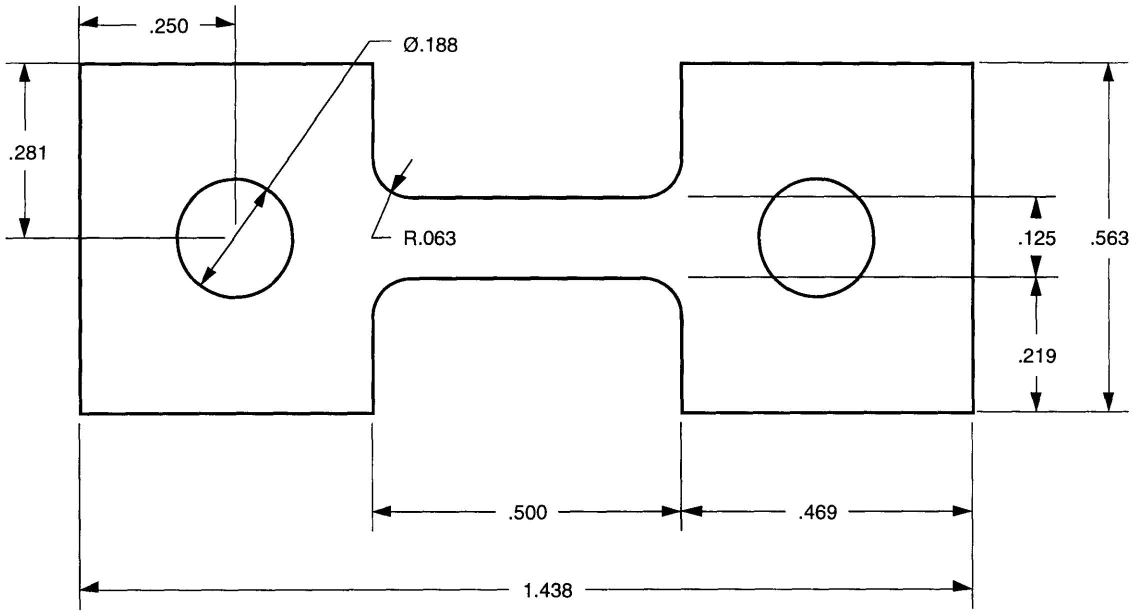

Note 1: Samples to be machined 0.113 inch thick, uniform to within +0.000", -0.004".

Note 2: 0.188 dia holes to receive 4.0 mm (0.157") pin or 5/32 inch (0.156") pin.

APPENDIX 6. ESHELBY TECHNIQUE CALCULATIONS

The internal stresses generated in the experimental material may be calculated theoretically by the Eshelby technique, as described in ref. [19]. In the following, numbers in parentheses refer to equations in that work.

To develop the equations for the mean matrix and particle stresses and strains, the absolute temperature (T), and the particle volume fraction for the 5% composite (f) must first be defined (as referenced in the main text):

$f := .05 \qquad T := 273 + 1200 \qquad T = 1473$

The following values for the matrix PSZ are defined: Poisson's ratio (num), the elastic modulus at 1200°C (Em), followed by the similar values for the zirconia "inclusion" or particle: Poisson's ratio (nu), the elastic modulus at 1200°C (E). These values, as tabluated in the main text, are the same for the matrix and inclusion.

$\mathrm{num} := 0.27 \qquad \mathrm{nu} := 0.27$

$\mathrm{Em} := 110 \cdot 10^{9} \qquad E := 110 \cdot 10^{9}$

Next an identity matrix for the matrix calculations is defined,

$I := \mathrm{identity}(6) \qquad \mathrm{ORIGIN} := 1$

as is the Eschelby S tensor given in Clyne and Withers (Appendix III):

$$S := \begin{bmatrix} \frac{7 - 5\cdot\mathrm{num}}{15\cdot(1-\mathrm{num})} & \frac{5\cdot\mathrm{num} - 1}{15\cdot(1-\mathrm{num})} & \frac{5\cdot\mathrm{num} - 1}{15\cdot(1-\mathrm{num})} & 0 & 0 & 0 \\ \frac{5\cdot\mathrm{num} - 1}{15\cdot(1-\mathrm{num})} & \frac{7 - 5\cdot\mathrm{num}}{15\cdot(1-\mathrm{num})} & \frac{5\cdot\mathrm{num} - 1}{15\cdot(1-\mathrm{num})} & 0 & 0 & 0 \\ \frac{5\cdot\mathrm{num} - 1}{15\cdot(1-\mathrm{num})} & \frac{5\cdot\mathrm{num} - 1}{15\cdot(1-\mathrm{num})} & \frac{7 - 5\cdot\mathrm{num}}{15\cdot(1-\mathrm{num})} & 0 & 0 & 0 \\ 0 & 0 & 0 & \frac{4 - 5\cdot\mathrm{num}}{15\cdot(1-\mathrm{num})} & 0 & 0 \\ 0 & 0 & 0 & 0 & \frac{4 - 5\cdot\mathrm{num}}{15\cdot(1-\mathrm{num})} & 0 \\ 0 & 0 & 0 & 0 & 0 & \frac{4 - 5\cdot\mathrm{num}}{15\cdot(1-\mathrm{num})} \end{bmatrix}$$

Next, we define the three prinicipal matrix compliance values (Cm11, Cm12, and Cm44) and the matrix material compliance tensor (Cm), followed by the corresponding values for the zirconia inclusion (Ci11, Ci12, Ci44, and Ci):

$$\mathrm{Cm11} := \frac{\mathrm{Em}\cdot\mathrm{num}}{(1+\mathrm{num})\cdot(1-2\cdot\mathrm{num})} + \frac{\mathrm{Em}}{(1+\mathrm{num})}$$

$$Cm12 := \frac{Em \cdot num}{(1 + num) \cdot (1 - 2 \cdot num)}$$

$$Cm44 := \frac{Cm11 - Cm12}{2}$$

$$Cm := \begin{bmatrix} Cm11 & Cm12 & Cm12 & 0 & 0 & 0 \\ Cm12 & Cm11 & Cm12 & 0 & 0 & 0 \\ Cm12 & Cm12 & Cm11 & 0 & 0 & 0 \\ 0 & 0 & 0 & Cm44 & 0 & 0 \\ 0 & 0 & 0 & 0 & Cm44 & 0 \\ 0 & 0 & 0 & 0 & 0 & Cm44 \end{bmatrix}$$

$$Ci11 := \frac{E \cdot nu}{(1 + nu) \cdot (1 - 2 \cdot nu)} + \frac{E}{(1 + nu)}$$

$$Ci12 := \frac{E \cdot nu}{(1 + nu) \cdot (1 - 2 \cdot nu)}$$

$$Ci44 := \frac{Ci11 - Ci12}{2}$$

$$Ci := \begin{bmatrix} Ci11 & Ci12 & Ci12 & 0 & 0 & 0 \\ Ci12 & Ci11 & Ci12 & 0 & 0 & 0 \\ Ci12 & Ci12 & Ci11 & 0 & 0 & 0 \\ 0 & 0 & 0 & Ci44 & 0 & 0 \\ 0 & 0 & 0 & 0 & Ci44 & 0 \\ 0 & 0 & 0 & 0 & 0 & Ci44 \end{bmatrix}$$

The coefficients of thermal expansion for the matrix (alpham) and the inclusion (alphai) are defined, followed by dt, the thermal cycle magnitude, for CTE-mismatch calculation:

$alpham := 12 \cdot 10^{-6}$ $\quad$ $alphai := 7 \cdot 10^{-6}$ $\quad$ $dT := 300$

Total thermal strain is defined as the CTE mismatch times the change in temperature plus the linear transformation strain, (1/3)(ΔV/V), where ΔV/V is 6%. Thermal strain is entered for three dimensions in εt:

$thermal := [(alpham - alphai) \cdot dT]$ $\quad$ $transf := \frac{0.06}{3}$

$$\varepsilon t := (thermal + transf) \cdot \begin{bmatrix} 1 \\ 1 \\ 1 \\ 0 \\ 0 \\ 0 \end{bmatrix}$$

Clyne and Withers give the Eschelby equivalent transformation strain in equation (3.2.1) calculated here as εT:

$$\varepsilon T := -\left[\left[(Cm - Ci)\cdot\left[S - f\cdot(S - I)\right]\right] - Cm\right]^{-1}\cdot Ci\cdot \varepsilon t$$

The authors give the mean matrix strain (εmmean) in equation (3.24) as

$$\varepsilon mmean := -f\cdot(S - I)\cdot \varepsilon T$$

from which the mean matrix stess (σmmean) may be calculated as

$$\sigma mmean := Cm\cdot \varepsilon mmean$$

The mean inclusion stress (σimean) is found by imposing the constrain that the total internal stress must sum to zero, and the mean particle strain (εimean) is calculated with the complaince tensor:

$$\sigma imean := \frac{f - 1}{f}\cdot \sigma mmean$$

$$\varepsilon imean := Ci^{-1}\cdot \sigma imean$$

And, finally, the mean values of matrix and inclusion stress and strain for the PSZ-5% zirconia composite may be calculated:

$$\sigma mmean\cdot 10^{-6} = \begin{bmatrix} 108 \\ 108 \\ 108 \\ 0 \\ 0 \\ 0 \end{bmatrix} \qquad \sigma imean\cdot 10^{-6} = \begin{bmatrix} -2051.8 \\ -2051.8 \\ -2051.8 \\ 0 \\ 0 \\ 0 \end{bmatrix}$$

$$\varepsilon mmean\cdot 10^{6} = \begin{bmatrix} 451.6 \\ 451.6 \\ 451.6 \\ 0 \\ 0 \\ 0 \end{bmatrix} \qquad \varepsilon imean\cdot 10^{6} = \begin{bmatrix} -8580.4 \\ -8580.4 \\ -8580.4 \\ 0 \\ 0 \\ 0 \end{bmatrix}$$

APPENDIX 7. CALCULATIONS FOR SATO AND KURIBAYASHI MODEL

The details for the model discussed in section 5.3 which was based on work by Sato and Kuribayashi [8] are shown below for a 5 MPa externally applied stress. When equations were used from this reference the number is listed in parentheses in the text.

First, the range of temperature cycling is defined by T0 and T1, with a half-cycle time of tmax. These are combined into an expression for temperature as a function of time,T(t).

$$T0 := 273 + 950 \qquad T1 := 273 + 1250 \qquad tmax := 660$$

$$T(t) := T0 + \frac{T1 - T0}{tmax} \cdot t$$

The transformation strain ("transf") is (1/3)(ΔV/V), where ΔV/V = 6%. This is added to the thermal coefficient of expansion mismatch Δa (see Appendix 6) to yield the total transformation mismatch ("mismatch") of 2.15%.

$$transf := \frac{0.06}{3} \qquad mismatch := transf + 5 \cdot 10^{-6} \cdot (T1 - T0)$$

Since a model will be created for a PSZ-5% zirconia, the volume fraction, f, must be defined:

$$f := 0.05$$

Here we will be using the intrinsic creep properties of the compsoite in the final model. Thus the stress exponent, n is defined, as is the part of the creep equation (equation 15 in the main text) which does not include the stress, denoted by "B". The gas constant is also defined, and the stress in this example is defined as 5 MPa:

$$n := 1.32 \qquad R := 8.314$$

$$B(t) := \frac{1.32 \cdot 10^{8}}{T(t)} \cdot \exp\left[-\frac{580000}{R \cdot T(t)}\right]$$

$$stress := 5 \cdot 10^{6}$$

These data yield an expected strain rate of

$$t := 456$$

$$B(503.6) \cdot (stress)^{n} = 8.593 \cdot 10^{-8}$$

at t=456 s, which corresponds to 1178°C. The result confirms the experimental value given in the main text. Next the temperature-dependent constant must be averaged over the thermal half-cycle (with an exponent of 1/n, see the reference) for use in the model:

$$Bav := \int_{0}^{tmax} B(t)^{\frac{1}{n}} \, dt$$

And finally equation (30) in the reference given above may be written as a function of the volume fraction *f*, the average time-dependent creep constant, Bav, the stress exponent n, and the mismatch stress divided over a half cycle to yield the expected strain per half cycle (delta):

$$\text{delta} := \frac{2\cdot n\cdot (n+4)}{5\cdot 2^{\frac{1}{n}}}\cdot\frac{\left[1-f^{\frac{1}{n}}\right]\cdot f}{(1-f)^2\cdot f^{\frac{1}{n}}}\cdot \text{stress}\cdot\left[\frac{\text{mismatch}}{\text{tmax}}\right]^{1-\frac{1}{n}}\cdot \text{Bav}$$

The strain rate may be calculated by dividing delta by the half-cycle time, tmax, for the following result. This process was repeated successively for the different stress levels presented in the text.

$$\frac{\text{delta}}{\text{tmax}} = 2.158\cdot 10^{-7}$$

BIBLIOGRAPHY

1. Green, D.J., R.H.J. Hannink, and M.V. Swain, *Transformation Toughening of Ceramics*. 1989, Boca Raton, FL: CRC.

2. Stevens, R., *Engineering Properties of Zirconia*, in *Engineered Materials Handbook - Ceramics and Glasses*. 1986, ASM International. p. 775-786.

3. Pilling, J. and N. Ridley, *Superplasticity in Crystalline Solids*. 1989, London: The Institute of Metals.

4. Poirier, J.P., *Creep of Crystals*. 1985: Cambridge University Press.

5. Dunand, D.C. *Transformation Superplasticity in Metals, Alloys and Composites*. in *International Symposium on Superplasticity in Materials*. 1997: TMS. **in print.**

6. Sauveur, A., *What is Steel - Another Answer.* Iron Age, 1924. **113**: p. 581-583.

7. Wu, M.Y., J. Wadsworth, and O.D. Sherby, *Internal Stress Superplasticity in Anisotropic Polycrystalline Zinc and Uranium.* Metallurgical Transactions, 1987. **18A**: p. 451-462.

8. Sato, E. and K. Kuribayashi, *A Model of Internal Stress Superplasticity Based on Continuum Mechanics.* Acta Metallurgica et Materialia, 1993. **41**: p. 1759-1767.

9. Dunand, D.C. and C.M. Bedell, *Transformation-Mismatch Superplasticity in Reinforced and Unreinforced Titanium.* Acta Materialia, 1996. **44**(3): p. 1063-1076.

10. Bengough, G.D., *A Study of the Properties of Alloys at High Temperatures.* J. Inst. Metals, 1912. **7**: p. 123-174.

11. Chokshi, A.H., *Superplasticity in Fine Grained Ceramics and Ceramic Composites: Current Understanding and Future Prospects.* Materials Science and Engineering, 1993. **166**: p. 119-133.

12. Maehara, Y. and T.G. Langdon, *Superplasticity in Ceramics.* Journal of Materials Science, 1990. **25**: p. 2275-2286.

13. Greenwood, G.W. and R.H. Johnson, *The Deformation of Metals Under Stress during Phase Transformations.* Proceedings of the Royal Society of London, 1965. **283A**: p. 403-422.

14. Johnson, C.A., R.C. Bradt, and J.H. Hoke, *Transformational Plasticity in Bi2O3.* Journal of the American Ceramic Society, 1975. **58**: p. 37-40.

15. Hart, J.L. and A.C.D. Chaklader, *Superplasticity in pure ZrO2.* Mater. Res. Bull., 1967. **2**: p. 521-526.

16. Lobb, R.C., E.C. Sykes, and R.H. Johnson, *The Superplastic Behaviour of Anisotropic Metals Thermally Cycled under Stress.* Metal Sci. J., 1972. **6**: p. 33-39.

17. Pickard, S.M. and B. Derby, *The Influence of Microstructure on Internal Stress Superplasticity in Polycrystalline Zinc.* Scripta Metallurgica et Materialia, 1991. **25**: p. 467-472.

18. Roberts, A.C. and A.H. Cottrell, *Creep of Alpha Uranium During Irradiation with Neutrons.* Philosophical Magazine, 1956. **1**: p. 711-717.

19. Clyne, T.W. and P.J. Withers, *An Introduction to Metal Matrix Composites.* 1993: Cambridge University Press, Cambridge.

20. Huang, C.Y. and G.S. Daehn. *Superplastic Forming of Metal Matrix Composites by Thermal and Pressure Cycling.* in *Superplasticity and Superplastic Forming 1995.* 1996: TMS, Warrendale PA.

21. Zwigl, P. and D.C. Dunand. *Transformation Mismatch Plasticity in NiAl/ZrO2 Intermetallic Matrix Composites.* in *International Symposium on Superplasticity in Materials.* 1997: TMS. **in print.**

22. Poirier, J.P., *On Transformation Plasticity.* Journal of Geophysical Research, 1982. **87**(88): p. 6791-6797.

23. Leblond, J.B., J. Devaux, and J.C. Devaux, *Mathematical Modelling of Transformation Plasticity in Steels. I: Case of Ideal Plastic Phases.* International Journal of Plasticity, 1989. **5**: p. 551-572.

24. Diani, J.M., H. Sabar, and M. Berveiller, *Micromechanical Modelling of the Transformation Induced Plasticity (TRIP) Phenomenon in Steels.* International Journal of Engineering Science, 1995. **33**(13): p. 1921-1934.

25. de Jong, M. and G.W. Rathenau, *Mechanical Properties of an Iron-Carbon Alloy during Allotropic Transformation.* Acta Metallurgica, 1961. **9**: p. 714-720.

26. Zhang, H., G.S. Daehn, and R.H. Wagoner, *The Temperature Cycling Deformation of Particle Reinforced Metal Matrix Composites - A Finite Element Study.* Scripta Metallurgica et Materialia, 1990. **24**: p. 2151-2155.

27. Kot, R.A. and V. Weiss, *Transformation Plasticity in Iron-Nickel Alloys.* Metallurgical Transactions, 1970. **1**: p. 2685-2693.

28. Paterson, M.S., *Creep in Transforming Polycrystalline Materials.* Mechanics of Materials, 1983. **2**: p. 103-109.

29. Wolten, G.M., *Diffusionless Phase Transformations in Zirconia and Hafnia.* J. Am. Ceram. Soc., 1963. **46**(9): p. 418-422.

30. Rühle, M. and A.H. Heuer, *Phase Transformations in Zirconia-Containing Ceramics: II, the Martensitic Reaction in Zirconia*, in *Phase Transformations in Zirconia Containing Ceramics*, e.a. N. Claussen, Editor. 1984.

31. Chen, I.W. and Y.H. Chiao, *Martensitic Nucleation in ZrO2 and HfO2.* Acta Metallurgica, 1983. **31**: p. 1627-1638.

32. Maiti, H.S., K.V.G.K. Gorhale, and E.C. Subbarao, *Kinetics and Burst Phenomenon in ZrO2 Transformation.* Journal of the American Ceramic Society, 1972. **55**: p. 317-322.

33. Claussen, N., F. Sigulinski, and M. Rühle, *Phase Transformation of Solid Solutions of Zirconia ind Hafnia in an Alumina Matrix*, in *L.W. Hobbs*, A.H. Heuer, Editor. 1981, American Ceramic Society: Columbus, OH. p. 164-167.

34. Kingery, W.D., *Pressure Forming of Ceramics*, in *Ceramic Fabrication Processes*, W.D. Kingery, Editor. 1958, MIT Technology Press. p. 55-61.

35. Wakai, F., *Effects of Solute Ion and Grain Size on Superplasticity of ZrO2 Polycrystals.* Journal of Materials Science, 1991. **26**: p. 241-247.

36. Bravo-Leon, A., *et al.*, *The Role of a Threshold Stress in the Superplastic Deformation of Fine-Grained Yttri-Stabilized Zirconia Polycystals.* Acta Metallurgica, 1996. **34**(7): p. 1155-1160.

37. Bravo-Leon, A., M. Jiménez-Menlendo, and A. Dominguez-Rodríguez, *High Temperature Plastic Deformation at Very Low Stresses of Fine-Grained Y2O3-Partially Stabilized ZrO2.* Scripta Metallurgica, 1996. **35**(4): p. 551-555.

38. Lee, D., *MS Thesis.* M.S. Thesis, Department of Materials Science and Engineering, MIT, 1995.

39. Murray, P., D.T. Livey, and J. Williams, *The Hot Pressing of Ceramics*, in *Ceramic Fabrication Processes*, W.D. Kingery, Editor. 1958, MIT Technology Press. p. 147-171.

40. McNaughton, J.L. and C.T. Mortimer, *Differential Scanning Calorimetry*, in *IRS; Physical Chemistry Series 2*. 1975.

41. Kajihara, K., Y. Yoshizawa, and T. Sakuma, *The Enhancement of Superplastic Flow in Tetragonal Zirconia Polycrystals with SiO2-Doping.* Acta. Metall. et Mater., 1995. **43**(3): p. 1235-1242.